SEDIMENTOLOGY the journal of the International Association of Sedimentologists IAS

Sedimentology (2024) **71**, 1639–1685 doi: 10.1111/sed.13190

Evolving fill-and-spill patterns across linked early post-rift depocentres control lobe characteristics: Los Molles Formation, Argentina

AURÉLIA M-L. J. PRIVAT* , JEFF PEAKALL* , DAVID M. HODGSON*, ERNESTO SCHWARZ† , CHRISTOPHER A-L. JACKSON‡ and JONATAN A. ARNOL§

**Stratigraphy Group, School of Earth and Environment, University of Leeds, Leeds LS29JT, UK (E-mail: aurelia.privat@gmail.com)*

†Centre of Geological Investigation (CIG)-CONICET, National University of La Plata (UNLP), Diagonal 113 N°275 B1904, La Plata, Argentina

‡Basins Research Group (BRG), Department of Earth Science and Engineering, Imperial College, Prince Consort Road, London SW7 2BP, UK

§División Geología, Museo de La Plata, Facultad de Ciencias Naturales y Museo, National University of La Plata (UNLP), Paseo del bosque s/n B1900FWA, La Plata, Argentina

Associate Editor – Adam McArthur

ABSTRACT

Inherited rift topography controls the sediment routing, timing of sand supply, and sedimentary linkage of early post-rift depocentres. Exhumed examples of early post-rift turbidite systems are rare and previous studies have examined the evolution of individual depocentres; in contrast, the detailed evolution of early post-rift turbidite systems across multiple depocentres has never been documented. Current fill-and-spill models do not detail the stratigraphic architecture and evolution of sedimentological characteristics of multiple intraslope fans developed across topography, including bed type distributions. Here, the evolution of three intraslope fans that developed across two early post-rift depocentres is documented along an 18 km long transect in the southern Neuquén Basin, Argentina. The relative chronology of sand supply in depocentres is constrained with new U–Pb ages, and sediment source areas with provenance analysis. The early post-rift intraslope fans record progradation of the system and progressive sedimentary linkage of post-rift depocentres, transverse to local syn-rift structures, with sediment routing subparallel to the cratonic basin margin. The large-scale stratigraphic architecture of intraslope fans indicates an evolution as a fill-and-spill system, with initial confinement through flow stripping and overspill to spillover with erosion and bypass across a transverse topographic high separating the depocentres. Changes in early post-rift intraslope fan characteristics, including thickness, sandstone content, lobe complex stacking patterns, stratal termination patterns and bed type distribution, record changing confinement through time within a depocentre, and spatially across depocentres. The strong spatial and vertical stratigraphic variability of transitional flow deposits and hybrid event beds reflects enhanced erosion, sediment bypass and flow transformation across transverse relief between the two depocentres during the spillover phase. These findings advance current understanding of early post-rift turbidite systems and refine fill-and-spill models, which will help the prediction of spatial and vertical changes in rock quality and connectivity in subsurface hydrocarbon reservoirs and CO_2 storage sites.

Keywords Back-arc, early post-rift, fill-and-spill, hybrid event beds, intraslope lobe, rift basin.

INTRODUCTION

Understanding the spatial and temporal evolution of early post-rift deep-marine sandy systems and the roles of sediment supply, inherited rift topography, differential subsidence and local compaction, are key to determining the architecture of hydrocarbon reservoirs and CO_2 storage sites. Inherited rift topography can have a long-lived influence on the geometry and connectivity of early to late post-rift deep-marine sandy systems. However, the nature of stratigraphic architecture, and turbiditic facies, remain poorly documented. Ponded, perched or fill-and-spill confined systems develop across seabed topography (i.e. salt or mud diapirs, fault-scarps) and are well-documented in a range of tectonic settings, in the subsurface (e.g. Booth *et al.*, 2003; Smith, 2004; Rodriguez *et al.*, 2021; Casagrande *et al.*, 2022) and at outcrop (e.g. Sinclair & Tomasso, 2002; Shultz & Hubbard, 2005; Vinnels *et al.*, 2010; Southern *et al.*, 2015; Tinterri & Tagliaferri, 2015; Brooks *et al.*, 2018; Cumberpatch *et al.*, 2021). Numerous subsurface studies have highlighted large-scale interactions between inherited or compaction-enhanced rift-related topography in deep-marine, *late post-rift* systems (Lien, 2005; Fugelli & Olsen, 2007; Jackson *et al.*, 2008; Ravnås *et al.*, 2014; Dmitrieva *et al.*, 2018). In comparison, this topic has been emphasized only in a few studies of deep-marine, *early post-rift* systems (Argent *et al.*, 2000; Burgess *et al.*, 2000; Færseth & Lien, 2002; Zachariah *et al.*, 2009; Veiga *et al.*, 2013). Furthermore, subsurface studies lack detailed documentation of sedimentary characteristics, and the rare examples of exhumed early post-rift sandy systems have predominantly been investigated as part of large-scale studies focused on the overall stratigraphic expression of the syn-rift to post-rift transition (Takano, 2002; Alves *et al.*, 2003; Lien, 2005; Yu *et al.*, 2013; D'Elia *et al.*, 2015; Hadlari *et al.*, 2016).

Deep-marine early post-rift sandy systems typically evolve across multiple depocentres, progressively smoothing the inherited rift topography, from the slope to basin-floor. However, the evolution from disconnected to linked individual depocentres and the related sedimentation processes have not been examined in detail. Early post-rift systems are likely fed by several intrabasinal and extrabasinal sediment source areas (e.g. Alves *et al.*, 2003; Lien, 2005; Fugelli & Olsen, 2007). This can result in important sedimentary facies variability and reservoir heterogeneity, like those defining syn-rift systems (e.g. Haughton *et al.*, 2003; Southern *et al.*, 2017; Stevenson *et al.*, 2020; Steventon *et al.*, 2021). These factors suggest a complicated organization of early post-rift sandy systems, from large-scale stratigraphic architecture to facies-scale variability, not captured by models depicting the evolution of rift basins (e.g. Prosser, 1993; Ravnås & Steel, 1998; Gawthorpe & Leeder, 2000).

Here, the Early Jurassic Los Molles Formation (Weaver, 1931) in the Eastern Catán-Lil and Chachil basins of the southern Neuquén Basin (Argentina) is investigated. This forms a rare, exhumed example of an early post-rift, sandy deep-marine system developed in partially linked intraslope depocentres (see Privat *et al.*, 2021, for characterization of the late syn-rift to early post-rift evolution). Exposures of early post-rift strata enable construction of a *ca* 18 km long correlation panel across two depocentres, showing the large-scale stratigraphic architecture of three intraslope fans. New U–Pb SHRIMP ages are presented, refining the current chronostratigraphic framework, alongside petrographic analyses, enabling investigation of the potential sediment source(s) for these early post-rift sandstones. The objectives of this paper are to: (i) constrain the timing and provenance of sand supply and the regional depositional context for the early post-rift system; (ii) detail the vertical and lateral/spatial stratigraphic variability of early post-rift intraslope fans across depocentres (i.e. sedimentological characteristics, thickness, stacking and stratal termination patterns, sandstone content, bed-types); and (iii) evaluate the role of inherited rift topography on spatial compartmentalization of sand across topographically complex slopes.

GEOLOGICAL AND STRATIGRAPHIC SETTING

The Neuquén Basin (36° S to 40° S) developed along the south-western convergent margin of the Gondwana–South American plate. Basin subsidence and sedimentation evolved through

three main tectonic stages; (i) Late Palaeozoic to Early Jurassic post-orogenic thermo-mechanical collapse, and intracontinental volcanic rifting; (ii) Early Jurassic to Early Cretaceous extensional back-arc basin development with rollback subduction and post-rift thermal subsidence; and (iii) Late Cretaceous to Cenozoic retroarc foreland basin development with subduction-driven compression and formation of the Andean fold-and-thrust belt (Vergani *et al.*, 1995; Legarreta & Uliana, 1996; Franzese & Spalletti, 2001; Howell *et al.*, 2005; Horton *et al.*, 2016).

In the southern Neuquén Basin (Fig. 1), oblique rifting resulted in the opening of numerous grabens and half-grabens with variable rift fault orientations (Vergani *et al.*, 1995; Pángaro *et al.*, 2006; Silvestro & Zubiri, 2008; Figs 1 and 2). Syn-rift volcanism (Late Triassic to Early Jurassic) controlled the infill of the sub-basins with continental and lacustrine volcano-sedimentary successions forming the Precuyano Cycle (Norian–Sinemurian; Vergani *et al.*, 1995; Legarreta & Uliana, 1996; Franzese & Spalletti, 2001; Schiuma & Llambías, 2008; Figs 2 and 3). The transition from intraplate rifting to rollback subduction (Mpodozis & Ramos, 2008) is recorded by activity of the Early Andean magmatic arc dated from the Late Triassic (Bermudez *et al.*, 2002; Llambías *et al.*, 2007) to the Sinemurian–Pliensbachian (Schiuma & Llambías, 2008; Spalletti *et al.*, 2010).

The syn-rift to post-rift transition coincided with the proto-Pacific Ocean incursion and propagated diachronously from the northern (Rhaetian) to southern (Early to Late Pliensbachian) Neuquén Basin (Franzese *et al.*, 2006; Lanés *et al.*, 2008; Pángaro *et al.*, 2009; D'Elia *et al.*, 2015; Privat *et al.*, 2021). In the southern Neuquén Basin, the Early Jurassic (Pliensbachian–Aalenian) marine transgression of rift topography (Riccardi, 1991; Damborenea *et al.*, 2013; Leanza *et al.*, 2013) resulted in the formation of several marine depocentres (Legarreta & Uliana, 1996; Gómez Omil *et al.*, 2002; Pángaro *et al.*, 2009). Their evolution is recorded by the Early Jurassic Cuyo Group, which unconformably overlies the Precuyano Cycle (Gulisano *et al.*, 1984), forming a transgressive succession defined by late syn-rift shallow-marine systems (Chachil and Chacaico formations) and an early post-rift deep-marine siliciclastic system (Los Molles Formation; Weaver, 1931; Gulisano & Guttiérrez Pleimling, 1995; De la Cruz & Suárez, 1997; Paim *et al.*, 2008; Leanza *et al.*, 2013; D'Elia *et al.*, 2015; Privat *et al.*, 2021; Figs 2 and 3). The Middle Jurassic Cuyo Group is bounded by a basal Toarcian–Aalenian and top intra-Callovian sequence boundary, forming a regressive succession including deltaic (Lajas Formation), fluvial (Challaco Formation) and evaporitic (Tábanos Formation) deposits (Gulisano & Guttiérrez Pleimling, 1995; Legarreta & Uliana, 1996; Paim *et al.*, 2008) (Fig. 3). The Middle Jurassic Cuyo Group records the formation of a single post-rift depocentre from the Middle Jurassic to Early Cretaceous, controlled by thermal subsidence and episodic transpression (e.g. Mpodozis & Ramos, 2008; Silvestro & Zubiri, 2008; Pángaro *et al.*, 2009) (Fig. 1).

The two studied rift depocentres correspond to the Eastern Catán-Lil and Chachil basins (Figs 2 and 3). The Eastern Catán-Lil Basin (Fig. 2) forms a small half-graben (10 km long, 5 km wide) bounded by the Cerro Mallín de Ibáñez and Tutavel crystalline basement highs (Chachil Plutonic Complex) and by the Puesto Rincón del Polo metamorphic basement horst (Piedra Santa Formation). The Chachil Basin forms a larger graben (>15 km long, 10 km wide; Franzese *et al.*, 2006; Privat *et al.*, 2021) and is separated from the Eastern Catán-Lil Basin by the Southern Chachil crystalline basement horst border (Fig. 2). Uplift and exhumation of rift depocentres occurred in response to Andean-driven compression along the westernmost extremity of the Huincul High, an ENE–WSW trending, inversion-related, intraplate structure bounding the southern Neuquén Basin margin (Gómez Omil *et al.*, 2002; Silvestro & Zubiri, 2008; García Morabito, 2010) (Fig. 1). Because the east–west Andean compressional stress field was oblique to the trend of the main rift faults, it only resulted in a partial inversion of rift faults along pre-rift basement structures, enabling the analysis of stratal relationships between rift structures and syn-rift to post-rift units (e.g. Franzese *et al.*, 2006; Muravchik *et al.*, 2014; Privat *et al.*, 2021). In the study area, the Los Molles Formation lacks evidence for extensional faulting and abrupt facies or thickness variations across syn-rift faults, which are mainly recorded in the Chachil and Chacaico formations, supporting its early post-rift nature (see Franzese *et al.*, 2006; Privat *et al.*, 2021).

The studied depocentres form a series of grabens and half-grabens associated with an ENE–WSW trending palaeoshelf–slope system along the southern Neuquén Basin margin involving the development of the Los Molles Formation turbidite deposits across the slope (cf. Gómez Omil *et al.*, 2002; Pángaro *et al.*, 2009; Brinkworth *et al.*, 2018). The Los Molles Formation includes

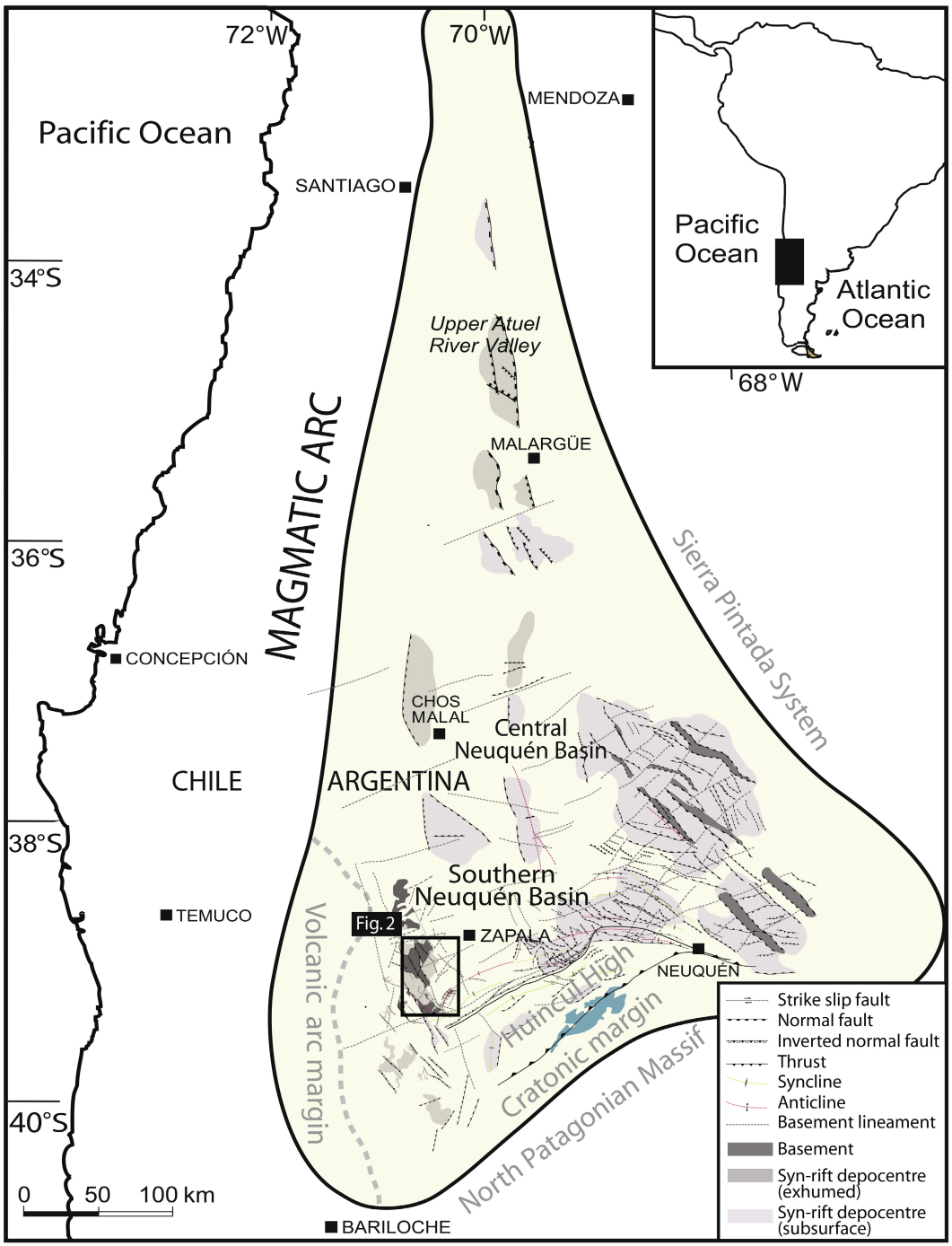

Fig. 1. General map of the Neuquén Basin showing the main tectonic structures including rift faults (black), basement lineaments and pre-rift suture zones (in grey) (compilation from subsurface studies after Gómez Omil *et al.*, 2002; Silvestro & Zubiri, 2008; Yagupsky, 2009; Cristallini *et al.*, 2009; Pángaro *et al.*, 2009; García Morabito, 2010; Bechis *et al.*, 2014). Note the location of the Huincul High and the cratonic and volcanic arc basin margins during the Early Jurassic. The position of the map of the study area (Fig. 2) is indicated.

Late Pliensbachian to Early Toarcian basinal organic-rich mudstone at its base and Toarcian to Aalenian lower slope to basin-floor sandy fans (Gulisano & Guttiérrez Pleimling, 1995; Burgess *et al.*, 2000; Gómez Omil *et al.*, 2002; Paim *et al.*, 2008; Brinkworth *et al.*, 2018). In this study, Unit 3 and Unit 4 (Figs 2 and 3), respectively, represent the lowermost muddy and the upper sandy

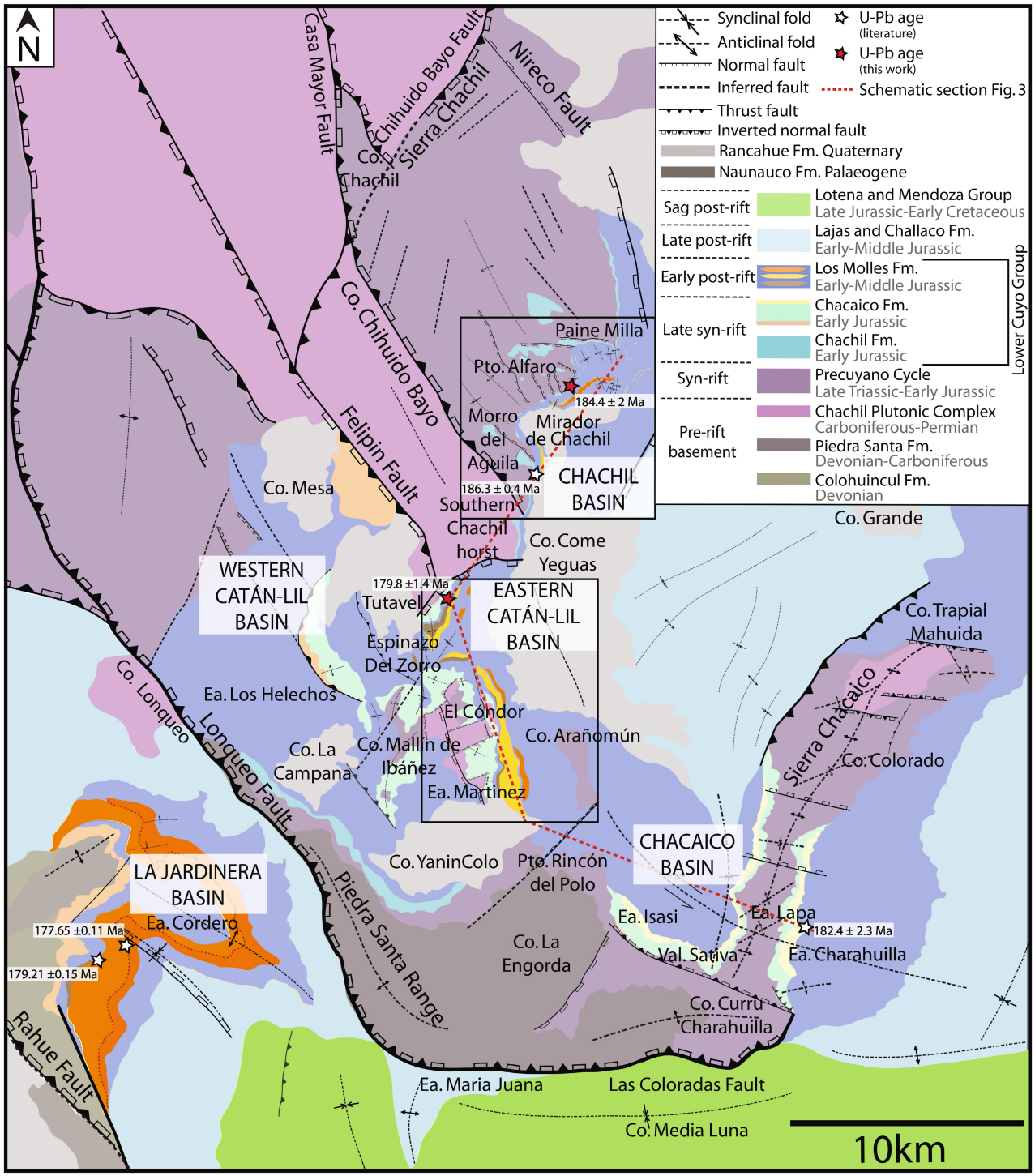

Fig. 2. Regional geological map of the study area showing the location and pre-rift, syn-rift and post-rift units in the study area, the different sandy depocentres (Chacaico, Eastern Catán-Lil, Chachil and La Jardinera) and the investigated sandy units (SU4.1 in brown, SU4.2 in yellow and SU4.3 in orange). The map includes information after Leanza & Blasco (1990), Gulisano & Guttiérrez Pleimling (1995), Cucchi *et al.* (2005), Franzese *et al.* (2006), Paim *et al.* (2008), García Morabito (2010) and Muravchik *et al.* (2014). See the stratigraphic position of U–Pb age data (Armella *et al.*, 2016; Naipauer *et al.*, 2018, and this study) in the studied depocentres on Figs 3 and 4. The limits of Fan 1 and 2 and corresponding U–Pb ages (Steel *et al.*, 2023) are highlighted by a dashed orange line and the overlying Los Molles Formation corresponds to slope deposits (Paim *et al.*, 2008).

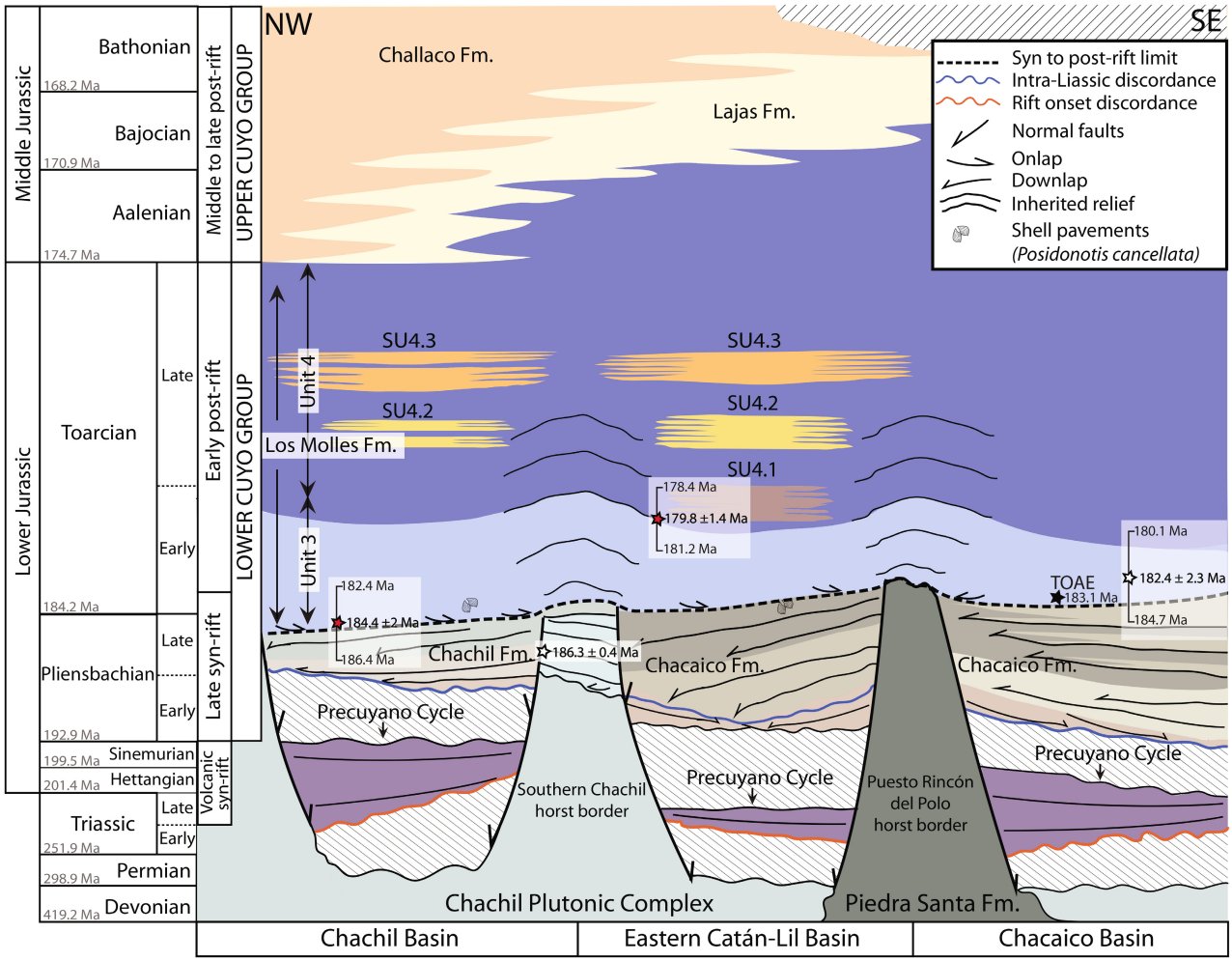

Fig. 3. Stratigraphy of the Cuyo Group, detailing the different formations of the Lower Cuyo Group in the three basins of the study area and the Los Molles Formation represented by Unit 3 and Unit 4, including sandy subunits (SU4.1, SU4.2 and SU4.3). Note the distribution of sandy subunits which record onset of sand supply since the late Early Toarcian according to new U–Pb (SHRIMP–SII) volcanic zircon age constraints from the present study shown by red stars in the Chachil Basin (184.4 ± 2 Ma) and in the Eastern Catán-Lil Basin (179.8 ± 1.4 Ma) (cf. location on Fig. 2). Ages from other outcrop studies in these basins are shown by white stars in the Chachil Basin (186.3 ± 0.4 Ma with U–Pb ID-TIMS, Armella *et al.*, 2016, modified from Leanza *et al.*, 2013) and the Chacaico Basin (182.4 ± 2.3 Ma with U–Pb SHRIMP, Naipauer *et al.*, 2018) (cf. location on Fig. 2). The distribution and age of basement, volcanic syn-rift and late-syn-rift deposits synthesize results of previous work in this area and from the literature (Gulisano & Gutiérrez Pleimling, 1995; Franzese *et al.*, 2006; Paim *et al.*, 2008). Note also the Toarcian Oceanic Anoxic Event (TOAE) after Al-Suwaidi *et al.* (2016) and biostratigraphic markers (ammonites, nannofossils and bivalve biozones, after Riccardi *et al.*, 2011; Damborenea *et al.*, 2013). Numerical Jurassic ages from Cohen *et al.* (2013).

part of the Los Molles Formation defined in the Chachil Basin by Privat (2019) and Privat *et al.* (2021). Unit 4 is further sub-divided into three different sandy subunits (SU4.1, SU4.2 and SU4.3), each representing a single depositional system (i.e. an intraslope submarine fan) investigated in this paper.

Previous outcrop studies that focus on the sandy fans of the Los Molles Formation in the La Jardinera depocentre (Fig. 2) interpreted an unconfined to weakly confined basin-floor or base-of-slope system, with little to no emphasis placed on the influence of inherited rift topography on lobe confinement (Paim *et al.*, 2008; Giacomone *et al.*, 2020; Arienti Gonçalves *et al.*, 2022; Steel *et al.*, 2023). However, the interaction of sandy fans of the Los Molles Formation with long-lived inherited rift topography along

the slope is suggested from subsurface data (Gómez Omil *et al.*, 2002; Pángaro *et al.*, 2009; Brinkworth *et al.*, 2018; Gutiérrez Pleimling *et al.*, 2021) and is documented at outcrop in other depocentres (Burgess *et al.*, 2000; Veiga *et al.*, 2013; Privat *et al.*, 2021; Martinez-Doñate *et al.*, 2023).

METHODOLOGY

Detailed stratigraphic and structural mapping was conducted using Global Positioning System referencing and Uncrewed Aerial Vehicle photogrammetry, drawing on and integrating data from previous geological studies (Fig. 2) (Leanza & Blasco, 1990; Gulisano & Guttiérrez Pleimling, 1995; Cucchi *et al.*, 2005; Franzese *et al.*, 2006; García Morabito, 2010; Muravchik *et al.*, 2014). The stratigraphic framework (Fig. 3) integrates depocentre fills with published geochronological data (Armella *et al.*, 2016; Naipauer *et al.*, 2018) and biostratigraphic markers (ammonites, nannofossils, bivalve biozones) (Riccardi *et al.*, 2011; Damborenea *et al.*, 2013; Al-Suwaidi *et al.*, 2016) and two new U–Pb SHRIMP Concordia ages (cf. analytical method in Supplementary Data S1) obtained from two tuff samples (Figs S1 and S2; Table S1) collected at the base and top of Unit 3 (Figs 2 and 3).

A detailed *ca* 18 km long correlation panel constructed from 25 logged sections (10 to 270 m long, 1 : 25 scale) documents the large-scale stratigraphic architecture and detailed sedimentological characteristics of three sandy subunits (SU4.1, SU4.2 and SU4.3) defined in Unit 4 in the Eastern Catán-Lil and Chachil basins (Figs 4 and S3 for detailed correlation panels). Palaeocurrent measurements were collected in each subunit from sole marks (grooves and flute casts), dune-scale and ripple-scale cross-stratification, and were plotted in rose diagrams with stereonet software (R.W. Allmendinger©) (Fig. 5). The transect in the Eastern Catán-Lil Basin is exposed along a north–south trending outcrop belt oblique to the main north-east palaeocurrent direction, whereas the north-east/south-west trending outcrop belt in the Chachil Basin is subparallel to the main north-east palaeocurrent direction (Fig. 5). Laterally extensive sandstone packages (i.e. lobe complexes, *sensu* Prélat *et al.*, 2009) in the sandy subunits were tracked in the field and constrained with photographic panels and virtual outcrop models. Marker beds such as debrites or thick mudstone units, and changes in sedimentological characteristics, aided correlation across depocentres (Fig. 4).

The textural and compositional characterization of sandstones is based on the analysis of 13 petrographic thin sections collected in all three subunits of Unit 4 (SU4.1, SU4.2 and SU4.3) (Fig. 4) (see *Quantitative petrography method* in Supplementary Data S1). Ternary diagrams (Fig. 6) are used to interpret provenance, based on recalculated parameters (Tables S2 and S3), compositional modes (Table S4) and point-count tables (Tables S5 and S6).

RESULTS

Geochronology and provenance

This study investigates the timing and provenance of Early Jurassic sand supply (Los Molles Formation) to two early post-rift depocentres bounded to the WSW by the Early Andean island arc system, and to the south-east by the cratonic basin margin (North Patagonian Massif), which could act as sediment sources (Fig. 1).

Geochronology

Description. Two tuff samples were collected in the Eastern Catán-Lil and Chachil basins (Fig. 2) to extract euhedral zircon crystals. Zircons were analysed and mounted to obtain two new U–Pb Concordia ages (Fig. S1; Table S1) using sensitive high-resolution ion microprobe (SHRIMP-SII) (see *Analytical method* in Supplementary Data S1). Tuff 1 comes from the top of Unit 3 in the Eastern Catán-Lil Basin (39°15.427′ S 70°34.959′ W) and Tuff 3 comes from the base of Unit 3 in the Chachil Basin (39°10.554′ S 70°31.447′ W) (Fig. S2). Deposition of Tuff 3 at the base of Unit 3 at 184.4 ± 2 Ma (2σ) in the Chachil Basin implies a latest Pliensbachian age for the basal part of the Los Molles Formation. This age is supported in the Eastern Catán-Lil Basin by the presence of *Posidonotis cancellata* (Leanza) (cf. assemblage zone in Riccardi *et al.*, 2011), which indicates that the basal part of the Los Molles Formation sits near the Pliensbachian–Toarcian boundary (Fig. 3). In the Eastern Catán-Lil Basin, Tuff 1 at the top of Unit 3 records an age of 179.8 ± 1.4 Ma (2σ) (Fig. S1), which implies a late Early Toarcian age for the Unit 3–Unit 4 boundary in the Los Molles Formation (Fig. 3).

Interpretation. The new U–Pb ages indicate that deposition of basinal mudstone (Unit 3) lasted from the latest Pliensbachian to the early-to-mid Early Toarcian, and that the early post-rift sand supply (Unit 4) reached the study area in the late Early Toarcian (Fig. 3). These ages imply that early post-rift sand supply in the study area preceded, and thus was not triggered by, Middle–Late Jurassic inversion. The inversion has been inferred previously as a driver for sand supply from cratonic sources caused by transpressional fault reactivation along the Huincul High (e.g. Naipauer *et al.*, 2012; Pujols *et al.*, 2018). This could be the case in slightly younger sandy depocentres such as La Jardinera (latest Toarcian, Paim *et al.*, 2008; Kochhann *et al.*, 2011; Steel *et al.*, 2023) (Fig. 2), where increased sand supply is associated with a major eustatic sea-level fall along the southern Neuquén Basin margin at the Toarcian–Aalenian boundary (Paim *et al.*, 2008). Therefore, the triggers for sand supply need to be reconciled with the timing and provenance of sand in the study area as discussed below.

Textural and compositional characteristics

Description. Detrital modes and provenance fields were identified using standard Qp-Lv-Lsm and Lv-Lm-Ls plots (Dickinson & Suczek, 1979; Ingersoll & Suczek, 1979), and volcanic sources were determined with Lvv-Lvmi-Lvl and Lvf-Lvmi-Lvl plots (Marsaglia & Ingersoll, 1992; Critelli & Ingersoll, 1995; Critelli *et al.*, 2023) (Figs 6 and 7) (cf. Tables S2, S3 and S4). Compositional modes (Table S4) indicate high monocrystalline quartz (19% including dominant non-undulose and subordinate undulose and spherulitic quartz), high volcanic lithics (15 to 16% dominated by felsitic and microlitic grains) and feldspar plagioclase (8%), with subordinate sedimentary lithics (5 to 6% dominated by shale and siltstone) and polycrystalline quartz (5 to 6%). Other minor minerals include muscovite, biotite and chlorite, organic matter, extrabasinal carbonate grains, potassium feldspar, accessory minerals (i.e. zircon and iron oxides) and metamorphic grains (Figs S4 and S5). Plagioclase feldspar is the dominant feldspar type, with a P/F ratio between 0.6 and 1.0 (average 0.84) (Table S4) (Dickinson, 1970). The ratio of total volcanic lithics to total lithics (Lv/Lt) ranges between 0.4 and 0.9 (averaging 0.6) because the volcanic lithics are dominant (Figs 6 and 7). Felsitic volcanic grains have seriate or granular texture, microlitic grains have pilotaxitic and trachytic texture, lathwork grains have lathwork or hyalophitic texture, and vitric grains have glassy or devitrified texture. The high proportions of stable monocrystalline quartz and microcrystalline felsitic volcanic lithics, and unstable aphanitic volcanic lithics, polycrystalline quartz, feldspars and micaceous crystals point to the compositional immaturity of sandstones. Note that there is no major change in sandstone compositional maturity through the stratigraphy, but sandstone textural maturity based on the intergranular mud matrix content (*sensu* Dott, 1964) decreases from SU4.2 (matrix content averaging 13%) to SU4.3 (matrix content averaging 19%) (Table S4). The variability of matrix content in lobes of the SU4.3 sandstone has been studied in detail by Martinez-Doñate *et al.* (2023).

Interpretation. Previous studies have inferred that the Los Molles Formation sandstone was sourced from the Early Andean volcanic arc, mainly based on the high content of volcanic grains in sandstone (Burgess *et al.*, 2000; Paim *et al.*, 2008; Arienti Gonçalves *et al.*, 2022; Martinez-Doñate *et al.*, 2023). However, the high proportion of volcanic grains is not sufficient to determine source in a setting with at least three volcanic sources, each with a different compositional signature (Precuyano Cycle syn-rift volcanics, Early Andean volcanic arc and Chon Aike Igneous Province) (Naipauer *et al.*, 2018; Schwarz *et al.*, 2021). The detailed analysis of component grains indicates mixing of volcanic source with plutonic and minor metamorphic basement sources (Fig. 6). This is supported by the high proportion of plagioclase relative to potassium feldspar (average ratio of 0.84), which exceeds the threshold ratio of 0.75 used to define volcanic-derived sandstone (Dickinson, 1970). The immature composition of sandstone provides little support for a mature (secondary cycle) cratonic signature, such as the late Palaeozoic metamorphic highlands of the North Patagonian Massif.

Fig. 4. Correlation panel showing the stratigraphic architecture of sandy subunits (SU4.1, SU4.2 and SU4.3) across inherited rift topography of the Eastern Catán-Lil and Chachil basins (see correlation path shown in dotted red line on Fig. 5) and location of the Tuff 1 and Tuff 2 samples and sandstone samples. Note that the main datums used to correlate units are indicated by white dotted lines. The bright green layers correspond to clastic injectites, blue layers to thick debrites and purple layers to slumps.

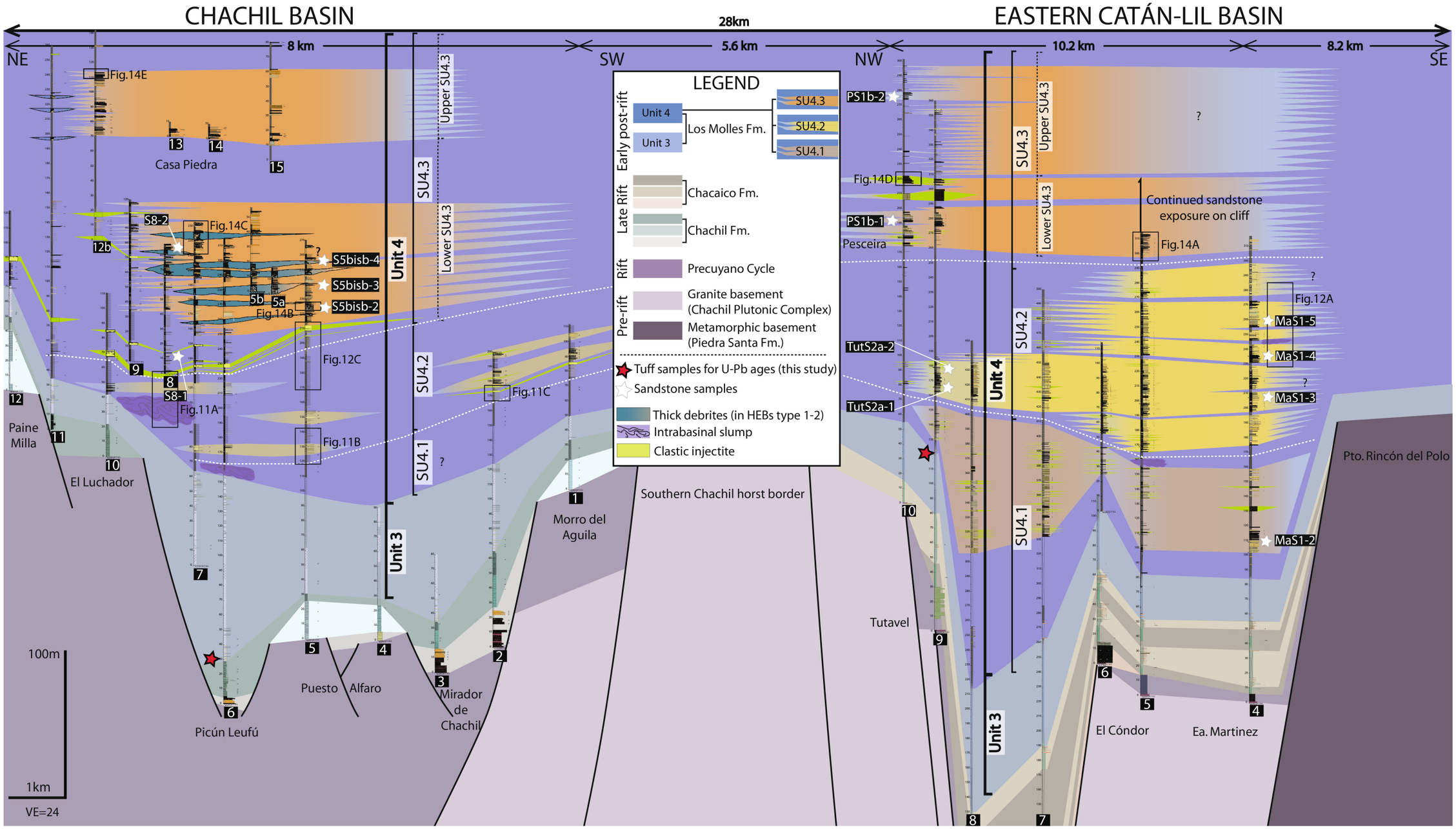

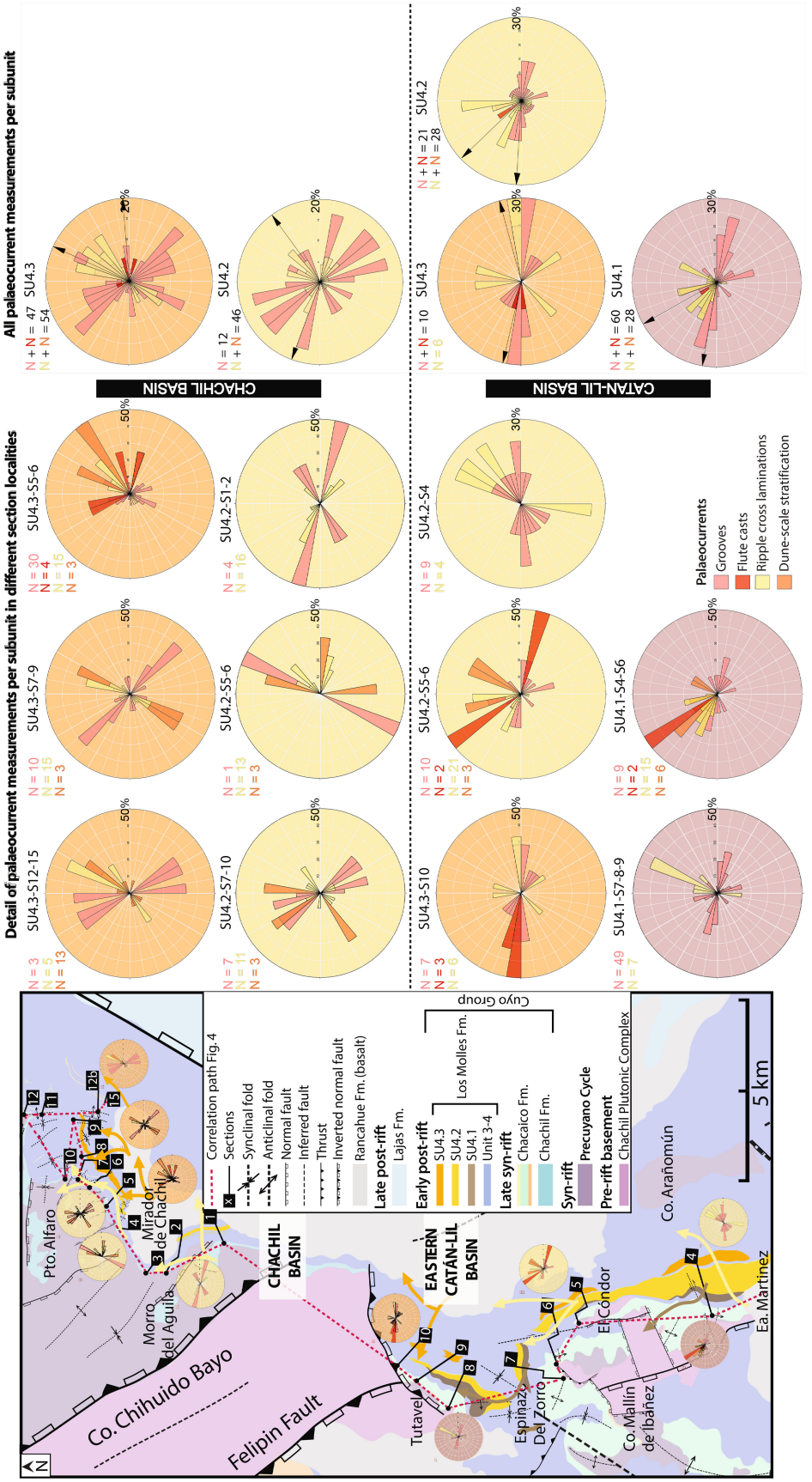

Fig. 5. Detailed map of the two Eastern Catán-Lil and Chachil depocentres investigated showing the location of logs collected, spatial distribution of sandy subunits and palaeocurrents. Palaeocurrents are shown as discrete datasets collected in each subunit per locality (left) [each type of measurement (grooves, flute casts, ripples and dune-scale cross-stratification) is shown independently] and all palaeocurrents collected in each subunit (right) (grooves and flute casts are integrated together and ripple and dune-scale cross-stratification are integrated together, in order to provide a more global overview of the dominant palaeoflow directions).

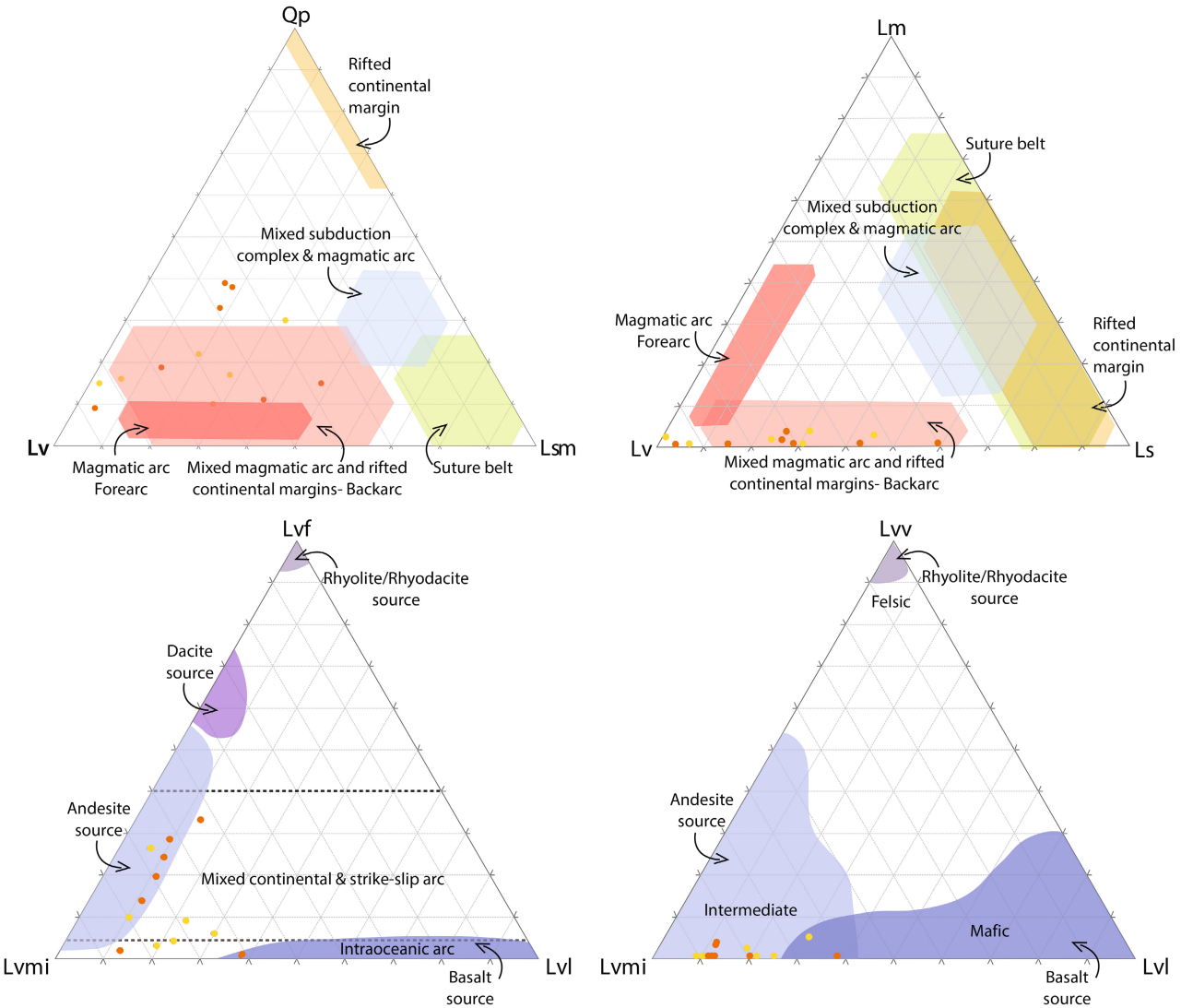

Fig. 6. Sample distribution in standard ternary diagrams with yellow dots corresponding to samples of SU4.1 and SU4.2 (MaS1-2, MaS1-3, MaS1-4, MaS1-5, TutS2a-1, TutS2a-2) and orange dots correspond to samples of SU4.3 (PS1b-1, PS1b-2, S5bisb-2, S5bisb-3, S5bisb-4, S8-1, S8-2). Qp-Lv-Lsm diagram (Dickinson & Suczek, 1979) shows the proportions of polycrystalline quartz (Qp), volcanic lithics (Lv) and sedimentary and metamorphic lithics (Lsm) with provenance fields from Ingersoll & Suczek (1979). Lm-Lv-Ls diagram (Ingersoll & Suczek, 1979) shows the proportions of different lithics including volcanic (Lv), metamorphic (Lm) and sedimentary grains (Ls). Both diagrams show that dominant provenance fields are mixed magmatic arc and rifted continental margins (backarc). Lvv-Lvmi-Lvl diagram shows the proportions of vitric (Lvv), microlitic (Lvmi) and lathwork (Lvl) volcanic grains. Lvf-Lvv-Lvl diagram shows the proportions of felsitic (Lvf), vitric (Lvv) and lathwork (Lvl) volcanic grains. Both diagrams show dominant contribution from intermediate and mafic volcanic sources (cf. fields after Marsaglia & Ingersoll, 1992, Critelli & Ingersoll, 1995; Critelli *et al.*, 2023). For detailed recalculated parameters and grain categories see Tables S2 and S3.

Instead, the recognized crystalline source contribution could originate from progressive unroofing of the Early Jurassic magmatic arc (western Coastal Cordillera and Subcordilleran batholith), corresponding to metamorphic basement and plutons of the Early Andean magmatic arc, which were eroded during subduction-triggered uplift and exhumation (e.g. Marsaglia *et al.*, 1995). The high proportion of felsic volcanic lithics record granular textures, suggesting a silicic volcanic source typical of dacite and rhyolite, and seriate textures, indicating an intermediate volcanic source more typical of dacite and andesite (e.g. Dickinson, 1970; Critelli & Ingersoll, 1995). Such felsic components are found in major quantities in syn-rift deposits associated with bimodal

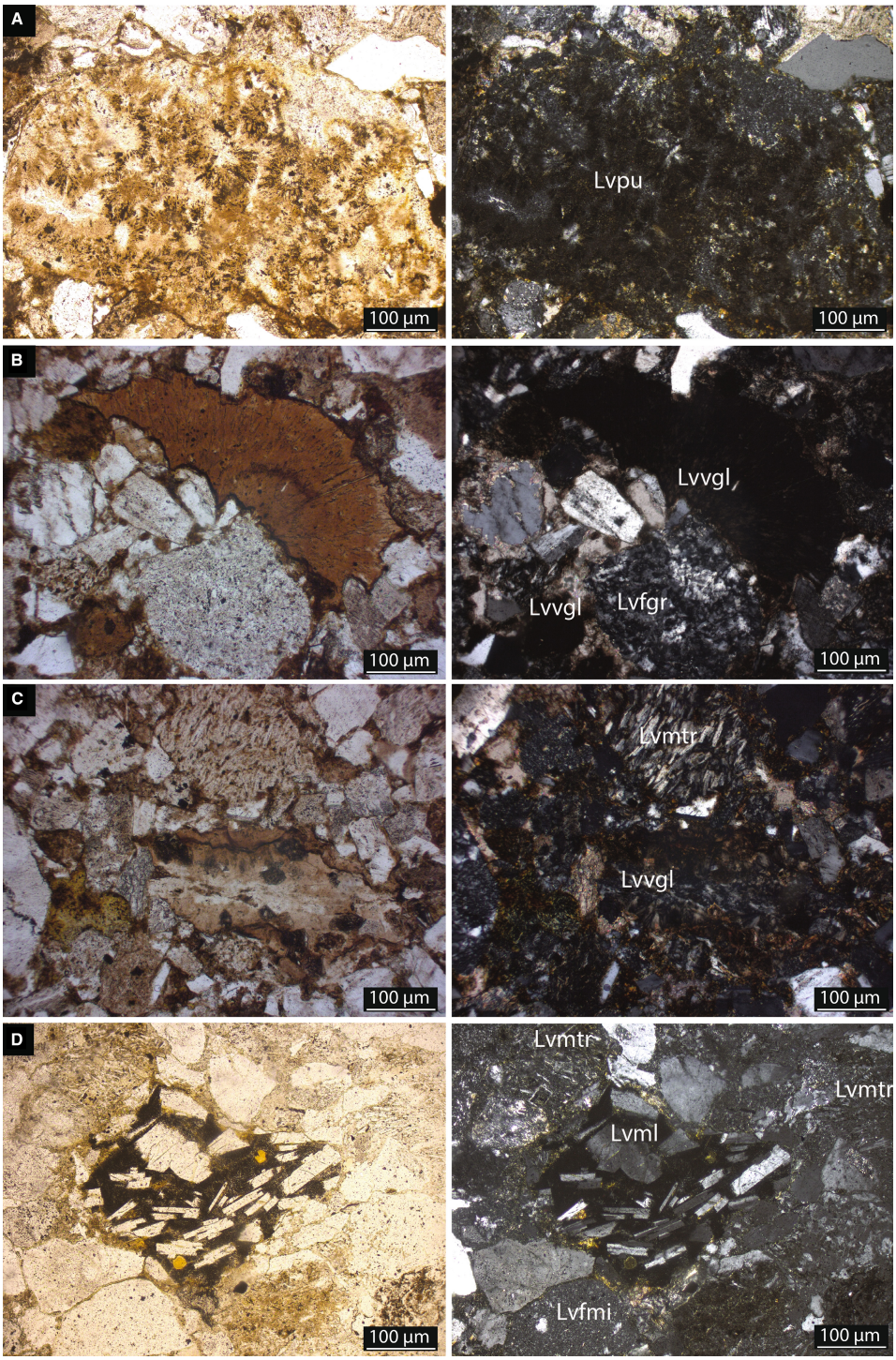

Fig. 7. Examples of thin-sections used for provenance study. Images are shown in plane-polarized light on the left and cross-polarized light on the right. (A) Example of MaS1-3 thin section showing a fragment of pumice (Lvpu) with spherulitic devitrification preserving tube vesicles and recrystallized cryptocrystalline texture. Note the pseudomatrix. (B) Example of MaS1-4 thin section showing a glassy volcanic lithic (Lvvgl) with typical ragged margins and felsitic fragment with granular texture (Lvfgr). (C) Example of MaS1-4 thin section showing microlitic volcanic lithic with trachytic texture (Lvmtr) and devitrification texture of glassy fragment (Lvvgl). Note the drusy calcite cement. (D) Example of MaS1-4 thin section showing microlitic volcanic lithic with lathwork (Lvml) and trachytic texture (Lvmtr) and felsitic volcanic lithic with recrystallized microcrystalline texture (Lvfmi). See Fig. 4 for locations of the thin-sections and Figs S5 and S6 for supplementary thin sections.

magmatism (Marsaglia *et al.*, 1995), here consistent with an interpretation as recycled Precuyano Cycle deposits (Bermudez *et al.*, 2002; Muravchik *et al.*, 2011). The relatively constant amount of microlitic volcanic grains, which are dominated by pilotaxitic and trachytic textures, support an intermediate volcanic source typical of andesite, and the subordinate lathwork and hyalophytic textures indicate an intermediate to mafic volcanic source typical of basaltic andesite and basalt. Therefore, the mixed felsic and intermediate–mafic source composition of volcanic grains in the investigated rift-margin distal depocentres, could reflect primary and reworked volcanic deposits (e.g. Marsaglia & Ingersoll, 1992) sourced from the volcanic island arc margin. Andesitic–dacitic volcanoes and intermediate–silicic calderas that developed across the Early Andean volcanic island arc (De la Cruz & Suárez, 1997) would have been the main volcanic source. This contrasts with the high content of silicic volcanic fragments in samples of equivalent strata in the adjacent Chacaico Basin (equivalent to the base of Unit 4 in this study), interpreted to reflect sand supply from a large rhyolitic-dominated province (Chon Aike Igneous Province, Naipauer *et al.*, 2018). This implies an ultra-long distance for sediment routing from an eastern source in North-eastern Patagonia (*ca* 500 km south-east of the study area) (see palaeogeographical reconstructions in Naipauer *et al.*, 2018; Schwarz *et al.*, 2021), compared to the relatively short distance for sediment supply from the Early Andean volcanic arc (*ca* 30 km south-west of the study area) (see palaeogeographical reconstructions in De la Cruz & Suárez, 1997).

In summary, this analysis of the textural and compositional characteristics of the Los Molles Formation sandstone, with consideration of potential transport pathways in the studied basins, is more consistent with a dominant Early Andean volcanic source and subordinate incorporation of recycled syn-rift sediments. The degradation of inherited rift topography could have enhanced provenance contribution from the recycled Precuyano Cycle syn-rift deposits, with mixing via erosion along routing pathways and degradation of topography.

FACIES ASSOCIATIONS AND KEY BED TYPES

The sandy subunits SU4.1, SU4.2 and SU4.3 of the Los Molles Formation in the Eastern Catán-Lil and Chachil basins each comprise lobe sub-environments (i.e. axis, off-axis, fringe) with different facies characteristics in terms of grain-size range, sorting, matrix content, nature of clasts, bedforms and bed types, enabling definition of 11 facies associations (Table 1) (Fig. 4). The facies associations include: lobe-axis (FA4.1.1, FA4.2.1 and FA4.3.1); lobe off-axis (FA4.1.2, FA4.2.2 and FA4.3.2); lobe fringe (FA4.1.3, FA4.2.3 and FA4.3.3); lower slope with scour-fills (FA4.3.4); and sand-starved lower slope to base-of-slope (FA4.4). These deposits record high to low-density turbidity currents, transitional flows, hybrid flows, debris-flows and slumps, mudflows and hypopycnal plumes (Table 1).

Within the lobe facies associations, 12 key bed types were identified (see Table 2 and Fig. 8) including High Density Turbidite bed types (HDTs 1 and 2), Transitional Flow Deposits bed types (TFDs 1 to 5) and Hybrid Event Bed types (HEBs 1 to 5) with variable occurrence and distribution in lobe sub-environments (see Table 1). The divisions that comprise the bed types are described below (cf. Table 2) and include: (i) basal clean or matrix-bearing sandy divisions; (ii) sandy bedform divisions (clean, matrix-poor, heterolithic or matrix-rich); (iii) banded divisions; (iv) clast-rich sandy divisions; (v) sandy or muddy debritic divisions; and/or uppermost (vi) structured turbidite or mudstone cap divisions. Note that, based on matrix quantification in this study (SU4.2 and SU4.3) and Martinez-Doñate *et al.* (2023) (SU4.3), it is possible to distinguish clean (10 to 12% matrix), matrix-poor (12 to 20%), heterolithic (20 to 25%), matrix-rich (25 to 40%) and debritic (>40%) divisions (Fig. 8).

In the studied system, the HEBs involve a basal division emplaced by transitional flows (*sensu* Baas *et al.*, 2009; cf. Privat *et al.*, 2021), as documented elsewhere (e.g. Kane & Pontén, 2012; Baker & Baas, 2020; Baas *et al.*, 2021a), instead of turbulent flows as in the original definition of HEBs (cf. Haughton *et al.*, 2009). A range of TFD bed types (TFDs 1 to 5) are also identified, consisting of various bedforms (banding, low amplitude bedwaves, mud-rich large ripples, swale-like and hummock-like heterolithic sandy bedforms, biconvex ripples) deposited by mud-rich transitional flows (Baas *et al.*, 2009, 2016; Stevenson *et al.*, 2020; Taylor *et al.*, 2024), which record flow transformation. The TFDs are distinctive from the HEBs, the latter being deposited by both transitional flow (lower) and debris-flow (upper) components (Baas *et al.*, 2009; Peakall

Table 1. Facies association table with bioturbation index (BI) following Taylor & Goldring (1993). RXL: Current ripple cross-lamination; CRXL: Climbing ripple cross-lamination; LXL: low-angle cross-lamination; PL: Planar lamination; SinL: Sinusoidal lamination; SigXL: Sigmoidal lamination; Step.L: Stepped lamination; Tc: Traction carpet; TXS: Trough cross-stratification; SSD: Soft sediment deformation; HCS/SCS: Hummocky or swaley cross-stratification; BiRXL: Biconvex ripples; Gr: Granule; VCs: Very coarse-grained sandstone; Cs: Coarse-grained sandstone; Ms: Medium-grained sandstone; Fs: Fine-grained sandstone; VFs: Very fine-grained sandstone; HDT: High-density turbidite; HEB: Hybrid event bed; LDT: Low-density turbidite; TFD: Transitional flow deposit; LPF: Laminar plug flow; LTPF: Lower transitional plug flow; QLPF: Quasi-laminar plug flow; TETF: Turbulence-enhanced transitional flow; UTPF: Upper transitional plug flow. For more detail on HDTs 1–2, HEBs 1–5 and TFDs 1–5 bed types, see Figure 8, Table 2 and main text.

Facies Association (FA)	Description	Interpretation
FA4.1.1: Thick-bedded matrix-rich sandstone packages (1.0–4.8 m thick *ca* 2.5 m)	Weakly amalgamated sandstone beds (0.8–2.6 m thick) with thin silty mudstone interbeds (2–10 cm thick), dominated by TFDs 3 (0.5–1.2 m thick) and few HDTs 2 (0.2–0.6 m thick). Sandstone beds (Ms–Fs) are poorly sorted, matrix-rich and massive to weakly normally graded with a muddier finer-grained top that can be laminated (PL). Base of beds can bear a few mudstone clasts (2–10 cm long) and outsized coarse grains. Beds are tabular, with erosive (grooves) or loaded base (flames) and sharp or amalgamated top	Marginal lobe-axis to off-axis (Prélat *et al.*, 2009; Kane & Pontén, 2012) dominated by transitional flows, rapidly decelerated LTPF to UTPF (Baas *et al.*, 2009) and collapsing suspension clouds forming muddy caps (Pickering & Hiscott, 1985). Grooves suggest the passage of high-strength quasi-laminar or laminar flows (Peakall *et al.*, 2020)
FA4.1.2: Medium to thick-bedded matrix-rich sandstone and silty mudstone packages (6–29 m thick *ca* 16.6 m)	Interbedded sandstone and sandy siltstone beds (0.2–1.0 m thick) with mudstone, including rare HEBs 3 (0.2–0.5 m thick) and stand-alone clast-rich chaotic sandy mudstone beds. Sandstone beds (Ms–Fs) are poorly sorted, massive to weakly normally graded, with deformed mudstone clasts (5–10 cm long) throughout or at top, sandy siltstone beds are normally graded and laminated (PL, RXL). Beds are tabular with a sharp planar or erosive base (grooves) and sharp planar top. Strata can be cross-cut (<15°) by subhorizontal sandstone bodies (0.2–0.8 m thick, hundreds of metres to 1 km across) that are massive or planar laminated, with sharp planar or stepped margins and pinchout terminations	Lobe off-axis (Prélat *et al.*, 2009; Kane & Pontén, 2012) dominated by transitional flows, rapidly decelerated LTPF to UTPF (Baas *et al.*, 2009) and few low to intermediate yield strength, sand-rich debris-flows (Talling *et al.*, 2012). Note the paucity of HEBs compared to FA4.2.2 and FA4.3.2. Beds can be remobilized into clastic sills, with post-depositional fluidization and propagation of injectites with brittle deformation of compacted muddy substrate by laminar flows (Hurst *et al.*, 2003; Cobain *et al.*, 2015)

Table 1. (continued)

Facies Association (FA)	Description	Interpretation
FA4.1.3: Thin to medium-bedded mudstone-dominated heterolithic packages (3.4–65 m thick *ca* 16.9 m)	Interbedded silty sandstone (Fs–VFs), siltstone and mudstone beds (0.01–0.4 m thick) (Chondrites; BI: 0–1). Beds are normally graded and laminated (PL, RXL) or massive with mudstone clasts (1–5 cm long) throughout and tabular with sharp planar base and top, or gradational top	Lobe fringe (Mutti, 1977; Prélat *et al.*, 2009; Boulesteix *et al.*, 2019) dominated by waning low-density turbulent flows and muddy flow tails (Stow & Bowen, 1980; Lowe, 1982) and low yield strength, sand-rich debris-flows (Talling *et al.*, 2012)
FA4.2.1: Medium to thick-bedded matrix-poor sandstone packages (0.9–11.7 m thick, *ca* 2.5 m)	Amalgamated sandstone beds (0.5–2.6 m thick) dominated by HDTs, including clast-rich HDTs 2 (0.2–0.6 m thick) and TFDs 1 (0.5–1.2 m thick), few clast-poor sand-rich HEBs 5 (0.5–0.8 m thick) and muddy HEBs 2 (0.2–0.6 m thick) clustered at base of lobes. Turbidite sandstone beds (Ms–Fs) are poorly sorted and crudely normally graded. It includes few bioclasts (ammonite rostrums, bivalves), subrounded clasts of blueish siltstone and grey mudstone (2–5 cm long) and outsized green to purple epiclastic volcanic lithics (VCs–Gr) often at base. Top can be laminated with small-scale sandy bedforms (PL, CRXL to RXL, LXL, SinL) or large-scale heterolithic sandy bedforms with carbonaceous-rich muddy foresets and mud drapes (SCS–HCS, BiRXL) (TFDs 1). HEBs 5 are matrix-rich and massive with a few mudstone and carbonaceous clasts (2–8 cm long) at top. Beds are tabular, with loaded or erosive base (grooves, flute casts) with clast-rich basal lags, locally scoured (0.6–4.4 m deep, 10–50 m long) and gradational or sharp planar top	Lobe axis (Prélat *et al.*, 2009; Etienne *et al.*, 2012) dominated by high-density turbidity currents (Lowe, 1982) and transitional flows (Baas *et al.*, 2009). HDTs record rapid suspended sediment load fallout of high-density turbidity currents and tractional reworking by slowly decelerated medium to low-density turbulent flows. Rapid deposition from relatively high near-bed sediment concentration and suspension fallout enabled high bedform aggradation and migration rate (Allen, 1973). Locally, mudstone clast top division developed due to incorporation of mudclasts travelling as bedload at top of bed (HDTs 2). TFDs record deposition by slowly decelerated, TETF to LTPF with increased clay concentration and attenuated nearbed turbulence (Baas *et al.*, 2016; Stevenson *et al.*, 2020), enabling heterolithic sandy bedforms that could indicate combined-flow processes (e.g. Tinterri, 2011; Ge *et al.*, 2017). Few HEBs record deposition by rapidly decelerated, LTPF to UTPF and QLPF to LPF (Baas *et al.*, 2009; Peakall *et al.*, 2020), corresponding to low yield strength, sand-rich (HEBs 5) or high yield strength muddy (HEBs 2) debris-flows (Talling *et al.*, 2012) common at base of lobe axis. Basal sandy division of HEBs 2 can be remobilized into clastic sills or dykes prior to, or after, compaction with brittle fracturing (Hurst *et al.*, 2003; Cobain *et al.*, 2015)

Table 1. (continued)

Facies Association (FA)	Description	Interpretation
FA4.2.2: Medium to thick-bedded matrix-poor sandstone-dominated heterolithic packages (2.0–26.6 m thick, *ca* 14.5 m)	Sandstone beds (0.5–2.0 m thick) include HDTs, matrix-poor TFDs 2 (0.2–0.5 m thick) and clast-poor sand-rich HEBs 5 (0.5–0.8 m thick), locally amalgamated or interbedded with mudstone-dominated heterolithic strata (FA4.2.3) (Chondrites, Planolites; BI: 2–3). Sandstone beds (Ms–Fs) are massive with few mudstone and carbonaceous clasts (5–8 cm long) or normally graded with laminated top (PL, RXL), or with matrix-poor sandy bedforms with carbonaceous-rich muddy foresets (HCS, BiRXL, RXL) (TFDs 2). HEBs 5 are matrix-rich and massive with a few mudstone and carbonaceous clasts (2–8 cm long) at top. Beds are tabular, with sharp planar or locally erosive base and gradational or sharp top, rarely amalgamated (<1 m thick). Strata can be cross-cut (<5°) by subhorizontal sandstone bodies (0.5–1.2 m thick, several kilometres across), massive or planar parallel laminated, with subangular mudstone clasts (5–30 cm long), with sharp planar or stepped margins and pinchout terminations	Lobe off-axis (Prélat *et al.*, 2009; Spychala *et al.*, 2017) dominated by waning moderate to low-density density turbidity currents with traction-plus-fallout (Lowe, 1982) and transitional flows (Baas *et al.*, 2009). TFDs record deposition by slowly decelerated, TETF to LTPF (Baas *et al.*, 2016; Stevenson *et al.*, 2020) enabling matrix-poor bedforms that could indicate combined-flow processes (e.g. Tinterri, 2011; Ge *et al.*, 2017). HEBs record deposition by rapidly decelerated, LTPF to UTPF (Baas *et al.*, 2009), corresponding to low yield strength, sand-rich (HEBs 5) debris-flows (Talling *et al.*, 2012). Cross-cutting sandstone bodies correspond to clastic sills which record local erosion of compacted muddy substrate
FA4.2.3: Thin to medium-bedded mudstone-dominated heterolithic packages (1.0–22.4 m thick, *ca* 10.1 m)	Interbedded sandstone dominated by LDTs, matrix-poor TFDs 2 (0.2–0.5 m thick) and with few clast-poor sand-rich HEBs 5 (<0.5 m thick), with sandy siltstone and silty mudstone beds (0.1–0.2 and up to 2 m thick) with mudstone. Sandstone beds (Fs–VFs) and siltstone are massive to normally graded and laminated (PL, RXL, SinL, SSD, convolute laminae and flames), or with banded to matrix-poor sandy bedforms (HCS, BiRXL, RXL) (TFDs 2). HEBs 5 are matrix-rich and massive with a few mudstone and carbonaceous clasts (2–8 cm long) at top or throughout. Beds are tabular with sharp planar base and sharp or gradational top. Strata can be cross-cut (<15°) by subhorizontal sandstone bodies (0.2–0.5 m thick, 10–100 m across) with sharp planar or stepped margins locally mantled with subangular or subrounded mudstone clasts (2–10 cm long) or subvertical sandstone bodies (5–15 cm wide, 10–30 cm high) showing ptygmatic folds and abrupt pinchout	Lobe fringe (Prélat *et al.*, 2009; Spychala *et al.*, 2017) dominated by waning low-density turbulent flows, locally with common water-escape structures (SSD) suggesting rapid deposition (Allen, 1982). TFDs including banded and sandy bedform division, record deposition by moderately to slowly decelerated, LTPF to UTPF (Baas *et al.*, 2009). HEBs record deposition by moderately decelerated, LTPF to UTPF (Baas *et al.*, 2009), corresponding to low yield strength, sand-rich (HEBs 5) debris-flows (Talling *et al.*, 2012). Locally, beds can be remobilized into clastic sills or dykes (Hurst *et al.*, 2003; Cobain *et al.*, 2015), which ptygmatic folds record as emplaced in uncompacted strata (Kuenen, 1968)

Table 1. (continued)

Facies Association (FA)	Description	Interpretation
FA4.3.1: Medium to thick-bedded matrix-poor sandstone packages (1.5–5.0 m thick, *ca* 3 m)	Amalgamated sandstone beds (0.4–1.0 m thick) dominated by HDTs, including HDTs 1 (0.4–1.0 m thick) and matrix-rich TFDs 3 (0.4–0.8 m thick) and TFDs 5 (0.2–0.5 m thick). Locally intervening silty mudstone interbeds (5–15 cm thick) or clast-rich muddy HEBs 1 (1–7 m thick). Sandstone beds (Cs–Ms) are poorly sorted, crudely normally graded and massive or laminated (Step.L, TCs) and with basal coarse-tail normal or inverse grading (VCs, Gr). It includes subangular dark grey mudstone or rare subrounded siltstone clasts (5–20 cm long) and few bioclasts (common bivalves and rare ostreid shells, foraminifera, small ammonites) and few armoured mudstone clasts (2–6 cm long) with quartz granules. Top of beds can present large-scale clean sandy bedforms (DXS and RXL) locally associated with scour-fills (TXS) with mudstone clast-rich basal foresets (HDTs 1), or matrix-rich sandy bedforms (mud-rich bedwaves, RXL) (TFDs 3), or banded sandstone (TFDs 5), locally incised by mud-filled scours (40 cm deep, *ca* 3 m wide). Beds are tabular with erosive (grooves, rare flute casts) or loaded base (flames) and amalgamated top. Sandy scours (1.5 to 2.0 m deep, *ca* 5 m long) are infilled by low-angle (<10°) cross-stratified bedsets (20–80 cm thick foresets) bearing rip-up mudstone clasts (5–10 cm long)	Lobe axis (Prélat *et al.*, 2009; Etienne *et al.*, 2012) dominated by high-density turbidity currents (Lowe, 1982) and transitional flows (Baas *et al.*, 2009). HDTs record coarse bedload deposition from high-density flows, with high aggradation rates and collapse of high-concentration near-bed sheared layers (Lowe, 1982; Sumner *et al.*, 2008). Local inverse basal grading suggests rapid flow deceleration and kinetic sieving (Legros, 2002; Dasgupta & Manna, 2011). Large-scale clean sandy bedforms with basal grain-size break and associated with scours record reworking at top of beds from bypassing flows (Mutti *et al.*, 2003; Stevenson *et al.*, 2015). TFDs with matrix-rich bedforms record deposition by slowly decelerated, LTPF to UTPF compared to the banded sandstone developed under moderately decelerated UTPF (Baas *et al.*, 2011; Stevenson *et al.*, 2020). Locally, HEBs 1 record deposition by moderately to rapidly decelerated, LTPF to UTPF and QLPF (Baas *et al.*, 2009), corresponding to intermediate to high yield strength, muddy debris-flows (Talling *et al.*, 2012). The abundance of grooves, compared to rare flute casts, suggests that the bulk of cohesive flows bypassed towards more distal settings (Peakall *et al.*, 2020)
FA4.3.2: Thick or medium to thin-bedded matrix-rich sandstone-dominated heterolithic packages (2.0–26.6 m thick, *ca* 14.5 m)	Sandstone beds (0.1–0.6 m thick) include LDTs, matrix-rich TFDs 4 and TFDs 5 (0.2–0.5 m thick) and clast-rich muddy HEBs 1, HEBs 3 (0.2–0.5 m thick) and HEBs 4 (0.4–1.0 m thick), rarely amalgamated or interbedded with mudstone-dominated heterolithic strata (FA4.3.3). Sandstone beds (Ms–Fs) are poorly sorted and massive or normally graded locally with laminated top (PL, RXL), or with matrix-rich sandy bedforms (mud-rich bedwaves, HCS, BiRXL) (TFDs 4), or banded sandstone (TFDs 5). Beds are tabular or with pinch and swell geometry, sharp planar or erosive base (grooves) and gradational or sharp top	Lobe off-axis (Prélat *et al.*, 2009; Spychala *et al.*, 2017) dominated by transitional flows (Baas *et al.*, 2009) and debris-flows (Talling *et al.*, 2012) and waning moderate to low-density turbulent flows (Lowe, 1982). TFDs with banding record deposition by moderately decelerated, UTPF with propagation of low-amplitude bedwaves, compared to slowly decelerated, LTPF to UTPF (Baas *et al.*, 2016; Stevenson *et al.*, 2020) enabling matrix-rich bedforms that could indicate combined-flow processes (e.g. Tinterri, 2011; Ge *et al.*, 2017). HEBs record deposition by moderately to rapidly decelerated, LTPF to UTPF and QLPF (Baas *et al.*, 2009), corresponding to intermediate, sand-rich (HEBs 3) and high yield strength, muddy (HEBs 4) debris-flows (Talling *et al.*, 2012)

Table 1. (continued)

Facies Association (FA)	Description	Interpretation
FA4.3.3: Thin to very thin-bedded mudstone-dominated heterolithic packages (2–10 m thick, *ca* 5.5 m)	Interbedded sandstone, siltstone and silty mudstone beds (5–20 cm thick) (Chondrite, Planolites, Nereites; BI: 3–4) with pin-striped sandy to silty laminated mudstone, including thin TFDs 5 (0.2 m thick) and clast-rich muddy HEBs 3 and 4 (0.2–0.4 m thick), and thicker stand-alone clast-rich chaotic sandy mudstone beds (0.1–0.6 m thick). Sandy or mud-filled scours (10–15 cm deep, *ca* 1 m long) are present. Sandstone beds (Ms–Fs) are massive with mudstone clasts (2–5 mm long), or laminated (PL, RXL, few BiRXL with sigmoidal foresets (<5°) (2–6 cm thick, 10–15 cm wavelength) with opposite or oblique palaeoflow directions) or banded (TFDs 5). Beds are tabular or with pinch and swell geometry, sharp planar base and sharp or gradational top. Chaotic sandy mudstone beds are associated with subvertical sandstone bodies (5–15 cm wide, 10–30 cm high) showing ptygmatic folds and pinchout terminations. Subhorizontal sandstone bodies (0.2–3.0 m thick, 5 km across) cross-cut (<15°) strata, bearing angular rafts (10–50 cm thick, >1 m across) with long axis parallel to bedding of host strata and sharp planar or stepped margins locally mantled with mudstone clasts (2–5 cm long)	Lobe fringe (Prélat *et al.*, 2009; Spychala *et al.*, 2017) dominated by waning medium to low-density turbidity currents (Lowe, 1982) and transitional flows (Baas *et al.*, 2009), with minor debris-flows (Talling *et al.*, 2012). TFDs with banding record deposition by moderately decelerated, UTPF with propagation of low-amplitude bedwaves (Baas *et al.*, 2011; Stevenson *et al.*, 2020). HEBs record deposition by moderately to rapidly decelerated, LTPF to UTPF and QLPF (Baas *et al.*, 2009), corresponding to intermediate, sand-rich (HEBs 3) and high yield strength, muddy (HEBs 4) debris-flows (Talling *et al.*, 2012). Stand-alone muddy debrites record high yield strength muddy debris-flows (Talling *et al.*, 2012) and associated clastic dykes emplaced shortly after debrite deposition, as indicated by ptygmatic folds (Kuenen, 1968). The large clastic sills record post-depositional fluidization and propagation with significant brittle deformation and erosion of compacted muddy substrate (Hurst *et al.*, 2003; Cobain *et al.*, 2015) in comparison to clastic sills in SU4.2 or SU4.1
FA4.3.4: Thick to medium-bedded matrix-poor sandstone and sandy heterolithic packages (2–10 m thick)	Amalgamated sandstone (up to 2 m thick, 1.0–1.5 km wide) thinning and pinching-out laterally, sandy heterolithic lens-shaped packages (5–10 m thick, 200–300 m wide) shaling-out laterally and subhorizontal clast-rich sandstone bodies with abrupt pinchout terminations are found isolated in mudstone including stand-alone clast-rich chaotic mudstone beds (FA4.4). Sandstone beds (VCs–Ms) are massive, with coarse-tail normal grading of granules and crushed shells, with subangular siltstone clasts at base and/or mudstone rip-up clasts (2–3 cm long) and top can be cross-stratified (20–50 cm thick foresets). Sandy heterolithics include thin-bedded sandstone (Ms–Fs), sandy siltstone and mudstone, normally graded and laminated (PL, RXL). Subhorizontal mudstone clast-rich sandstone bodies are massive, breccia-like as full of subangular mudstone clasts (8–15 cm long) with long-axis parallel to bedding and have sharp margins and pinchout	Lower slope with isolated sand-filled or heterolithic-filled large scours which record erosion, bypass and deposition from basal concentrated part of high-density turbidity currents, with high suspended sediment fallout rates and bedload traction (Lowe, 1982) or with traction-plus-fallout from waning medium to low-density flows (Lowe, 1982). Bioclastic material is more common than in FA4.2.1 or FA4.3.1, suggesting proximity from source. These deposits could correspond to short-lived gullies passively filled and/or represent disconnected lobes (Brooks *et al.*, 2018). The clast-rich breccia-like sandstone bodies could record fluidization and remobilization of shallowly-buried sandy gullies

Table 1. (continued)

Facies Association (FA)	Description	Interpretation
FA4.4: Very thin to thin-bedded mudstone-dominated succession (tens to hundreds of metres thick)	Siliciclastic mudstone with wispy laminae (clay, silt and volcanic grains, phytodetritus) and massive silty mudstone, weakly bioturbated (Chondrites, Teichichnus, Phycosiphon; BI: 2–3) bearing ammonites and bivalves (abundant *Bositra sp.*). Thin beds of tuff, siltstone and sandstone (0.05–10.0 cm thick), massive or laminated and carbonaceous-rich (PL, RXL) with sharp planar or loaded base and gradational or sharp top are present. Clast-rich chaotic mudstone beds (0.1–0.6 m thick) bearing muddy and siltstone clasts (5–15 cm long), with irregular wavy top and sharp base can occur. Contorted/folded beds (1–5 m thick, 1–2 km across) of deformed mudstone and siltstone occur locally, with overturned to recumbent folds (1–5 m amplitude) indicating a dominant fold vergence towards the north-east. Strata is often cross-cut by subvertical (5–20 cm thick, 0.2–1 m high) and subhorizontal (ranging from 15 cm to 80 cm thick, 1 km across) sandstone bodies, also cross-cutting one another, with sharp planar or stepped margins and abrupt pinchout terminations	Sand-starved lower slope to base-of-slope, normally oxygenated, receiving dilute terrigenous influxes at distance from the locus of sandy fans (Boulesteix *et al.*, 2019) with local sediment destabilization and soft sediment deformation (slumps, muddy debrites, clastic injectites). Mudstone records settling from suspension of muddy/silty clouds, high concentration mudflows (McCave & Jones, 1988) and potentially hypopycnal plumes given the presence of phytodetritus (Paim *et al.*, 2011). Suspension fallout from ash plumes and waning low-density turbidity currents (Stow & Bowen, 1980) are common. Chaotic beds record high yield strength muddy debris-flows (Talling *et al.*, 2012) and deformed beds record slump translation, with gravity-driven plastic deformation of semi-lithified intrabasinal mudstone-prone slope deposits. Slumps may have travelled across a short distance given the moderate deformation and open fold geometries (Martinsen & Bakken, 1990). Cross-cutting sandstone bodies record post-depositional fluidization and injection with brittle deformation suggested by clastic sill and dyke margins; cross-cutting relationships record multiphase injection (Hurst *et al.*, 2003; Cobain *et al.*, 2015)

Table 2. Facies table for the different bed types divisions including: (i) basal sandy divisions (clean or matrix-bearing); (ii) sandy bedform divisions (clean, matrix-poor, heterolithic or matrix-rich); (iii) banded divisions; (iv) clast-rich sandy divisions; (v) sandy or muddy debritic divisions; and/or uppermost (vi) structured turbidite or mudstone cap divisions. See Fig. 8 for the detailed occurrence of divisions in bed types.

Divisions	Bed types	Description	Interpretation
Basal sandy divisions	HDT 1 HDT 2 TFD 2 HEB 4	Clean sandstone, massive, with crude normal grading (HDT 2, TFD 2, HEB 4), or stepped laminae (HDT 1)	Deposition under high-density turbidity current with high aggradation rates and locally with collapse of high-concentration near-bed sheared layers (Lowe, 1982; Sumner *et al.*, 2008)
	TFD 1 TFD 3 TFD 4 TFD 5 HEB 1 HEB 3 HEB 5	Matrix-poor sandstone, massive with mudstone clasts (1–5 to 8 cm long) concentrated at the base (TFD 3, HEBs 1–3) or at the top (TFDs 1–4–5, HEB 5)	Deposition under lower transitional plug flows (LTPF) to upper transitional plug flows (UTPF) (Baas *et al.*, 2009), which formed a fluidal basal layer at the base of debris-flows in HEBs (cf. Peakall *et al.*, 2020; Privat *et al.*, 2021) and clasts incorporated via bedload deposition (Baas *et al.*, 2021a)
	HDT 2 TFD 1 HEB 2	Tabular or pinch-and-swell geometry, or locally injected with ptygmatic folds (*sensu* Kuenen, 1968) at the contact with the overlying debritic division (HEB 2), or with discordant convex-up or stepped margins (HDT 2, TFD 1, HEB 2)	Ptygmatic folds and stepped margins suggest post-depositional fluidization and injection of the basal sandy divisions prior to, or after, compaction with brittle fracturing (Hurst *et al.*, 2003; Cobain *et al.*, 2015)
Sandy bedform divisions	HDT 1	Clean and coarse-grained sandy bedforms (HDT 1), well-cemented, with large ripple to dune-scale cross-stratification (<15°) (25–40 cm high, 50–80 cm wavelength), adjacent to scour-fills with trough cross-stratification (15°–30°), locally bearing mudstone clasts on foresets	Relatively high amplitude and long wavelength clean sandy bedforms record reworking of coarse-grained bedload as migrating large ripples and dunes with high aggradation rate (Allen, 1973; de Cala, 2021). Scour-fills indicate erosion and bypass of high-density turbidity currents at bed top (Mutti *et al.*, 2003; Stevenson *et al.*, 2015)
	TFD 1	Matrix-poor and fine-grained sandy bedforms (TFD 1), with small hummock-like bedforms (5–10 cm high, 20–40 cm wavelength) and large biconvex ripples (10–20 cm high, 10–30 cm wavelength) with mixed sand–mud cross-laminae bearing mudchips and thin muddy carbonaceous foresets	High to low amplitude and moderate to long wavelength, matrix-poor and heterolithic sandy bedforms deposited under slowly decelerated turbulence-enhanced transitional flow (TETF) to LTPF (Fig. 8) (Baas *et al.*, 2009, 2016; Baker & Baas, 2020; Stevenson *et al.*, 2020).
	TFD 2	Heterolithic and fine-grained sandy bedforms (TFD 2), with larger biconvex ripples (15–20 cm high, 20–50 cm wavelength) and swale and hummock-like bedforms (10–20 cm high, 50–100 cm wavelength) with well-preserved extensive muddy carbonaceous foresets and mud drapes (0.5–1.5 cm thick)	Low amplitude and longer wavelength matrix-rich sandy bedforms deposited under slowly decelerated LTPF to UTPF flows (Fig. 8) (Baas *et al.*, 2009, 2016; Baker & Baas, 2020; Stevenson *et al.*, 2020). These bedforms (TFD 1–4 and HEB 1) form a continuum with different dimensions and matrix content (Fig. 8) reflecting turbulence modulation with a progressive increase in flow cohesion (Baas *et al.*, 2021b). They record deposition under combined flows with an oscillatory component developed due to flow interaction with nearby seabed topography (Tinterri, 2011) and/or bedform-scale relief (Ge *et al.*, 2017; Hofstra *et al.*, 2018)
	TFD 3 TFD 4 HEB 1	Matrix-rich sandy bedforms, with mud-rich bedwaves and mud-rich ripples (5–10 cm high, 20–50 cm wavelength) (HEB 1) or large ripples and swale and hummock-like bedforms (15–30 cm high, 40–80 cm wavelength), with smaller biconvex ripples (5–10 cm high, 15–20 cm wavelength) at top (TFDs 3–4)	

Table 2. (continued)

Divisions	Bed types	Description	Interpretation
Banded divisions	TFD 5 HEB 3 HEB 4	Thick sand-rich and mud-rich bands (1–5 mm to 2 cm thick bands) subparallel and planar, with scattered mudchips in bands (TFD 5, HEBs 3–4)	Deposition under moderately decelerated UTPF, sufficiently slow to enable a period of traction and turbulence attenuation by cohesive forces, represented by low-amplitude bedwaves; locally these record faster moving larger bedload clasts (Baker & Baas, 2020; Stevenson *et al.*, 2020)
	TFD 1	Thin sand-rich and mud-rich bands (2–5 mm to 1 cm thick bands) forming subparallel planar to low-angle undulose bedwaves, with mudstone clasts (1–5 cm long) at base (TFD 1) (*sensu* Stevenson *et al.*, 2020)	
Clast-rich sandy divisions	HDT 2	Mudstone clast-rich and matrix-poor sandstone, with tightly packed and crudely stratified subrounded oblate mudstone clasts (HDT 2) (cf. Fonnesu *et al.*, 2018)	Deposition with deceleration-induced suspension-fallout of sand, and incorporation of mudclasts travelling as much slower bedload, thus moving 'backwards' relative to the flow, whilst the suspended mud-component (matrix) is advected with the flow (see Baas *et al.*, 2021a). The relative bedload and suspended mud velocities, leads to a spatial separation of mud-rich bedload and matrix components in more proximal locations. This explains the matrix-poor nature of this division and is similar to the Mudstone-Clast-Rich Beds (MRB) that abruptly transition laterally and longitudinally into HEBs (Fonnesu *et al.*, 2015, 2018)
Sandy or muddy debritic divisions	HEB 3 HEB 5	Sand-rich debritic divisions: either swirly matrix-rich sandstone bearing carbonaceous fragments (0.5–2.0 cm long) (HEB 5), or chaotic matrix-rich sandstone with deformed siltstone and mudstone clasts (2–25 cm long) (HEB 3)	*En masse* deposition by low to intermediate yield strength debris-flows (Talling *et al.*, 2012)
	HEB 1 HEB 2 HEB 4	Mud-rich debritic divisions: either patchy sand-rich mudstone matrix bearing rare deformed mudstone clasts (5–10 cm long) (HEB 4), or with sand-poor mudstone matrix bearing subangular to subrounded floating clasts of mudstone and sandstone (locally injected) (5–40 cm long) and deformed heterolithic rafts (50–80 cm long) (HEBs 1–2)	*En masse* deposition by high yield strength debris-flows, with elevated clast buoyancy and local basal erosion (Talling *et al.*, 2012; Dakin *et al.*, 2013) (cf. Privat *et al.*, 2021). The various bioclastic material and armoured mudstone clasts with quartz granules (HEB 1) indicate long-distance transport from more proximal slope setting (Chun *et al.*, 2002; Haughton *et al.*, 2003). This suggests transformation of voluminous debris-flows of extrabasinal origin (i.e. slope failures) that evolved with co-genetic sandy divisions (Privat *et al.*, 2021)
Upper divisions	HEB 1 HEB 5	Planar laminated to ripple cross-laminated, normally graded sandstone (HEBs 1–5)	Deposition by low-density turbidity currents (Lowe, 1982) from the tail of the flow developed with dilution at the top of transitional flows and debris-flows
	TFDs 1 to 5 HEB 3 HEB 4	Ungraded massive mudstone caps (TFDs 1–5, HEBs 3–4)	Mudstone caps deposited by very low strength fluid mudflows (cf. Baas *et al.*, 2011; Talling *et al.*, 2012)

et al., 2020). In both HEBs and TFDs, the uppermost parts of an event bed are typically the products of more dilute turbiditic components, representative of the tail of the flow. In this classification (Table 2 and Fig. 8), the deposits of clay-rich flows were separated into those with (HEBs) and without (TFDs), a debritic component, respectively. This contrasts with earlier classifications, where all such deposits were grouped as Hybrid Event Beds (Haughton *et al.*, 2009) or as Transitional Flow Deposits (Kane & Pontén, 2012).

DEPOSITIONAL AND EVOLUTIONARY MODEL

To analyse the large-scale stratigraphic architecture and sedimentological characteristics of the deep-water deposits of Unit 4, and their evolution across inherited rift topography in the Eastern Catán-Lil and Chachil basins, a hierarchical approach (Prélat *et al.*, 2009) is taken to define several lobe complexes following the criteria of Prélat & Hodgson (2013). Tabular packages of several metres thickness bounded by surfaces marking abrupt facies changes are lobes, and lobe complexes are defined by several lobes separated by an extensive mudstone interval of several metres to 10 m thickness, which could represent distal lobe fringe with lobe backstepping, or avulsion with lateral lobe switching (Prélat & Hodgson, 2013). In this context, each sandy subunit (SU4.1, SU4.2 or SU4.3) is interpreted to represent a single depositional system (i.e. an intraslope submarine fan) separated by a thick mudstone succession (15 to 70 m thick) (Fig. 4) marking a fan-wide break in sand supply (Prélat & Hodgson, 2013). This section compares the characteristics of the different subunits across the two basins, including; the architecture, stacking and stratal termination patterns of lobe complexes, and the proportion of facies associations (Table 1) and bed types (cf. close-up correlation panels Fig. S3).

Subunit 4.1

Lobe characteristics (SU4.1)

Subunit SU4.1 (18 to 95 m thick) forms an overall low sandstone content succession of interbedded matrix-rich, locally amalgamated fine-grained sandstone and mudstone beds, with common clastic injectites (Figs 4 and 9). SU4.1 matrix-rich lobes (1.0 to 4.8 m thick), are fine-grained, structureless and clast-poor (exclusively dark grey intrabasinal mudstone clasts), and lack coarse sand grain-sizes compared to SU4.2 matrix-poor lobes (Fig. 10). This suggests deposition by high-efficiency, clay-rich sluggish flows with dampened turbulence, dominantly transitional flows (Baas *et al.*, 2009) (Table 1). The relatively isolated occurrence of lobe-axis and off-axis deposits (FA4.1.1–FA4.1.2) in mudstone-prone strata (Fig. 9A) suggests that flows incorporated clay material through entrainment of muddy substrate draped above inherited rift topography (Unit 3) and developed 'dirty' lobes in relatively distal parts of the system (e.g. Shumaker *et al.*, 2018).

Lobe-axis (FA4.1.1) and *lobe off-axis deposits* (FA4.1.2) are dominated by clast-bearing transitional flow deposits (similar to TFD 3) with few high-density turbidites (HDT 2) (Fig. 9B), and HEBs (HEB 3) or stand-alone sand-rich debrites (Fig. 9D), associated with thick mudstone interbeds. *Lobe fringe deposits* (FA4.1.3) consist of low-density turbidites and a few stand-alone sand-rich debrites. This suggests deposition by rapidly decelerated mud-rich transitional flows (Baas *et al.*, 2009) and a few low to intermediate yield strength sand-rich debris-flows (Talling *et al.*, 2012), with collapsing suspension clouds forming mud caps in a topographically confined setting that promoted the widespread remobilization of these deposits into clastic injectites after burial (Fig. 9E).

Lobe complexes architecture and stacking patterns (SU4.1)

The SU4.1 lobe complexes (each *ca* 15 to 20 m thick) are exposed mainly in the Eastern Catán–Lil Basin, whereas in the Chachil Basin the equivalent strata (10 to 40 m thick) are mudstone-dominated (FA4.4) (Fig. 4). In the Eastern Catán–Lil Basin, SU4.1 is present in two small mud-draped topographic lows (*ca* 4 km wide) in the Martinez–El Cóndor (up to 65 m thick) and Tutavel–Espinazo Del Zorro sub-basins (up to 95 m thick). SU4.1 thins laterally *ca* 1 km towards the El Cóndor fault-block high and towards the slope flanking the northern Tutavel fault border where it reaches a minimum thickness (<20 m; see Fig. 4). The lobe complexes show variable bed thickness trends overprinted by widespread remobilization as clastic injectites. However, both sub-basin-fills show an overall thickening-upward trend in the lower part and thinning-upward and fining-

upward trend towards the top of succession, with dominant stacking of lobe complex fringes (FA4.1.3) (Fig. 9). This suggests an evolution with aggradation to forward-stepping of lobe complexes, with preferential deposition in the Tutavel–Espinazo Del Zorro sub-basin than in the Martinez–El Cóndor sub-basin, and final backstepping of the system (Fig. 4). The overall low sandstone content of SU4.1, with poor amalgamation, thick mud-rich interbeds, poorly defined thickness trends and stacking patterns, is interpreted to reflect the trapping of low volume fine-grained sandy and mud-rich flows relative to the size of the Eastern Catán-Lil Basin, with partial ponding in the two sub-basins of underfilled inherited rift topography (e.g. Romans *et al.*, 2011; Fonnesu *et al.*, 2018).

In the Chachil Basin, it is not possible to identify the equivalent SU4.1 due to the lack of marker beds. However, it might correspond to mudstone-prone deposits associated with local slumps, debrites and clastic injectites (cf. FA4.4) (Fig. 11A) present between the top of Unit 3 and the base of SU4.2. This suggests that only the most dilute parts of flows reached the Chachil Basin during coeval deposition of sandy flows (SU4.1 lobe complexes) in the updip Eastern Catán-Lil Basin.

Lobe complex stratal terminations (SU4.1)

Lobe complexes thin and fine gradually, or pinchout abruptly as clastic injectites close to inherited rift topography (Figs 4 and 5). Abundance of clastic injectites and diverse palaeocurrent measurements close to basin margins indicate deposition in a confined setting (e.g. Cobain *et al.*, 2017; Hansen *et al.*, 2019). This, together with the variable distribution of SU4.1 lobe complexes in both sub-basins, reflects lobe compartmentalization across a complex intrabasinal topography (Fig. 4). The lack of comparable sandy strata in the Chachil Basin (Fig. 11A) is interpreted to reflect the influence of topographic relief that induced partial ponding of SU4.1 lobe complexes in the Eastern Catán-Lil Basin.

Subunit 4.2

Lobe characteristics (SU4.2)

Subunit SU4.2 (30 to 124 m thick) forms a high sandstone content succession, dominated by coarser-grained and matrix-poor sandstone beds compared to SU4.1, with well-defined facies segregation by lobe sub-environments and thickness trends in both basins (Figs 4 and 10). SU4.2 matrix-poor lobes (1.2 to 11.7 m thick; Fig. 10) exhibit well-developed tractional bedforms, basal scours, clast-rich lags and various clast types (blueish siltstone, grey mudstone, epiclastic volcanics, bioclasts, carbonaceous fragments) (Table 1). The character of SU4.2 lobes indicates deposition by higher energy and larger volume high-density turbulent and subordinate transitional flows compared to SU4.1 (Figs 8 and 10).

Lobe-axis deposits (FA4.2.1) (Fig. 13A and D) are dominated by high-density turbidites including clast-rich beds (HDT 2), or transitional flow deposits (TFD 1) (Fig. 8). A few HEBs can be clustered at the base of lobe complexes, with muddy (HEB 2) or sand-rich (HEB 5) debritic divisions (Fig. 8), which record rapid flow deceleration and erosional bulking in a proximal lobe setting (e.g. Pierce *et al.*, 2018). These HEBs might reflect initiation of a given lobe complex (e.g. Tinterri & Tagliaferri, 2015). *Lobe off-axis deposits* (FA4.2.2) include HEBs (HEB 5) and transitional flow deposits with matrix-poor and heterolithic sandy bedforms (TFDs 1 and 2), but a poorly developed banded division, suggesting deposition from slowly decelerating flows (e.g. Baas *et al.*, 2016; Stevenson *et al.*, 2020) (Fig. 8). These transitional flow deposits and HEBs thin in *lobe fringe deposits* (FA4.2.3), which are more dominated by low-density turbidites (Fig. 13G and F) and that include local slumps (Fig. 8).

Lobe complexes architecture and stacking patterns (SU4.2)

The SU4.2 lobe complexes (each *ca* 20 to 40 m thick) are exposed mainly in the Eastern Catán-Lil Basin (Figs 5, 12A and 12B), whereas only

Fig. 8. Summary of the characteristic bed types including High Density Turbidite bed types (HDTs 1 to 2), Transitional Flow Deposits bed types (TFDs 1 to 5) and Hybrid Event Bed types (HEBs 1 to 5); these show variable occurrence and distribution in lobe subenvironments. The different divisions which make up the beds are detailed and based on matrix quantification in this study (SU4.2 and SU4.3) and Martinez-Doñate *et al.* (2023) (SU4.3); it is possible to distinguish their relative matrix content in the clean (10 to 12% matrix), the matrix-poor (12 to 20% matrix), the heterolithic (20 to 25% matrix), the matrix-rich (25 to 40% matrix) and the debritic (>40% matrix) divisions. These bed types are typically encountered in the SU4.2 fan (HDT 1 to 2, TFD 1 to 2, HEB 2 to 5) and in the SU4.3 fan (HDT 1, TFD 3 to 4 to 5, HEB 1 to 3 to 4). See Table 2 for descriptions.

HDT 1 (0.4 to 1 m thick)

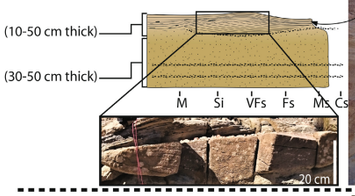

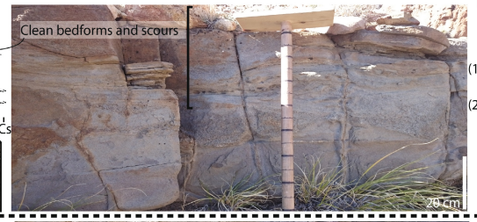

HDT 2 (0.2 to 0.6 m thick)

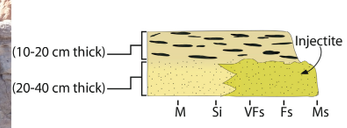

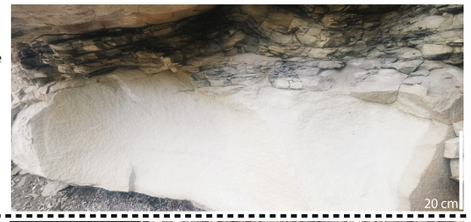

TFD 1 (0.2 to 0.5 m thick)

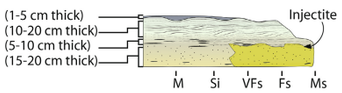

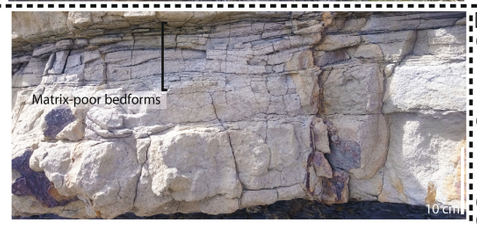

HEB type 1 (1 to 7 m thick)

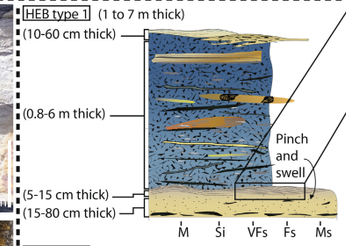

TFD 2 (0.5 to 1.2 m thick)

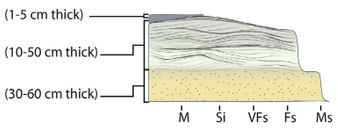

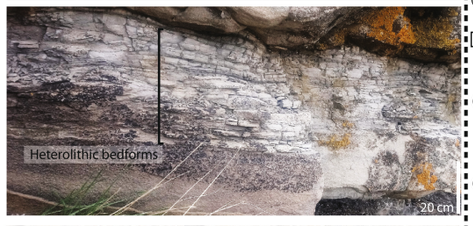

HEB type 2 (0.2 to 0.6 m thick)

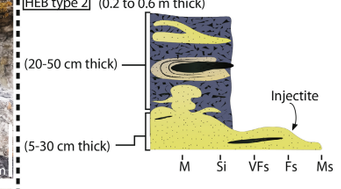

TFD 3 (0.4 to 0.8 m thick)

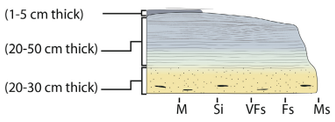

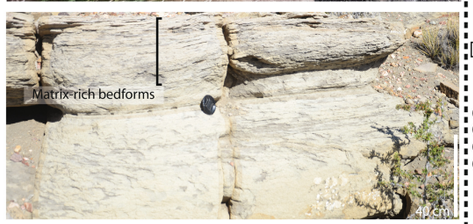

HEB type 3 (0.2 to 0.5 m thick)

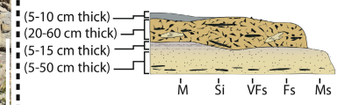

TFD 4 (0.2 to 0.5 m thick)

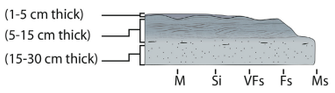

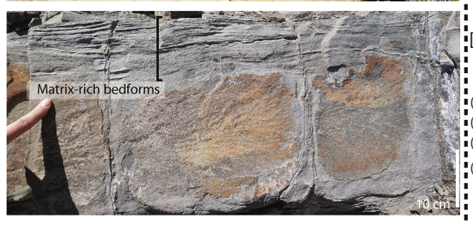

HEB type 4 (0.4 to 1 m thick)

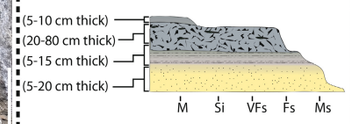

TFD 5 (0.2 to 0.5 m thick)

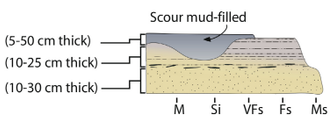

HEB type 5 (0.5 to 0.8 m thick)

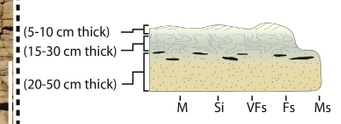

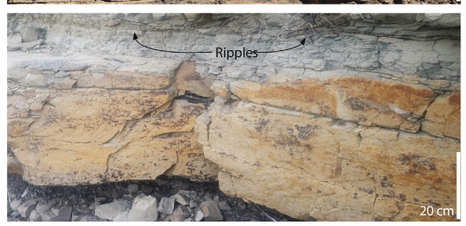

Basal sandy divisions

- Massive or with coarse tail normal grading locally with stepped laminae
- Crudely normally graded with concentration of outsized coarse grains at base
- Matrix-poor massive with mudstone clasts at base
- Clastic injectite
- Matrix-poor, massive with mudstone clasts at top
- Matrix-rich, massive with mudstone clasts at top

Sandy bedform divisions

- Clean sandy bedforms (large ripple- to dune-scale) locally associated with scour-fills including mudstone clasts at base of foresets
- Matrix-poor sandy bedforms with mudchips and thin carbonaceous-rich muddy foresets (low amplitude, shorter wavelength, hummock-like bedforms, and small biconvex ripples)
- Heterolithic sandy bedforms with carbonaceous-rich muddy foresets and drapes (high amplitude, long wavelength, swale- and hummock-like bedforms, large biconvex ripples)
- Matrix-rich sandy bedforms with muddy foresets (low amplitude, long wavelength, mud-rich bedwaves and large ripples)
- Matrix-rich sandy bedforms (low amplitude, long wavelength, hummock-like bedforms and large ripples)
- Matrix-rich sandy bedforms (low amplitude, long wavelength, swale- and hummock-like bedforms and small biconvex ripples)

Banded divisions

- Thin subparallel planar to low-angle sand-rich and mud-rich bands and bedwaves with mudchips and elongated mudstone clasts at base
- Thick subparallel planar to undulose sand-rich and mud-rich bands with mudchips throughout

Clast-rich division

- Mudstone clast-rich sandy division with matrix-poor sandstone bearing tightly packed crudely stratified oblate mudstone clasts

Debritic divisions

- Sand-rich debritic division with swirly matrix-rich sandstone bearing carbonaceous clasts
- Sand-rich debritic division with chaotic matrix-rich sandstone bearing mudstone and siltstone clasts throughout
- Muddy debritic division with patchy sand-rich mudstone matrix bearing few mudstone clasts throughout
- Muddy debritic division with starry night sand-poor mudstone matrix with mudstone and sandstone clasts and heterolithic rafts floating throughout
- Muddy debritic division with chaotic sand-poor mudstone matrix bearing mudstone and sandstone clasts (locally injected)

Upper divisions

- Structured planar to ripple cross-laminated and normally graded sandstone to siltstone
- Massive silty mudstone

Increasing matrix content

Fig. 9. Deposits of subunit SU4.1 in the Catán-Lil Basin, in the Espinazo Del Zorro sector (see section 7 in the Catán-Lil Basin on Fig. 5 for location). FA4.1.1: Lobe axis; FA4.1.2 Lobe off-axis; FA4.1.3: Lobe fringe. (A) and (B) Thick-bedded, poorly sorted, matrix-rich, medium to fine-grained sandstone with a tabular geometry (A), which consists in internally massive to crudely normally graded sandstone, locally with faint planar laminations, bearing a few mudstone clasts in the lower part of beds (B). (C) Medium to thick-bedded, sandstone bearing deformed mudstone pebbles distributed through the beds or near bed top, and with sharp base and deformed top pointing at their remobilization into clastic injectites. (D) Thin to medium-bedded mudstone-dominated heterolithics including silty mudstone, mudstone and fine-grained sandstone that can be normally graded with planar laminations or massive with small subrounded deformed mudstone pebbles. (E) Clastic injectites near lobe complex pinchout, with mounded bed tops (arrows), stepped margins and mudstone clasts at top (white frame).

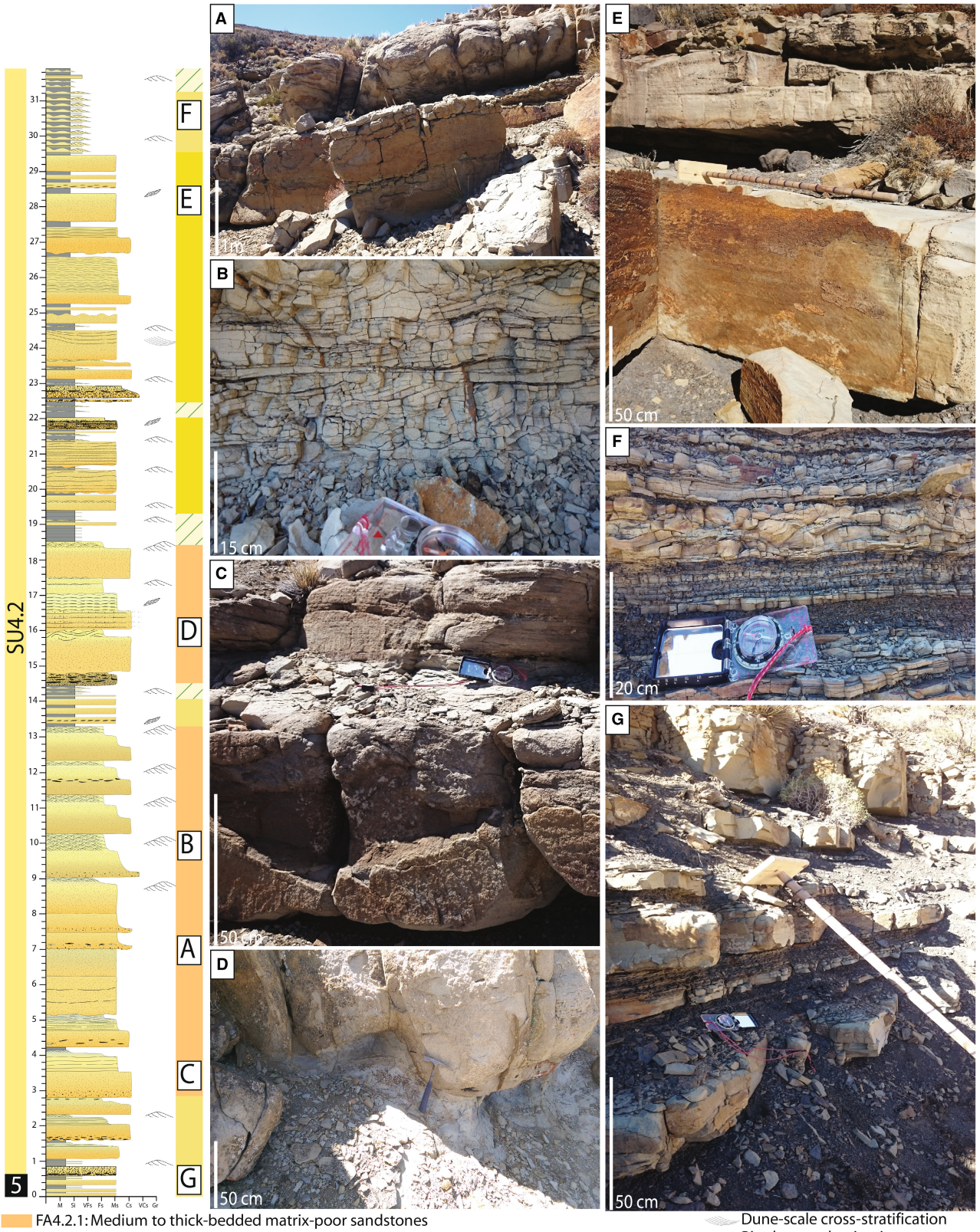

Fig. 10. Deposits of subunit SU4.2 in the Catán-Lil Basin (see section 5 in the Catán-Lil Basin on Fig. 5 for location). Note on pictures for scale, compass is 18 cm long, hammer is 40 cm long and Jacob's staff is 1.3 m long. FA4.2.1: Lobe axis; FA4.2.2 Lobe off-axis; FA4.2.3 (sand-rich): Lobe fringe. (A) Medium to thick-bedded, poorly sorted, matrix-poor, coarse to medium-grained sandstone with a tabular to mounded geometry, internally massive with outsized (very coarse) lithic grains, siltstone and/or mudstone pebbles and bioclasts near irregular erosive bed base and with sharp top. (B) Example of fine-grained structured upper part of beds with carbonaceous-rich parallel, planar, and climbing ripple laminations and thin muddy foresets. (C) Amalgamated medium to fine-grained sandstone with massive lower part and thick planar laminated upper part. (D) Amalgamated coarse to medium-grained sandstone with scoured base eroding into the silty-mud-rich top of underlying sandstone bed. (E) Massive or planar laminated sandstone bodies (clastic injectites–sills) (0.2 to 0.5 m thick, 10 to 100 m across). Note the mounded upper surface of middle sandstone bed and at top the abrupt pinchout of a thinner sandstone bed (clastic injectites). (F) Thin-bedded heterolithic packages with fine-grained sandstone, planar to ripple-cross laminated, with soft sediment deformation and sharp planar base and top, interbedded with massive siltstone and carbonaceous-rich mudstone. (G) Thin to medium-bedded sand-rich heterolithic packages with medium to fine-grained and massive to planar laminated sandstone.

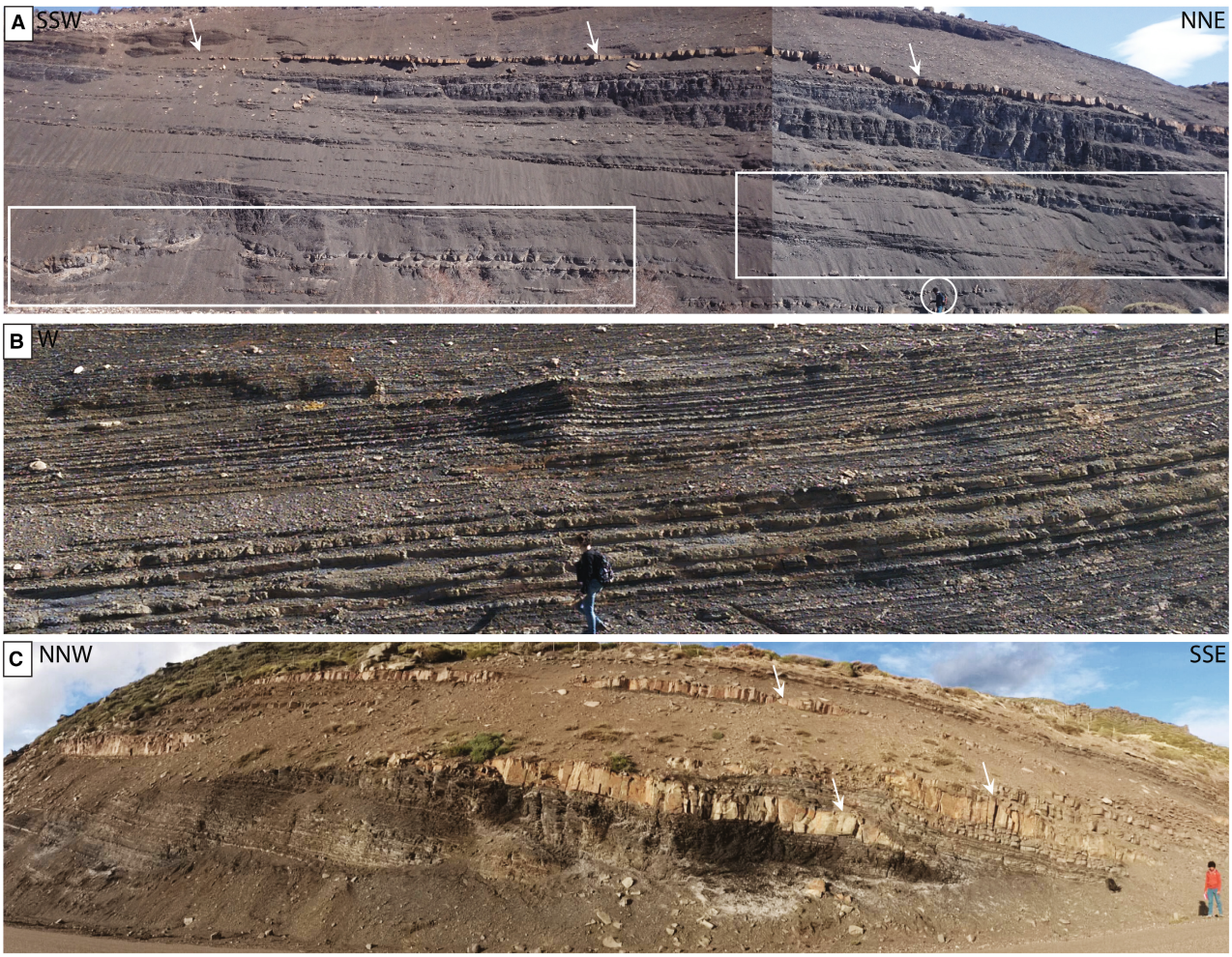

Fig. 11. Mudstone-prone successions in the Chachil Basin. (A) SU4.1 mudstone-prone succession with debrites, slumps and injectites (white arrows) (FA4.4) in the Chachil Basin (between sections 7 and 10 – see Fig. 5). White rectangles show slumped strata; person for scale, circled (*ca* 1.8 m tall). (B) SU4.2 mudstone-dominated heterolithic succession (FA4.2.2) in the Chachil Basin (section 5) with fringes and off-axis deposits of stacked lobe complexes including transitional flow deposits (TFDs) and hybrid event beds (HEBs). (C) SU4.2 mudstone-dominated heterolithic succession of pinching-out lobe fringes (FA4.2.3) in the Chachil Basin (section 2) with well-developed fine-grained clastic injectites (white arrows) close to the Southern Chachil horst border. See location on Fig. 5 of (A) at base of section 8, (B) at base of section 4, and (C) at base of section 2.

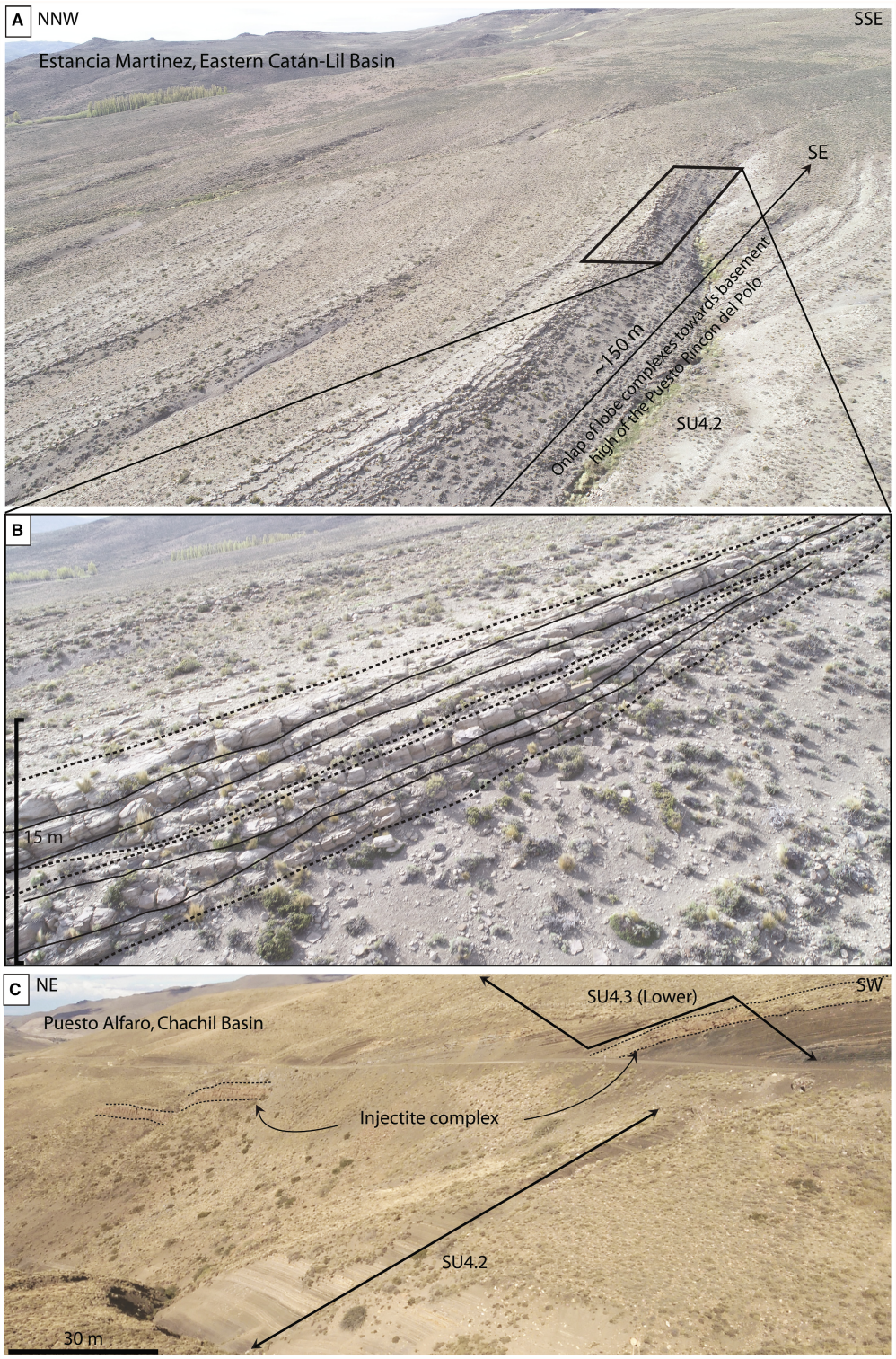

Fig. 12. Geometries of lobe complexes. (A) and (B) SU4.2 lobe complexes showing thinning and fining across a few kilometres (*ca* 2 km) from the Martinez sector towards the Puesto Ricón del Polo horst (section 4), along the south-eastern border of the Eastern Catán-Lil Basin. (C) SU4.2 and SU4.3 lobe complexes in the Chachil Basin, with injectite complex at base of SU4.3 (section 5). See location on Fig. 5 of (A) and (B) in middle part of section 4 in the Eastern Catán-Lil Basin, and (C) at base of section 5 in Chachil Basin.

lobe complex fringes (40 to 75 m thick) are present in the Chachil Basin (Figs 5 and 12C). In the Eastern Catán-Lil Basin, the laterally extensive mudstone interval (2.2 to 6.3 m thick) (Fig. 4) that separates SU4.1 and SU4.2 marks a regional decrease in sand supply, which could record abandonment of the feeder system through avulsion, or reduction in updip sediment supply. Based on lobe complexes margins, a 6 km by 10 km wide sand-rich depocentre within this basin is estimated for SU4.2, with a maximum stratigraphic thickness of 124 m (El Cóndor-Martinez sector) and lateral or oblique downdip thinning to 30 m towards basin margins (Tutavel-Pesceira and Puesto Rincón del Polo horst sectors) (Figs 4 and 5).

The five lobe complexes defined in SU4.2 can be traced across the basin (Fig. 4) and are laterally more extensive (5.0 to 8.5 km) than the SU4.1 lobe complexes, indicating less intrabasinal relief. Several lobe complexes display asymmetrical coarsening-upward and thickening-upward then fining-upward and thinning-upward trends, reflecting a range of lobe stacking patterns (see Prélat & Hodgson, 2013). The vertical succession of the stacked SU4.2 lobe complexes is interpreted to record: (i) initial forward-stepping (the first two lobe complexes); (ii) lateral and/or longitudinal migration, with backstepping of the locus of lobe complex axes from the El Cóndor section to the Martinez section (the middle two lobe complexes); and (iii) upslope backstepping of the system (topmost lobe complex) (Fig. 4). The retreat of the youngest lobe complex could reflect accommodation increase along the south-eastern margin of this basin (Fig. 4). The lack of abrupt vertical facies changes (i.e. multiple stacking of lobe-axis and fringe deposits within a lobe complex) suggests that progradational to aggradational lobe stacking prevailed over compensational stacking, suggesting deposition with moderate confinement at the basin margins (e.g. Marini *et al.*, 2015) (Fig. 4).

In the Chachil Basin, SU4.2 corresponds to a thick (up to 75 m) mudstone-dominated heterolithic succession representing stacked lobe complex fringes, characterized by only a few, thin, sandy packages (*ca* 2 to 5 m thick) representing TFD-rich and HEB-rich lobe off-axis deposits (FA4.2.2) (Figs 11B and 12C). The presence of siltstone clasts, and the grain-size range, good sorting and matrix-poor texture supports a correlation with SU4.2 lobe complexes in the Eastern Catán-Lil Basin, but a precise correlation was not possible due to a lack of good exposure (Fig. 4). The SU4.2 lobe complex fringe-dominated succession thickens (40 to 75 m thick) from the south-western margin to the axis of the Chachil Basin (Fig. 4), where it is associated with local slumps, debrites and minor clastic injectites (Fig. 11A and C). Local thickness changes suggest that deposition of SU4.2 healed the remaining inherited rift-related topography in this basin. The thick accumulation of SU4.2 lobe complex fringes in the Chachil Basin, and palaeocurrent data, are indicative of flow reflection and deflection (Fig. 5) on both sides of the Southern Chachil horst border, suggesting that it acted as a low-relief topographic high. This relief only allowed the overspill of the most dilute part of flows in the Chachil Basin during predominant sand deposition in the updip basin, and progressive diversion of sandy fairways could occur around this relief.

Lobe complex stratal terminations (SU4.2)

In the Eastern Catán-Lil basin, basal lobe complexes thin and fine northward, in an oblique downdip direction across *ca* 4 km, suggesting confinement by a north-west basin margin slope (Fig. 4). This interpretation is supported by palaeocurrent measurements of current ripples at high angles to the main palaeocurrent direction, indicating flow reflection and deflection (Fig. 5). Thinning and fining of lobe complexes across a few kilometres (*ca* 2 km) from the basin centre to the south-western basin margin (Fig. 12A and B) also supports moderate confinement of the sandy depocentre. The SU4.2 lobe complexes fringes (FA4.2.3) are dominated by TFDs towards the north-western basin margin, suggesting development of frontal lobe fringes (e.g. Spychala *et al.*, 2017). In contrast, the dominant planar and ripple laminated low-density turbidites towards the confining south-eastern basin margin (Fig. 12A) suggest the development of lateral lobe fringes (e.g. Spychala *et al.*, 2017) and/or lobe fringes in a more proximal setting.

In the Chachil Basin, the SU4.2 lobe-fringe-dominated heterolithic succession (FA4.2.2, FA4.2.3) shows tapered thinning and fining, or abrupt pinchout associated with clastic injectites, towards the basin margins (Fig. 11C) also suggesting confinement (e.g. Cobain *et al.*, 2017; Hansen *et al.*, 2019).

Subunit 4.3

Lobe characteristics (SU4.3)

Subunit SU4.3 (120 to 190 m thick) forms a moderate sandstone content succession, dominated by coarse-grained, clast-rich and matrix-

rich sandstone beds (Figs 4 and 13). The SU4.3 lobes (1.5 to 5.0 m thick) include sand-filled or mud-filled scours, basal lags, coarse-grained sandy bedforms and less varied clast types than SU4.2 (dark grey mudstone, few siltstones, bioclasts and ammonites, armoured mudstone clasts) (Figs 13 and 14). The character of SU4.3 lobes indicates deposition by coarser-grained and higher-energy turbidity currents associated with more erosion and sediment bypass, and more transitional and hybrid flows than for SU4.2, with the sporadic occurrence of muddy HEBs (HEB 1) (Figs 8 and 13).

Lobe-axis deposits (FA4.3.1) are dominated by high-density turbidites (HDT 1) and transitional flow deposits (TFDs 3 to 5) that are commonly scoured at their top (Fig. 13F and G), and include a few HEBs with thick, debritic divisions (HEB 1) (Fig. 8) occurring between amalgamated sandy packages (Fig. 14B and C). *Lobe off-axis deposits* (FA4.3.2) include transitional flow deposits (TFDs 4 and 5) and HEBs (HEBs 1, 3 and 4). The matrix-rich sandy bedforms (TFDs 3 and 4) and well-developed banded divisions (TFD 5) here suggesting deposition by more clay-rich, more rapidly decelerating flows than in SU4.2 (TFD 1 and 2). These observations suggest a more confined setting in the Chachil Basin (e.g. Stevenson *et al.*, 2020). Hybrid event beds with thin debritic divisions (HEBs 3 and 4) record extensive and rapid flow bulking from lobe-axis to off-axis (e.g. Haughton *et al.*, 2009; Fonnesu *et al.*, 2015; Pierce *et al.*, 2018), which contrasts with SU4.2 (FA4.2.2) (Fig. 8). Additionally, HEBs with thick debritic divisions and extra-basinal clasts (HEB 1) are present, reflecting voluminous debris-flows derived from a proximal slope setting. *Lobe fringe deposits* (FA4.3.3) are dominated by thinner and muddier transitional flow deposits (TFD 5) and HEBs (HEBs 3 and 4). HEBs with thick debritic divisions (HEB 1) (Fig. 13B and D) and low-density turbidites including biconvex ripples (cf. Privat *et al.*, 2021) (Fig. 13E) are also present.

Lobe complexes architecture and stacking patterns (SU4.3)

The SU4.3 lobe complexes (each *ca* 15 to 30 m thick) are exposed in the two studied basins, thus are laterally more extensive than equivalent units in SU4.2, suggesting deposition in a broader depocentre during this stage (Figs 4 and 5). SU4.3 comprises a lower and upper lobe complex separated by a thick (30 to 40 m) mudstone interval (Fig. 4).

In the Eastern Catán-Lil Basin, SU4.3 is relatively thick (up to 120 m thick), with lobe complexes developed towards the north-east across a smoother intrabasinal topography partially healed by deposition of SU4.2. Despite the discontinuous exposure, a well-exposed lobe complex (*ca* 15 to 20 m thick) in the basin centre (Fig. 14A) shows coarsening-upward and thickening-upward trends passing from lobe fringes (FA4.3.3) to lobe off-axis and axial deposits (FA4.3.1 and FA4.3.2), suggesting progradation. In contrast, the north-western basin margin is dominated by off-axis and lobe fringe deposits (FA4.3.2 and FA4.3.3), with fining-upward trends that could record aggradational

Fig. 13. Deposits of subunit SU4.3 in the Chachil Basin (see section 5 in the Chachil Basin on Fig. 5 for location). Jacob's staff is 1.3 m long, where shown. FA4.3.1: Lobe axis; FA4.3.2 Lobe off-axis; FA4.3.3: Lobe fringe. (A) Massive fine-grained sandstone bodies (clastic injectites-sills) (0.2 to 3.0 m thick, 5 km across) cross-cutting (<15°) thin to very thin-bedded mudstone-dominated heterolithics. Injectites bear angular rafts (10 to 50 cm thick, >1 m across) with long axis parallel to bedding of host strata and have sharp planar or stepped margins locally mantled with mudstone clasts (2 to 5 cm long). (B) Interbedded poorly sorted, medium to fine-grained sandstone, siltstone and silty mudstone beds (5 to 20 cm thick) with pin-striped sandy to silty laminated mudstone and sandy or mud-filled scours (10 to 15 cm deep, *ca* 1 m long). (C) Amalgamated poorly sorted, matrix-rich (note the blueish colour), medium-grained sandstone with banded top divisions. (D) Thick-bedded or medium to thin-bedded, sandstone-dominated heterolithics including medium to fine-grained, matrix-rich sandstone often banded, and clast-rich muddy HEB type 1 (0.6 to 7.0 m thick) with thick debritic division overlying a basal sandstone that shows pinch and swell and pinchout. (E) Medium to fine-grained sandstone with biconvex ripples with sigmoidal foresets (<5°) (2 to 6 cm thick, 10 to 15 cm wavelength) showing opposite or oblique palaeoflow directions, in thin to very thin-bedded mudstone-dominated heterolithics. (F) Amalgamated poorly sorted, matrix-poor, coarse to medium-grained sandstone with basal coarse-tail normal or inverse grading, bearing mudstone and siltstone clasts in their lower part and with planar to low-angle cross stratified top. (G) Coarse to medium-grained sandy scours at top of amalgamated sandstone lobe, with at base (highlighted with white line) thinly cross-stratified bedsets (5 to 10 cm thick foresets) bearing mudstone clasts (0.5 to 2.0 cm long) overlain by scour-fills with well-sorted swale-like bedforms (25 to 50 cm thick, 0.2 to 0.5 m wavelength) with high-angle (15° to 30°) cross-stratification and trough cross-stratification.

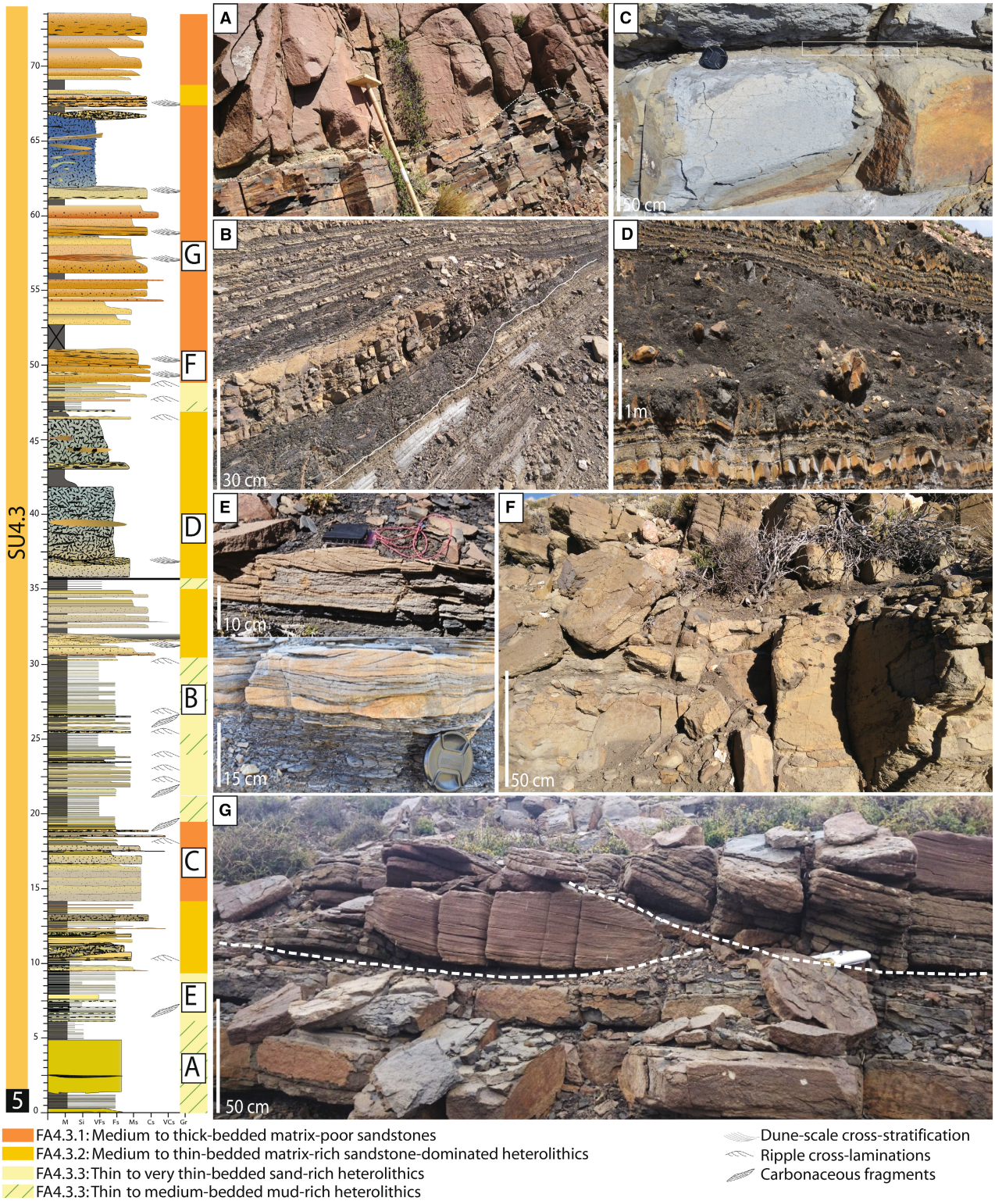

and compensational lobe stacking. The intervening lens-shaped clast-rich sandy packages (FA4.3.4) might represent isolated sand-filled scours or gullies (Figs 4 and 14D), which have been extensively remobilized as clastic injectites.

In the Chachil Basin, SU4.3 forms a better exposed and thicker succession (160 to 190 m thick), enabling detailed lateral correlations. It is possible to constrain a minimum 5 km width and >6 to 8 km length for the system based on

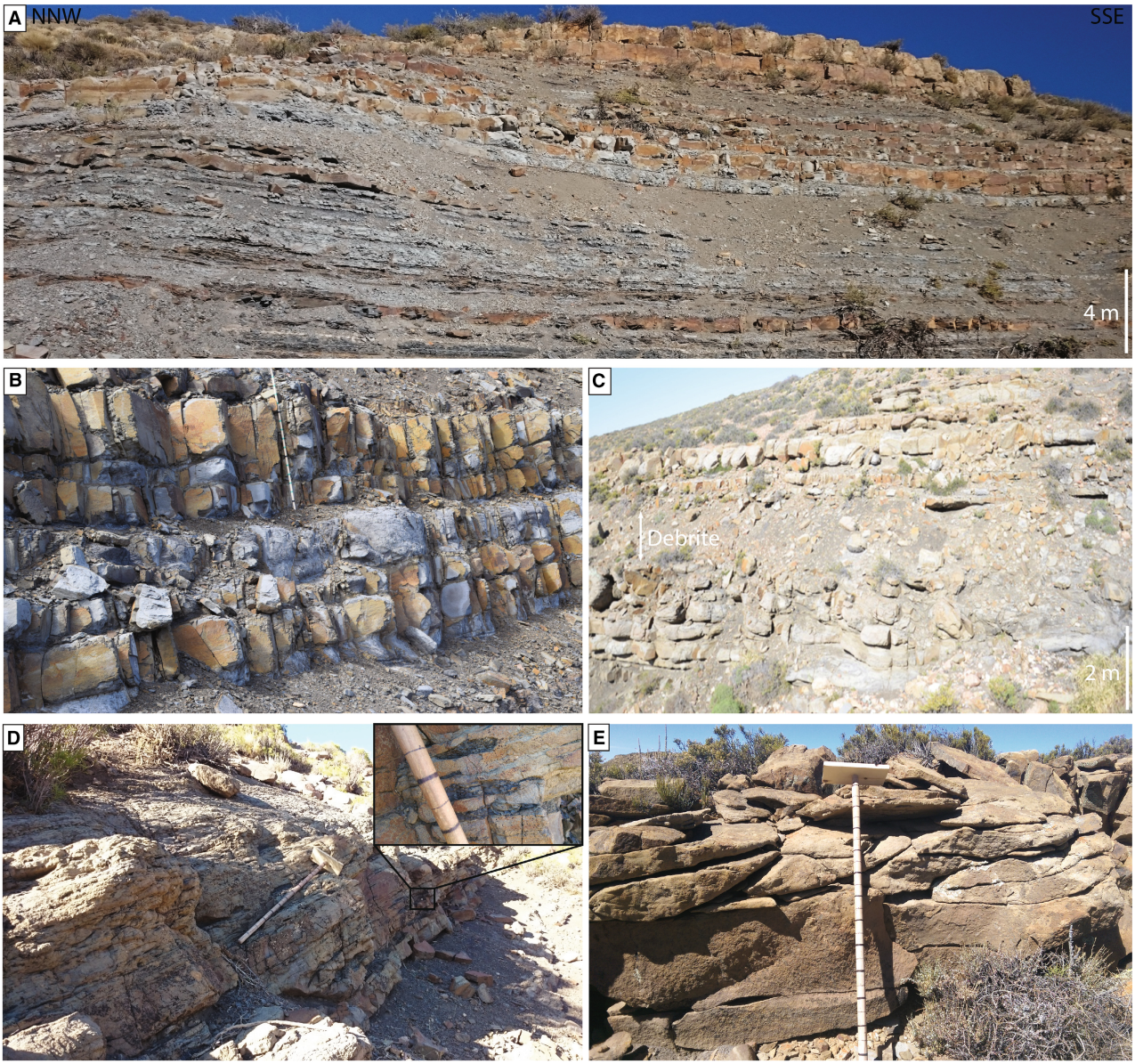

Fig. 14. Geometries and deposits of lobe complexes. Jacob's staff is 1.3 m long, where shown. (A) SU4.3 in the Estancia Martinez (section 4), Eastern Catán-Lil Basin, showing the lower SU4.3 lobe complexes (FA4.3.1-FA4.3.2, FA4.3.3) including matrix-rich lobes (blueish colour) and cleaner matrix-poor lobes (yellowish colour) similar to the trend seen in the Chachil Basin (cf. Privat *et al.*, 2021). (B) SU4.3 in the Puesto Alfaro (section 5), Chachil Basin showing the lower SU4.3 lobe complexes with amalgamated matrix-rich lobes (FA4.3.1). (C) SU4.3 in Picún Leufú (section 7), Chachil Basin, showing amalgamated lobes with intervening HEB type 1 with thick debritic division (FA4.3.1). (D) SU4.3 in the Pesceira (section 10), Eastern Catán-Lil Basin, showing the upper SU4.3 sandbodies here with coarse to medium-grained sandy scour-fill full of rip-up mudstone clasts (see inset) which are locally remobilized into clastic injectites (FA4.3.4). (E) SU4.3 in Casa Piedra (section 15), Chachil Basin, showing the upper SU4.3 sandbodies that consist of sandy scour or gully-fills and lobes, bearing mudstone and blueish siltstone clasts and bioclastic material. Shows a cross-stratified top (FA4.3.4).

oblique frontal pinchout of lobe complexes across 2 km from the basin centre to the northern basin margin (Picún Leufú to Casa Piedra sector) (Fig. 4). SU4.3 includes a lower sandy succession (70 to 120 m thick) of lobe complexes and an upper heterolithic succession (*ca* 45 m thick) including scour or gulley-fills and lobes, which are separated by a thick mudstone-prone interval (*ca* 35 m thick) (Fig. 4). The lower succession records a coarsening-upward and thickening-upward trend

with a stratigraphic evolution from dominantly stacked lobe fringe and off-axis deposits (FA4.3.3 and FA4.3.2), vertically grading to lobe-axis deposits (FA4.3.1) (Fig. 4). This suggests a general forward-stepping of lobe complexes, overprinted by lobe-scale compensational stacking, which reflects confinement by intrabasinal topography (Privat *et al.*, 2021; Martinez-Doñate *et al.*, 2023). In turn, the upper succession mainly consists of sand-filled and heterolithic-filled scours or gullies enriched in bioclastic material and encased in mudstone-prone strata (FA4.3.4) (Fig. 14D and E), which record deposition in a more proximal lower slope environment.

Lobe complex stratal terminations (SU4.3)

Subunit SU4.3 in the Eastern Catán-Lil Basin records lobe complex stratal terminations with bed thinning and a decrease of sandstone content over 4 km towards the northern basin margin (Fig. 4). Here, the dominant laminated low-density turbidites, TFDs and sand-rich debrites (FA4.2.3), support frontal lobe fringes (e.g. Spychala *et al.*, 2017). Palaeocurrent data indicate flow reflection or deflection (Fig. 5), suggesting that a remnant relief or a counterslope at the northern margin of the Eastern Catán-Lil Basin could have enhanced lateral lobe switching and deposition of the basal coarser-grained load of flows that otherwise bypass into the Chachil Basin. These observations indicate deposition of SU4.3 in a weakly confined setting in the Eastern Catán-Lil Basin. In the Chachil Basin, SU4.3 lobe complexes show more abrupt bed thinning and decrease of sandstone content across 2 to 3 km towards the northern basin margin (Fig. 4). Here, the stacked HEB-rich frontal lobe fringes record bed thinning (but not necessarily fining) and pinchout further downdip from the pinchout of thick mud-rich HEBs (HEB 1). Together with numerous clastic injectites and indicators of flow deflection and reflection (Figs 5 and 13E), the described stratal termination patterns suggest deposition with partial confinement by inherited rift topography (Privat *et al.*, 2021; Martinez-Doñate *et al.*, 2023).

DISCUSSION

Regional depositional setting and controls on early post-rift intraslope fans

The early post-rift intraslope fans (SU4.1, SU4.2 and SU4.3) of the Early Jurassic Los Molles Formation developed across low-relief and low-gradient basin margins (i.e. ramp-type system; Heller & Dickinson, 1985) bounding a relatively shallow offshore marine embayment and starved basin-floor (Figs 15 and 16). Seabed topography was controlled by the balance between early post-rift sediment supply and thermal subsidence of the backarc basin (100 to 200 to 400 m water depth; Gómez Omil *et al.*, 2002; Gómez-Pérez, 2003; Pángaro *et al.*, 2009; Brinkworth *et al.*, 2018). The stratigraphic evolution of the three early post-rift intraslope fans records a consistent increase of sandstone content, grain-size and clast-size (from SU4.1 to SU4.3) (Figs 9, 10 and 13) and a large-scale coarsening-upward trend associated with more common erosion and bypass features, debrites and HEBs over time (Fig. 15).

The recorded stratigraphic evolution contrasts with that of structural shelves and out-of-grade slopes in rift basins, which tend to promote direct coarse sediment bypass to base-of-slope and basin-floor settings, producing a progressive stratigraphic fining-up trend (e.g. Leeder *et al.*, 2002; Strachan *et al.*, 2013; Henstra *et al.*, 2016). In contrast, the observed stratigraphic evolution of intraslope fans in the Los Molles Formation could reflect an overprint due to the juxtaposition of axial and transverse deep-water systems developed from different sources (Fig. 16). In this context, inferred axial systems would be supplied by a south-west volcanic arc-derived source, whereas the transverse systems would be fed from the south-east cratonic source (Fig. 16). This scenario is like other documented early post-rift systems that developed from multiple active sediment sources (e.g. Deller, 2005; Lien, 2005; Fugelli & Olsen, 2007; Zachariah *et al.*, 2009; Henstra *et al.*, 2016). More specifically, the juxtaposition of axial and transverse systems involving volcanogenic and cratonic sources having different textural and compositional characteristics, has implications for the variability of reservoir quality, which commonly occur in intra-arc or back-arc basins (e.g. Marsaglia *et al.*, 1995; Sylvester & Lowe, 2004; Takano *et al.*, 2005; Masalimova *et al.*, 2016; Shumaker *et al.*, 2018) or in retroarc foreland settings (Malkowski *et al.*, 2017). It is notable that in the studied basins, despite the coeval existence of these two sediment sources, the regional palaeogeographical reconstructions show that, during the early post-rift (Early–Late Toarcian), the transverse cratonic-sourced fan deltas and intraslope fans were mainly trapped across slope

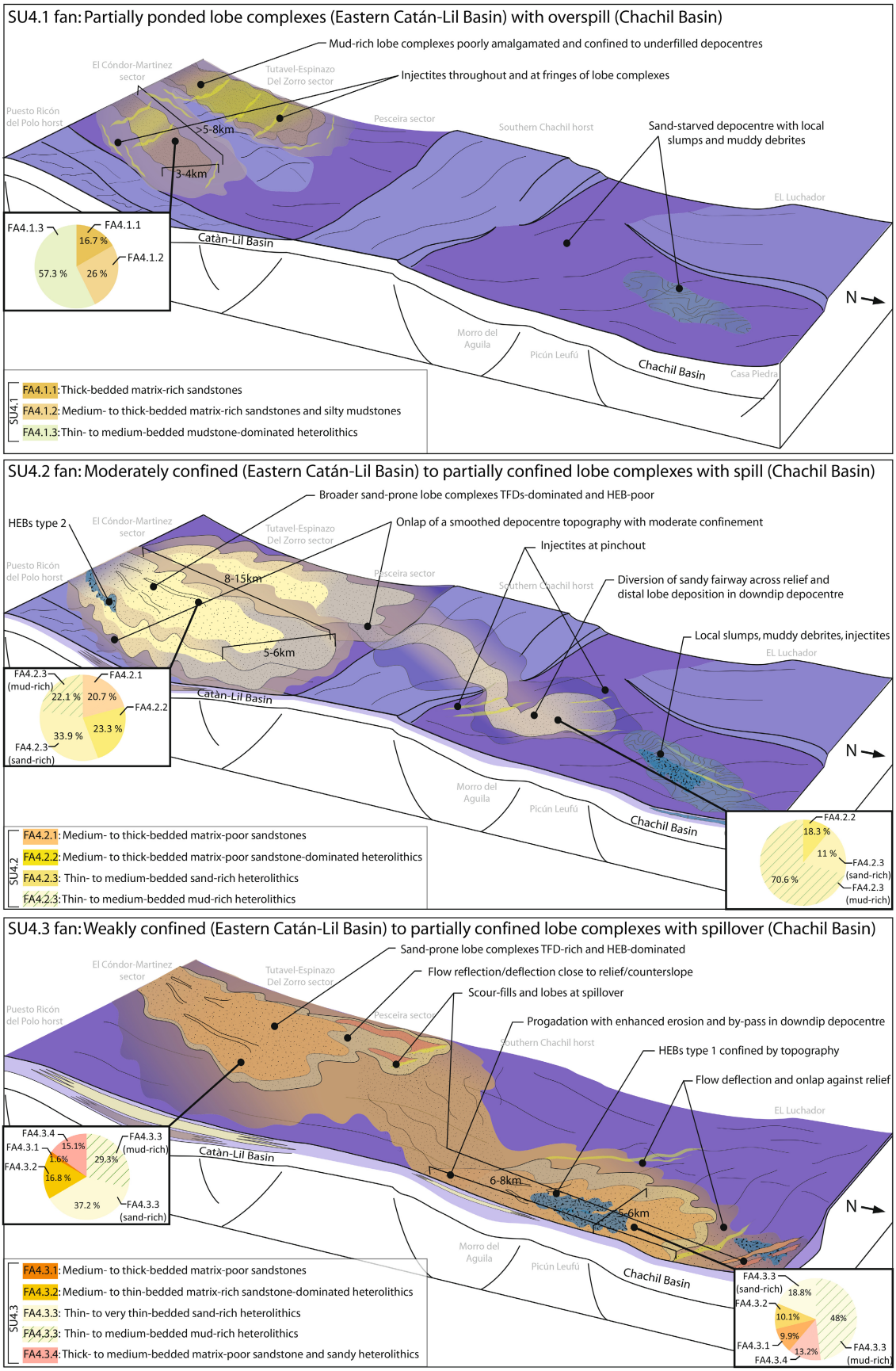

Fig. 15. Block diagrams showing the evolution of the three sandy subunits (fans) with progressive stepwise infill of inherited rift topography and development of lobes with different degree of confinement during linkage of intraslope depocentres. SU4.1 is partially ponded, SU4.2 is moderately confined by basin margins, SU4.3 is weakly confined in updip basin and partially confined in downdip basin by intrabasinal topography. Intraslope fans indicate an evolution as a fill-and-spill system, with initial partial ponding through overspill, to spillover with erosion and bypass across a transverse topographic high separating both depocentres. Note the occurrence of clastic injectites and contrasting stratigraphic HEB and TFD pattern at fan-scale. Total proportions of facies associations are shown in pie charts in each sandy subunit (cf. Table 1 and Figs 9 and 10–13) and aims to represent the relative sandstone content for each intraslope fan in each depocentre. HEB: Hybrid event bed; TFD: Transitional flow deposit; LDT: Low-density turbidite.

topography along the southern Neuquén Basin margin eastward of the study area (Gómez Omil *et al.*, 2002; Pángaro *et al.*, 2009; Brinkworth *et al.*, 2018) (Fig. 16). This is also supported by provenance analysis that does not evidence any distinct cratonic provenance signature, suggesting a uniform volcanogenic-dominated source area, consistent with axial progradation of early post-rift intraslope fans towards the NNE/north-east, subparallel to the north-east/south-west trending and north-west-dipping cratonic southern Neuquén Basin margin (Fig. 16).

The coarsening-upward trend and increase in grain-size and clast-size recorded in the early post-rift intraslope fans succession (SU4.1 to SU4.3) can be explained by several factors acting independently or in combination. First, this pattern could reflect a change of sediment grain-size range available and/or an increase of volcanogenic sediment production at source (i.e. Shumaker *et al.*, 2018). This would have helped to drive deltaic progradation, inducing a direct response of slope systems with progradation, as observed in narrow, ramp-type systems (e.g. Heller & Dickinson, 1985; Martinsen *et al.*, 2003; Eschard *et al.*, 2004; Ravnås *et al.*, 2014). Additionally, the enhanced bypass of the coarse grain-size fraction and occurrence of mass-wasting products from the SU4.1 to SU4.3 fans records an increase in flow energy and capacity that could reflect a progressive slope steepening. Slope steepening could be driven by the growth and uplift of the early Andean magmatic arc through time (Marsaglia *et al.*, 1995; Dorobek, 2007) and/or margin tilting with onset of post-rift thermal subsidence (Rabineau *et al.*, 2014; Balázs *et al.*, 2017; Roberts *et al.*, 2019). This would have enhanced erosion and retrogressive slope failures controlling progressive channel development and/or canyon incision, as seen along volcanic island arc slopes in other subduction-related active margins (e.g. Klaus & Taylor, 1991; Laursen & Normark, 2003; Noda *et al.*, 2008; Leclerc *et al.*, 2016; Clare *et al.*, 2018; Hsieh *et al.*, 2020). Finally, given the influence of inherited rift topography in the study area (Privat *et al.*, 2021), the filling of proximal slope topography and accommodation could also have resulted in enhanced bypass of the coarse grain-size fraction downslope (e.g. Prather, 2003; Covault & Romans, 2009).

Development of intraslope fans across inherited rift-related relief

Large-scale stratigraphic architecture of early post-rift intraslope fans records a high degree of sand compartmentalization and stepwise filling of inherited, rift-related relief across the Eastern Catán-Lil and Chachil basins. The Southern Chachil horst border acted as a topographic barrier (i.e. sill), suggesting a fill-and-spill linkage between the updip (Eastern Catán-Lil) and the downdip (Chachil) basins (Fig. 15). The sandy fans developed with variable confinement in the updip and downdip basins, depending on the initial configuration of inherited rift topography and progressive healing of accommodation. The SU4.1 fan records partial ponding in the updip basin and coeval sand starvation in the downdip basin. The SU4.2 and SU4.3 fans developed respectively with moderate and weak confinement in the updip basin, reflecting the progressive healing of the inherited rift topography. In contrast, the SU4.2 to SU4.3 fans developed with higher local confinement in the downdip basin, as the limited sand supply promoted a longer preservation of inherited rift topography.

Partial ponding and overspilling

The SU4.1 fan is a low sandstone content succession, which records trapping of sandy and muddy flows in accommodation inherited from rift topography of the updip basin. This characteristic suggests initial sand supply by low volume flows relative to the basin size, with

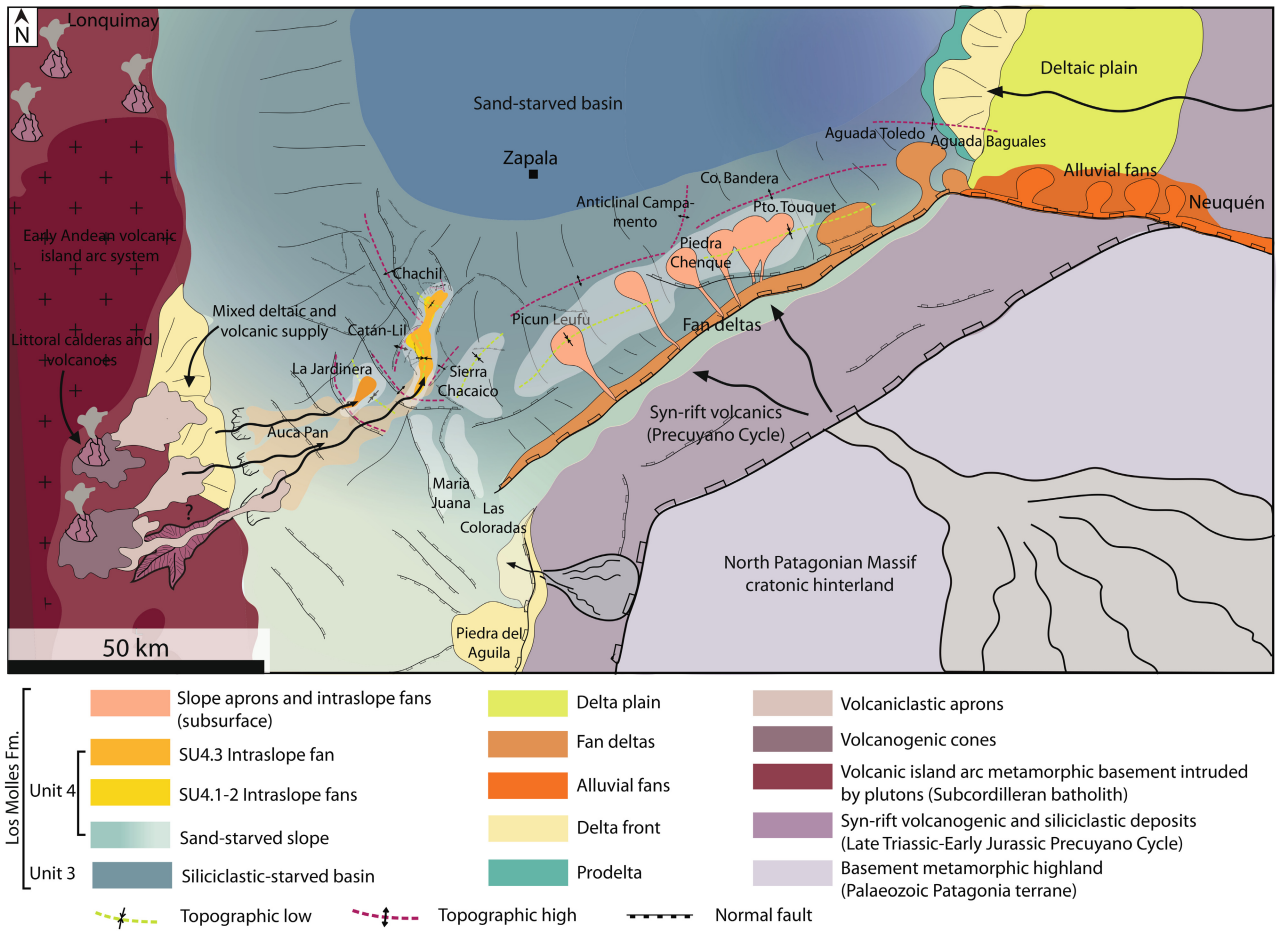

Fig. 16. Early–Late Toarcian palaeogeographical map of the Southern Neuquén Basin showing the configuration of sediment sources with axial and transverse systems developed respectively across volcanic arc and cratonic margins bounding the deep-marine backarc basin (100 m to 200 to 400 m depth; Gómez Omil *et al.*, 2002; Gómez-Pérez, 2003). Early post-rift fans prograded transversely to rift structures towards the NNE/north-east, subparallel to the north-east/south-west striking and north-west dipping cratonic Southern Neuquén Basin margin (see also rift structures in Gómez Omil *et al.*, 2002; Franzese *et al.*, 2006; García Morabito, 2010; Muravchik *et al.*, 2014; D'Elia *et al.*, 2015; Brinkworth *et al.*, 2018). Mud-draped inherited rift fault topography, expressed at the seabed with anticlinal and monoclinal folds associated with onlap and confinement (cf. Privat *et al.*, 2021), controlled the distribution of sandy depocentres. Note the onset of sand supply with the first fans developed in the Late Toarcian in La Jardinera depocentre (Giacomone *et al.*, 2020; Arienti Gonçalves *et al.*, 2022; Steel *et al.*, 2023) (Fig. 2). The studied intraslope fans (Unit 4) were fed with sand supply from mixed deltaic and epiclastic volcanogenic line-sourced coastal systems developed along the early Andean volcanic island arc (cf. De la Cruz & Suárez, 1997). Coeval early post-rift fans (in subsurface) developed in the south-eastern sector with sediment supply from nearby cratonic hinterland and sand trapping across slope topography of the Southern Neuquén Basin margin (Gómez Omil *et al.*, 2002; Brinkworth *et al.*, 2018). Subsequently, transpression started and fault-block uplift enhanced sediment supply from cratonic sources located tens of kilometres further to the east. This promoted the rapid progradation of deltaic-fed transverse systems and the development of a 'standard' passive-margin system, with a well-defined shelf-break by Middle Jurassic (Aalenian–Bathonian). This passive margin system included younger shelf-edge deltas, slope channels and connected basin-floor fans not shown on this map, which are documented in subsurface (Gómez Omil *et al.*, 2002; Brinkworth *et al.*, 2018) and at outcrop (Gulisano & Guttiérrez Pleimling, 1995; Paim *et al.*, 2008; Arienti Gonçalves *et al.*, 2022; Steel *et al.*, 2023).

possible overspill to the downdip basin of the most dilute part of larger volume flows, as suggested for other similar examples (Shultz & Hubbard, 2005; Marini *et al.*, 2016). In SU4.1, the widespread remobilization of lobes into clastic injectites also suggests deposition in a topographically confined setting (e.g. Cobain *et al.*, 2017; Hansen *et al.*, 2019) (Fig. 17A and B).

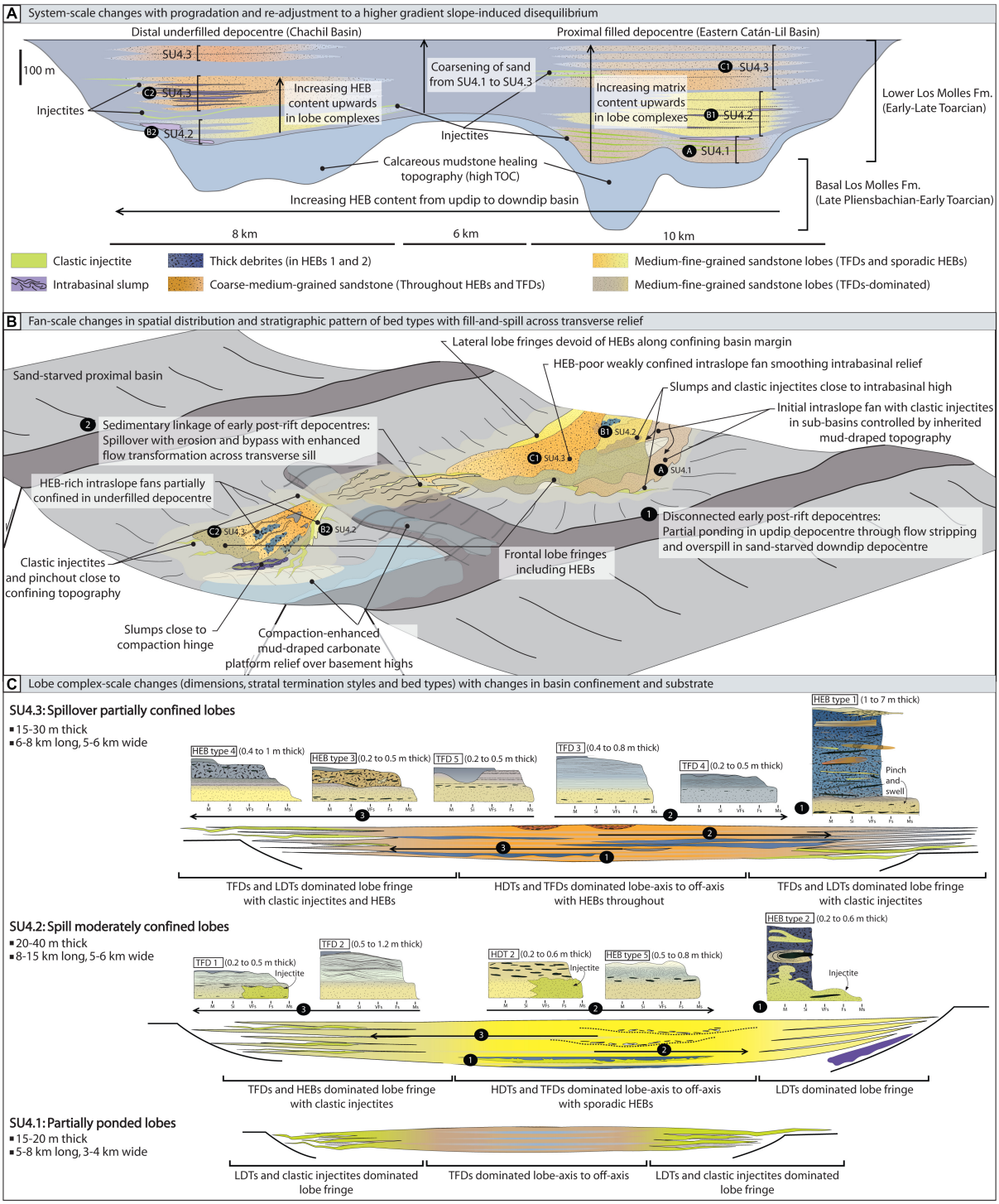

Fig. 17. Synthetic evolution model for the documented early post-rift fill-and-spill system, in cross-section (A) and spatially (B), showing progressive linkage of disconnected depocentres, with initial partial ponding through overspill, to spillover and bypass across transverse topography, promoting erosion and flow transformation, with preferential HEB development in the downdip basin. The successive intraslope fans developed with different degree of confinement by inherited rift topography that resulted in various lobe complexes dimensions, stratal termination styles and bed types distribution as shown in (C) schematic cross-sections for SU4.1, SU4.2 and SU4.3 lobe complex types, representative of both the Eastern Catán-Lil and Chachil basins, detailing the stacking patterns and distribution of HEBs and TFDs (shown orthogonal to primary flow direction).

Several exhumed systems have shown that variations in the volume and type of flows entering a basin, induce changes in sandstone content and thickness trends of ponded or partially ponded successions, depending on the rate of overspill, on the size of flows with respect to the size of the basin, and the height of the confining topography (i.e. Hodgson & Haughton, 2004; Shultz & Hubbard, 2005; Amy *et al.*, 2007; Southern *et al.*, 2015; Soutter *et al.*, 2021).

In contrast, the SU4.2 fan formed a high sandstone content succession deposited across a smoother topography in the updip basin, likely in a moderately confined setting contained by its basin margins (e.g. Marini *et al.*, 2015). SU4.2 also marks increased downdip overspill to the Chachil Basin (Fig. 17A and B) that accumulated a mudstone-prone succession including some debrites and slumps at the base, and a few sandy heterolithic deposits. The rare sand-rich influxes to the downdip basin during SU4.2 might record larger volume flows that were diverted around, or breached, the Southern Chachil horst relief (Fig. 15) with a reduced topographic height (for example, few to tens of metres, Marini *et al.*, 2016), which acted as a 'spill point' as the two depocentres became partially connected (e.g. Vinnels *et al.*, 2010).

Spillover and abandonment

The SU4.3 fan records the sedimentary linkage of both depocentres, with deposition of a coarser-grained but moderate sandstone content succession across healed topography in the updip basin and across underfilled inherited rift topography in the downdip basin (Fig. 17A and B). Inherited rift and compaction-enhanced topography of mud-draped carbonate platforms on fault block highs induced higher confinement in the Chachil Basin. This resulted in the frontal pinchout of this intraslope fan over a downdip distance of *ca* 2 to 3 km against a frontal counterslope, with trapping of thick HEBs that pinchout in the depocentre axis, offset from the frontal fan pinchout dominated by lobe fringe low-density turbidites and TFDs (cf. Privat *et al.*, 2021; Martinez-Doñate *et al.*, 2023). Shallow sand-filled scours and/or gullies developed near the exit point in the updip basin, and mud-filled or sand-filled scours and coarse-grained sandy bedforms developed in the downdip basin, suggesting a response to gradient change across the transverse topographic high that acted as a sill (e.g. Smith, 2004) (Fig. 17A and B). Therefore, during the spill phase, the system prograded in the downdip basin without marked knickpoint development and headward channel incision. Alternatively, channels could have a muddy infill (Smith, 2004), which may be difficult to identify at outcrop. Finally, thinning-upward of the SU4.3 fan and accumulation of a thick mudstone succession (hundreds of metres) across both basins suggests either lateral switching of sediment routes or regional reduction in sand supply. Either way, the sediment supply system terminated prior to the healing phase associated with major incision of the intraslope fans by parent feeder channel-levée systems (Beaubouef & Friedmann, 2000; Booth *et al.*, 2003).

Comparison with other fill-and-spill systems

Basin-fill patterns

Fill-and-spill systems are poorly recognized in rift basin-fills despite the favourable physiography (e.g. Ravnås & Steel, 1997; Argent *et al.*, 2000; Ravnås *et al.*, 2000; Tillmans *et al.*, 2021; Jones *et al.*, 2023). Here, the early post-rift axial (basin-margin parallel) sandy fairways interacted with inherited rift topography, like tortuous corridors (*sensu* Smith, 2004) and controlled the distribution of sandy depocentres (Fig. 16). The confinement of the sandy fairways by lateral topographic barriers (i.e. the Puesto Rincón del Polo horst) permitted the coeval development of sand-rich (i.e. Chachil and Eastern Catán-Lil Basin) and adjacent sand-starved (i.e. Chacaico Basin) depocentres (Figs 3 and 17). The stratigraphic architecture of the basin-fill (Fig. 18A) shows local fill-and-spill across a transverse topographic barrier (i.e. the Southern Chachil horst) and sustained progradation of intraslope fans from updip to downdip depocentres. In contrast, syn-rift fill-and-spill systems evolving across transverse fault-block highs record initial ponding then spilling from updip to downdip depocentre, until fault-block uplift cuts-off sand supply to the distal depocentre. This triggers emplacement of intrabasinal mass-transport deposits (MTDs) and renewed ponding in both depocentres, which then evolve as elongated trough-like basins routing axial sandy fairways (Ravnås & Steel, 1997; Steventon *et al.*, 2021) (Fig. 18B).

In the studied system, the different evolutionary stages from disconnected to linked early post-rift depocentres across inherited rift topography, record a change from partial ponding, through overspill, to spillover with erosion and bypass, with each stage separated by a muddy 'blanketing' phase (e.g. Booth *et al.*, 2003). This evolution features a vertical coarsening-upward

trend, increasing sandstone content upward and spatially across a transverse topographic high separating the two basins, flow deflection/reflection and associated bedforms, stratal thinning and common pinchout with clastic injectites towards confining slopes (Figs 15 and 17). All of these characteristics are observed in analogous minibasins of similar size in different tectonic settings (5 to 10 km wide and up to 20 km long) (Sinclair & Tomasso, 2002; Shultz & Hubbard, 2005; Amy *et al.*, 2007; Vinnels *et al.*, 2010; Tinterri & Tagliaferri, 2015). However, the evolution of the documented system is more compatible with a semi-enclosed or partially silled configuration of intraslope basins (e.g. Smith, 2004; Vinnels *et al.*, 2010) with intervening fault-block highs (i.e. sills), rather than three-dimensionally contained basins with full flow ponding in the updip basin (cf. Sinclair & Tomasso, 2002; Southern *et al.*, 2015). This configuration also contrasts with open stepped (cf. Deptuck *et al.*, 2012; Hay, 2012) or terraced (cf. Ravnås *et al.*, 2000; Tillmans *et al.*, 2021) slope settings, marked by subtle changes of slope gradient between steps and ramps, which lack counterslopes and/or topographic highs acting as effective sills between basins. Such systems developed across stepped slopes, promote the formation of high net : gross depocentres lacking MTDs and abundant HEBs, as the upper, mud-rich part of the flow is stripped downslope during system evolution (e.g. Adeogba *et al.*, 2005; Hay, 2012; Brooks *et al.*, 2018; Casagrande *et al.*, 2022).

In the studied system, which developed across a topographically complex slope, intrabasinal slumps and debrites are present. Intrabasinal MTDs are at the top of the lower partially ponded succession (SU4.1) in the updip basin, and within the spill succession (SU4.2) close to basin margins in both basins (Figs 17 and 18A). Moreover, the spillover stratigraphy (SU4.3) comprises distinctively thick debrites as part of HEBs (HEB 1) in the downdip basin, which are interpreted with a potential extrabasinal origin as mass-wasting (cf. Privat *et al.*, 2021, and Table 2 for details) (Figs 17 and 18A). It also differs from fill-and-spill systems, where MTDs tend to occur towards the top of ponded stratigraphy mainly due to tectonic pulses and/or slope progradation in foreland or transtensional basins (e.g. Shultz & Hubbard, 2005; Pyles, 2008; Salles *et al.*, 2014; Tinterri & Tagliaferri, 2015) (Fig. 18C). In many cases, intrabasinal MTDs are small, whereas large volume extrabasinal MTDs can plug the proximal basins, preventing or interrupting the development of spilling into the distal basins left starved, and forcing migration of the system, initiating a fill-and-spill cycle in a neighbouring depocentre.

These fill-and-spill systems are also prone to cut-off or diversion of sandy fairways across mobile salt or shale substrates. However, they behave differently due to more rapid subsidence with sediment loading, salt flow and syn-sedimentary growth structures, which control the duration and stacking of multiple fill-and-spill cycles in a given basin undergoing rapid renewal of accommodation (Beaubouef & Friedmann, 2000; Winker & Booth, 2000; Booth *et al.*, 2003; Rodriguez *et al.*, 2021). Therefore, salt-withdrawal basin-fills develop a broader range of architectural elements, including abundant MTDs, channelized fans and channel-levée systems in the healing phase and condensed mudstone intervals (Booth *et al.*, 2003) (Fig. 18D). Mass-transport deposits are reported more in the upper, spillover and healing stratigraphy (Winker & Booth, 2000; Booth *et al.*, 2003; Wu *et al.*, 2020; Rodriguez *et al.*, 2021) than in the lower, ponded or confined stratigraphy (Beaubouef & Friedmann, 2000; Cumberpatch *et al.*, 2021). One main difference with other fill-and spill systems developed across non mobile salt or shale substrates, is that intrabasinal MTDs are more voluminous than extrabasinal MTDs and can dominate the onlap margins and/or stratigraphy of distal basins, representing up to 60% of the basin-fill (Beaubouef & Friedmann, 2000; Madof *et al.*, 2009; Beaubouef & Abreu, 2010; Poprawski *et al.*, 2021) (Fig. 18D).

Hybrid event beds in early post-rift intraslope fans: stratigraphic occurrence and spatial distribution

The stratigraphic and spatial variability of bed types (specifically TFDs and HEBs) in successive intraslope fans is presently poorly documented in fill-and-spill systems and only a few examples have been described (e.g. Haughton *et al.*, 2003; Tinterri & Tagliaferri, 2015; Soutter *et al.*, 2021) (Fig. 18). Herein, key characteristics of the Los Molles Formation fill-and-spill system include: (i) variability in TFD versus HEB types between each intraslope fan; (ii) different HEB stratigraphic patterns (cf. Haughton *et al.*, 2009) between SU4.2 (sporadic) and SU4.3 (throughout), with the overall increase in HEB occurrence from the updip to the downdip depocentre in both SU4.2 and SU4.3; and (iii)

Fig. 18. Comparison of the variable stratigraphic architectures and architectural elements in fill-and-spill systems with diverse confinement in different tectonic settings. (A) Fill-and-spill in early post-rift basins with inherited rift topography. Basin-fill records; (i) partial ponding with abundant Transitional Flow Deposits (TFDs), overspill showing local occurrence of intrabasinal mass-transport deposits (MTDs) near confining slopes and sporadic Hybrid Event Beds (HEBs), followed by (ii) spillover with erosion and bypass associated with scours and development of HEBs throughout the downdip basin, with flow transformation across relief (i.e. sill). The passive infill of inherited rift topography with moderate sediment supply rates, decreasing as the system shifts to lower slope and/or is abandoned, prevents the development of a healing phase and results in incomplete fill-and-spill cycle. (B) Fill-and-spill in tectonically active syn-rift basins (e.g. Ravnås & Steel, 1997; Argent *et al.*, 2000; Steventon *et al.*, 2021). Basin-fill records incomplete fill-and-spill cycles with; (i) ponding and (ii) spillover in the downdip basin both with development of slurry beds or HEBs at base and fringe of fan (cf. Haughton *et al.*, 2003), followed by (iii) cut-off sand supply in downdip basin and renewed ponding in updip basin due to fault growth and rejuvenated sill, with trigger of intrabasinal MTDs promoting the development of TFD-prone fans in the downdip basin (Steventon *et al.*, 2021). The progressive increase of accommodation controlled by fault-growth induces the change from transverse to axial routing of sandy systems in both basins. This eventually leads to the development of axial channel-levée systems, but no proper healing phase across the two basins and therefore results in incomplete fill-and-spill cycles. (C) Fill-and-spill in tectonically active foreland or transtensional basins (e.g. Shultz & Hubbard, 2005; Amy *et al.*, 2007; Pyles, 2008; Salles *et al.*, 2014; Southern *et al.*, 2015; Tinterri & Tagliaferri, 2015). Basin-fill records incomplete fill-and-spill cycles under moderate sediment supply rates mainly dominated by; (i) ponding in proximal basin with localized scours at break of slope on basin margin and occurrence of TFDs or sandy HEBs throughout fan (Shultz & Hubbard, 2005; Amy *et al.*, 2007; Southern *et al.*, 2015), or some slurry beds or HEBs at base and fringe of fan and at onlap margins adjacent to sills and/or MTDs (cf. Tinterri & Tagliaferri, 2015; Soutter *et al.*, 2021), and (ii) plugging of proximal basin by extrabasinal MTCs due to tectonic pulses, which interrupts the development of spill or healing phases and forces migration in distal depocentres, resulting in incomplete fill-and-spill cycles. (D) Fill-and-spill in salt-withdrawal basins [proximal basin based on Booth *et al.* (2003) and distal basin based on Beaubouef & Abreu (2010)]. Basin-fill records; (i) ponding and partial ponding with overspill and occurrence of highly erosive, large volume intrabasinal MTDs promoting TFDs and HEBs at onlap margins adjacent to sills. The following (ii) spill phase records development of transient channelized fans with bypass across sills in proximal basins and ponding across former MTDs in distal basin, promoting HEBs in the basal fans. The latest (iii) healing phase records plugging of distal basin by extrabasinal MTC, backstepping and diversion of feeder channel in updip basin with avulsion across MTD and final lateral migration of axial channel-levée system in proximal basin interrupted by salt growth fold. The abundance and large volume of MTDs and the thick fill-and-spill stratigraphy, are promoted by combined high sediment supply rates and rapid subsidence with sediment loading, growth structures and salt flow, which control the duration of fill-and-spill cycles.

the control on the stratigraphic increase of HEB occurrence at the system-scale (Fig. 17).

The effects of changes in basin confinement related to the inherited rift topography in the two depocentres, could have controlled the lobe complex dimensions and stratal termination style (Fig. 17C), resulting in different HEB spatial distributions and stratigraphic patterns (e.g. Southern *et al.*, 2015; Fonnesu *et al.*, 2018). Grain-size differences, and the nature of the cohesive muddy substrate being entrained (e.g. Mueller *et al.*, 2017; Pierce *et al.*, 2018) may also explain: (i) the textural differences of HEBs debritic divisions in SU4.2 and SU4.3; (ii) the paucity of banded divisions relative to TFDs with matrix-poor to heterolithic sandy bedform divisions in SU4.2 lobes; and (iii) well-developed banded divisions and matrix-rich sandy bedform divisions in SU4.3 lobes (cf. Figs 8 and 15). The potential control of substrate differences on TFD and HEB types is also suggested by the blueish silty and grey calcareous mudstone clasts only found in SU4.2 lobes and the dominant dark grey clayey mudstone clasts in SU4.3 lobes.

The stratigraphic pattern of HEBs in SU4.2 is characterized by a sporadic occurrence of dominantly sandy HEBs (HEB 5) and clustered muddy HEBs (HEB 2) at the base of lobe complexes mainly dominated by TFDs. In contrast, SU4.3 is characterized by sandy HEBs (HEB 3 to 4) throughout lobe complexes and sporadic occurrence of muddy HEBs (HEB 1) in the uppermost lobe complexes (Fig. 17C). This HEB stratigraphic pattern is corroborated with a systematic spatial increase in HEBs in both SU4.2 and SU4.3 intraslope fans, downdip from the Eastern Catán-Lil Basin to the Chachil Basin, where HEBs can extend for up to 3 to 4 km from

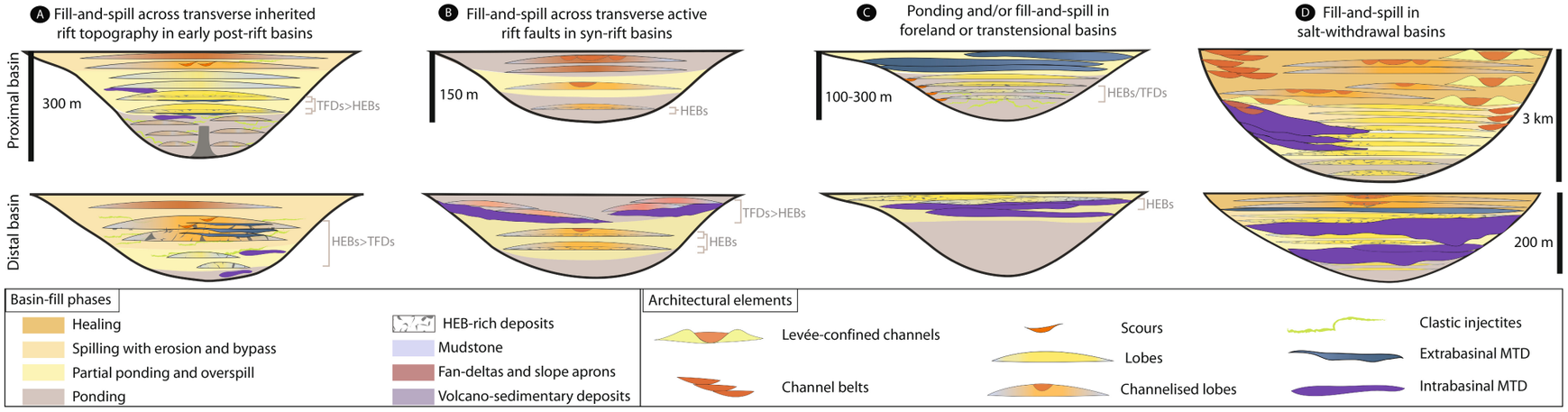

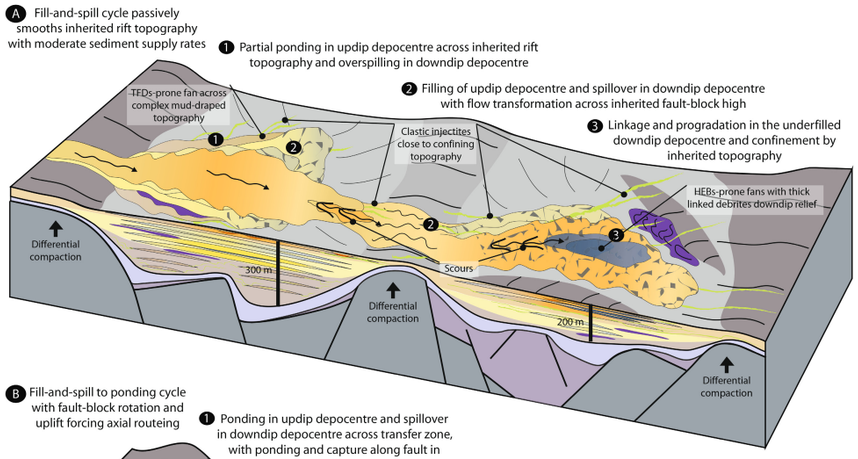

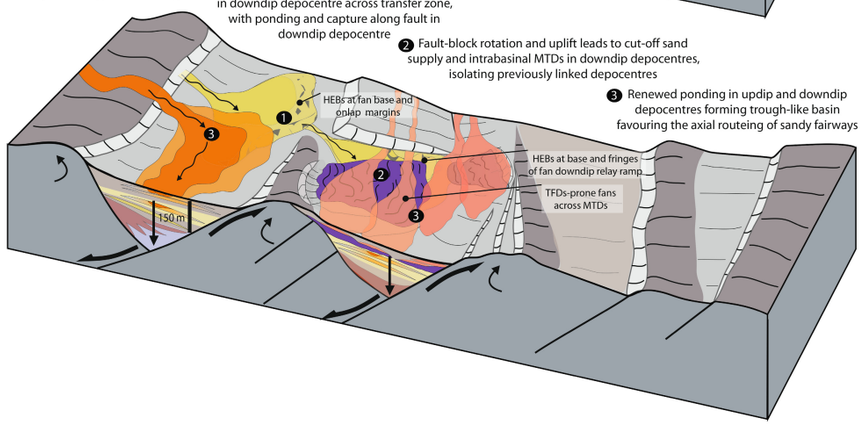

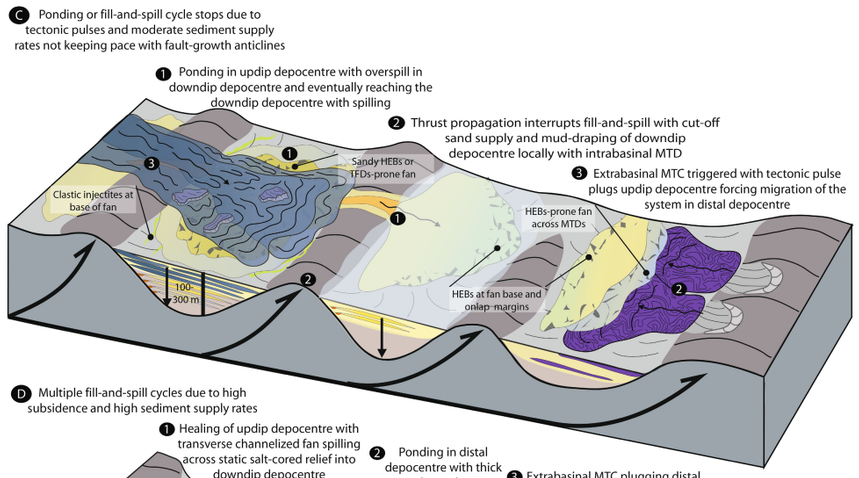

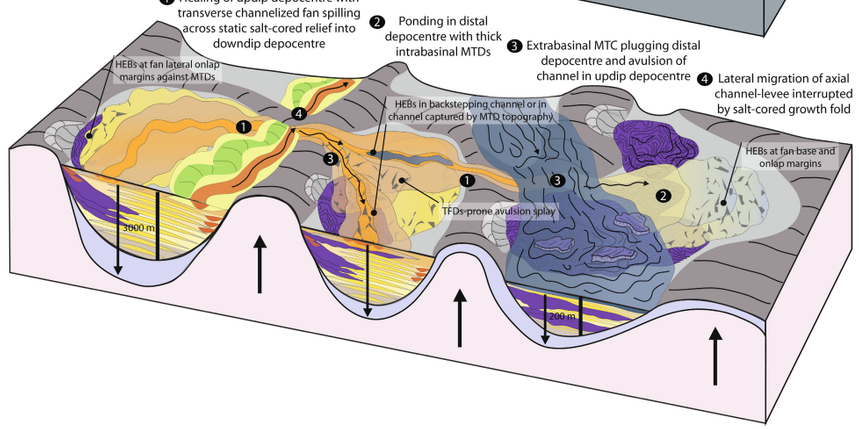

axis to pinchout of lobe complexes (cf. Privat *et al.*, 2021; Martinez-Doñate *et al.*, 2023) (Fig. 17A). Therefore, the high proportion of HEBs developed in the downdip Chachil Basin is interpreted to reflect flow transformation, with local enhanced flow acceleration, muddy substrate erosion and bypass across transverse relief of the Southern Chachil horst (Fig. 17B). This resulted in a sustained clustering of HEBs in the downdip basin in successive intraslope fans (SU4.2 and SU4.3), like the pattern observed at the break of slope in channel-lobe transition zones (e.g. Ito, 2008; Mueller *et al.*, 2017; Brooks *et al.*, 2022), until the local reduction of relief. Additionally, HEB occurrence throughout SU4.3 in the Chachil Basin could have been aided by confinement and flow transformation against multiple confining basin margins (Southern *et al.*, 2015).

At system scale, the successive intraslope fans record an overall stratigraphic increase of HEB occurrence from SU4.1 to SU4.3, with the youngest SU4.3 fan particularly enriched in HEBs, compared to SU4.2 and SU4.1 fans dominated by TFDs (Fig. 17C). This pattern is concomitant with an increase of matrix content in lobes and coarsening of grain-size and clast-size (Fig. 17A), which has been related to an increase of flow magnitude, erosion and bypass of coarser grained sediment fractions downslope (from SU4.1 to SU4.3). This change might record an increased flow confinement due to the propagation of slope channel systems (Maier *et al.*, 2011; Fildani *et al.*, 2013; Hodgson *et al.*, 2016) and gullies or canyons (Alves *et al.*, 2003; Jackson *et al.*, 2021) in response to slope steepening. This could explain deposition by unusually large volume, long run-out and high-energy flows, subject to substrate entrainment and flow transformation after bypassing updip slopes (e.g. Fonnesu *et al.*, 2018; Pierce *et al.*, 2018), resulting in progradation of the system with enhanced HEB development. Therefore, the changes recorded from SU4.1 to SU4.3 might be the stratigraphic expression of a wider system change, with re-adjustment to a higher gradient slope marking a period of disequilibrium and enhanced erosion (e.g. Haughton *et al.*, 2009).

The present findings have implications for fill-and-spill systems, highlighting the variability of TFD and HEB types and their different stratigraphic patterns between successive intraslope fans and spatially across the two basins, in response to changes in topography and confinement. In such fill-and-spill systems, HEBs are likely to be more developed during the sedimentary linkage of depocentres (spillover phase) in the downdip basin. In contrast, the facies differences in TFD and HEB types developed seem to be more dependent on the nature of substrate entrained and the run-out distance. These changes in stratigraphic and spatial TFD and HEB distribution between early post-rift intraslope fans reveal more complicated patterns in fill-and-spill systems, than the spatial HEB segregation towards the distal parts of fans in unconfined basin-floor systems (Haughton *et al.*, 2003; Hodgson, 2009; Kane & Pontén, 2012; Spychala *et al.*, 2017). This suggests that such predictive models should be applied with caution in other late syn-rift to early post-rift systems subject to intermittent periods of slope disequilibrium (e.g. Haughton *et al.*, 2003; Deller, 2005; Fugelli & Olsen, 2007; Southern *et al.*, 2017; Steventon *et al.*, 2021). The stratigraphic occurrence and variability of bed types, and the evolution of pinchout patterns in the studied fill-and-spill system reveal striking differences in confinement and flow transformation between individual depocentres, with implications for the development of stratigraphic traps and distribution of heterogeneities or flow baffles. These changes reflect the spatial and temporal evolution of the depositional system across topography, suggesting that other fill-and-spill systems in active tectonic settings (Fig. 18) subject to slope disequilibrium, might develop a range of similar features that require further investigation.

CONCLUSIONS

The Early Jurassic Los Molles Formation constitutes a unique exhumed example of early post-rift intraslope fans developed in a series of depocentres across inherited rift topography. New U–Pb ages presented in this study show that the early post-rift intraslope fans have a minimum late Early Toarcian age, which taken together with provenance analysis and sedimentology suggest that the main sediment supply was from the volcanic island arc margin, with axial sediment routing subparallel to the cratonic basin margin. The vertical stratigraphic evolution from SU4.1 through SU4.2 to SU4.3 fans, is marked by an increase in grain-size, clast content, matrix, erosional and bypass features and hybrid event beds (HEBs), reflecting increased flow energy and capacity, which is

associated with system progradation and progressive slope steepening.

Inherited rift topography controlled the compartmentalization of sand and evolution from disconnected to linked early post-rift depocentres, with the development of successive sandy fans, from partial ponding, through flow stripping and overspill, to spillover with erosion and bypass. This fill-and-spill system is characterized by the large-scale stratigraphic architecture and sedimentological changes from the SU4.1 to SU4.3 fans with:

- Variable lobe complex characteristics (thickness, sandstone content, stacking and stratal termination patterns) in each early post-rift intraslope fan, reflecting their deposition with changing confinement due to progressive reduction of topography.
- Development of different transitional flow deposit (TFD) and HEB types in successive intraslope fans due to changes in substrate entrainment.
- Contrasting distribution of bed types [high-density turbidites (HDTs), TFDs and HEBs] between the two basin-fills and with a different stratigraphic pattern between successive fans, as a response to changing topography. Hybrid event beds increase in the downdip basin during the sedimentary linkage of depocentres (spill-over phase), with enhanced erosion of mud and associated flow transformation across transverse relief between the two basins.

The documented fill-and-spill system shows fine-scale variability in the nature and distribution of bed types, and changes in stratigraphic architecture in different basin-fills, which contrast with the simpler sand-rich nature of other static fill-and-spill systems, and can be used to help prediction of spatial and vertical changes in reservoir quality and connectivity.

ACKNOWLEDGEMENTS

This study is a collaboration between the University of Leeds (UK), Imperial College London (UK) and the CIG-University of La Plata (Argentina), funded by the Lobe Joint Industry Programme. Dr Bin Fu from the Australian National University of Canberra (Australia) is thanked for his contribution on U–Pb geochronology results. The authors warmly thank Louis Thoreau and Andy Emery for their precious field assistance and efforts to collect the best data. Dania Pascua (Geological Service and Provincial Mining of Zapala) is thanked for providing logistical support. The authors thank all the owners for land access and their welcome. We are also very grateful to the Retamal family for their continuous help and invaluable support during the field seasons. Sebastian Kaempfe-Droguett, Gabriel Giacomone and Adam McArthur are thanked for their constructive review comments that helped to improve the final version of this manuscript. Jaco Baas, Adam McArthur and Elaine Richardson are also thanked for editorial handling.

CONFLICT OF INTEREST

The authors declare no conflict of interest for this previously unpublished work.

DATA AVAILABILITY STATEMENT

The data that support the findings of this study are available from the corresponding author.

REFERENCES

Adeogba, A.A., **McHargue, T.R.** and **Graham, S.A.** (2005) Transient fan architecture and depositional controls from near-surface 3-D seismic data, Niger Delta continental slope. *AAPG Bull.*, **89**, 627–643.

Allen, J.R.L. (1973) A classification of climbing-ripple cross-lamination. *J. Geol. Soc. Lond.*, **129**, 537–541.

Allen, J.R.L. (1982) *Sedimentary Structures: Their Character and Physical Basis*. Elsevier, Amsterdam. 593 p.

Al-Suwaidi, A.H., **Hesselbo, S.P.**, **Damborenea, S.E.**, **Mancenido, M.O.**, **Jenkyns, H.C.**, **Riccardi, A.C.**, **Angelozzi, G.N.** and **Baudin, F.** (2016) The toarcian oceanic anoxic event (Early Jurassic) in the Neuquén Basin, Argentina: a reassessment of age and carbon isotope stratigraphy. *J. Geol.*, **124**, 171–193.

Alves, T.M., **Manuppella, G.**, **Gawthorpe, R.L.**, **Hunt, D.W.** and **Monteiro, J.H.** (2003) The depositional evolution of diapir- and fault-bounded rift basins: examples from the Lusitanian Basin of West Iberia. *Sediment. Geol.*, **162**, 273–303.

Amy, L.A., **Kneller, B.C.** and **McCaffrey, W.D.** (2007) Facies architecture of the Gres de Peïra Cava, SE France: landward stacking patterns in ponded turbiditic basins. *J. Geol. Soc. Lond.*, **164**, 143–162.

Argent, J.D., **Stewart, S.A.** and **Underhill, J.R.** (2000) Controls on the Lower Cretaceous Punt Sandstone Member, a massive deep-water clastic deposystem, Inner Moray Firth, U.K. North Sea. *Pet. Geosci.*, **6**, 275–285.

Arienti Gonçalves, L., **Arienti, L.M.**, **D'Avila, R.F.S.**, **Carbone, O.C.** and **Ribeiro, A.** (2022) High-resolution

sequence stratigraphy applied to turbidites: the case study of Jurassic Los Molles Formation, Neuquén basin, Argentina. *J. S. Am. Earth Sci.*, **120**, 104078.

Armella, C., **Leanza, H.A.** and **Corfu, F.** (2016) Synsedimentary ash rains and paleoenvironmental conditions during the deposition of the Chachil Formation (Pliensbachian) at its type locality, Neuquen Basin, Argentina. *J. S. Am. Earth Sci.*, **71**, 82–95.

Baas, J.H., **Best, J.L.**, **Peakall, J.** and **Wang, M.** (2009) A phase diagram for turbulent, transitional, and laminar clay suspension flows. *J. Sediment. Res.*, **79**, 162–183.

Baas, J.H., **Best, J.L.** and **Peakall, J.** (2011) Depositional processes, bedform development and hybrid bed formation in rapidly decelerated cohesive (mud-sand) sediment flows. *Sedimentology*, **58**, 1953–1987.

Baas, J.H., **Best, J.L.** and **Peakall, J.** (2016) Predicting bedforms and primary current stratification in cohesive mixtures of mud and sand. *J. Geol. Soc. Lond.*, **173**, 12–45.

Baas, J.H., **Tracey, N.D.** and **Peakall, J.** (2021a) Sole marks reveal deep-marine depositional process and environment: implications for flow transformation and hybrid event bed models. *J. Sediment. Res.*, **91**, 986–1009.

Baas, J., **Best, J.** and **Peakall, J.** (2021b) Rapid gravity flow transformation revealed in a single climbing ripple. *Geology*, **49**, 493–497.

Baker, M.L. and **Baas, J.H.** (2020) Mixed sand-mud bedforms produced by transient turbulent flows in the fringe of submarine fans: indicators of flow transformation. *Sedimentology*, **67**, 2645–2671.

Balázs, A., **Burov, E.**, **Matenco, L.**, **Vogt, K.**, **Francois, T.** and **Cloetingh, S.** (2017) Symmetry during the syn and post-rift evolution of extensional back-arc basins: the role of inherited orogenic structures. *Earth Planet. Sci. Lett.*, **462**, 86–98.

Beaubouef, R.T. and **Abreu, V.** (2010) MTCs of the Brazos-Trinity slope system; thoughts on the sequence stratigraphy of MTCs and their possible roles in shaping hydrocarbons traps. In: *Submarine Mass Movements and their Consequences, Advances in Natural and Technological Hazards Research* (Eds Mosher, D.C., Shipp, R.C., Moscardelli, L., Chaytor, J.D., Baxter, C.D.P., Lee, H.J. and Urgeles, R.), Vol. **28**, pp. 475–490. Springer, Dordrecht, The Netherlands.

Beaubouef, R.T. and **Friedmann, S.J.** (2000) High resolution seismic/sequence stratigraphic framework for the evolution of Pleistocene intra slope basins, western Gulf of Mexico: depositional models and reservoir analogs. In: *Deep-Water Reservoirs of the World, 20th Annual GCSSEPM Foundation Bob F. Perkins Research Conference, Houston* (Eds Weimer, P., Slatt, R.M., Coleman, J., Rossen, N.C., Nelson, H., Bouma, A.H., Styzen, M.J. and Lawrence, D.T.), pp. 40–60. SEPM Society for Sedimentary Geology, Tulsa, OK.

Bechis, F., **Cristallini, E.O.**, **Giambiagi, L.B.**, **Yagupsky, D.L.**, **Guzmán, C.G.** and **García, V.H.** (2014) Transtensional tectonics induced by oblique reactivation of previous lithospheric anisotropies during the Late Triassic to Early Jurassic rifting in the Neuquén basin: insights from analog models. *J. Geodyn.*, **79**, 1–17.

Bermudez, A., **Delpino, D.** and **Pángaro, F.** (2002) Volcanismo de arco asociado a procesos de subducción-extensión durante el Triásico Superior – Jurásico Inferior (Precuyano). Área Cerro Bandera, Cuenca Neuquina, Argentina. 5° Congreso de Exploración y Desarrollo de Hidrocarburos (Mar Del Plata).

Booth, J.R., **Dean, M.C.**, **DuVernay, A.E.** and **Styzen, M.J.** (2003) Paleo-bathymetric controls on the stratigraphic architecture and reservoir development of confined fans in the Auger Basin: central Gulf of Mexico slope. *Mar. Pet. Geol.*, **20**, 563–586.

Boulesteix, K., **Poyatos-Moré, M.**, **Flint, S.S.**, **Taylor, K.G.**, **Hodgson, D.M.** and **Hasiotis, S.T.** (2019) Transport and deposition of mud in deep-water environments: processes and stratigraphic implications. *Sedimentology*, **66**, 2894–2925.

Brinkworth, W., **Vocaturo, G.**, **Loss, M.L.**, **Mortaloni, E.M.**, **Giunta, D.L.** and **Massaferro, J.L.** (2018) Estudio cronoestratigráfico y evolución paleoambiental del Jurásico Inferior-Medio en el engolfamiento de la cuenca Neuquina, Argentina. In: *10° Congreso de Exploración y Desarrollo de Hidrocarburos, Mendoza. Sessiones Generales: "Energía y Sociedad, Aliados Inseparables"*, pp. 597–622. IAPG, Instituto Argentino del Petróleo y del Gas, Buenos Aires.

Brooks, H.L., **Hodgson, D.M.**, **Brunt, R.L.**, **Peakall, J.**, **Poyatos-Moré, M.** and **Flint, S.S.** (2018) Disconnected submarine lobes as a record of stepped slope evolution over multiple sea-level cycles. *Geosphere*, **14**, 1753–1779.

Brooks, H.L., **Ito, M.**, **Zuchuat, V.**, **Peakall, J.** and **Hodgson, D.M.** (2022) Channel-lobe transition zone development in tectonically-active settings: implications for hybrid bed development. *Depositional Rec.*, **8**, 829–868.

Burgess, P.M., **Flint, S.** and **Johnson, S.** (2000) Sequence stratigraphic interpretation of turbiditic strata: an example from Jurassic strata of the Neuquén basin, Argentina. *Geol. Soc. Am. Bull.*, **112**, 1650–1666.

de Cala, I.S. (2021) An Experimental and Field-Based Investigation into Decimetre-Scale Bedforms Formed by Turbidity Currents. PhD thesis, University of Leeds, UK.

Casagrande, J., **Hodgson, D.M.**, **Peakall, J.** and **Benac, P.M.** (2022) Fill-and-Spill, Tilt-and-Repeat (FaSTaR) cycles: stratigraphic evolution above a dynamic submarine stepped slope. *Basin Res.*, **34**, 2162–2188.

Chun, S.S., **Choe, M.Y.** and **Chough, S.K.** (2002) Armored mudstone boulders in submarine debris-flow deposits, the Hunghae Formation, Pohang Basin: an evidence for the large-scale slumping of adjacent area of a submarine channel or scar wall. *Geosci. J.*, **6**, 215–225.

Clare, M.A., **Le Bas, T.**, **Price, D.M.**, **Hunt, J.E.**, **Sear, D.**, **Cartigny, M.J.B.**, **Vellinga, A.**, **Symons, W.**, **Firth, C.** and **Cronin, S.** (2018) Complex and cascading triggering of submarine landslides and turbidity currents at volcanic islands revealed from integration of high-resolution onshore and offshore surveys. *Front. Earth Sci.*, **6**, 223.

Cobain, S.L., **Peakall, J.** and **Hodgson, D.M.** (2015) Indicators of propagation direction and relative depth in clastic injectites: implications for laminar versus turbulent flow processes. *Geol. Soc. Am. Bull.*, **127**, 1816–1830.

Cobain, S.L., **Hodgson, D.M.**, **Peakall, J.** and **Shiers, M.N.** (2017) An integrated model of clastic injectites and basin floor lobe complexes: implications for stratigraphic trap plays. *Basin Res.*, **29**, 816–835.

Cohen, K.M., **Finney, S.C.**, **Gibbard, P.L.** and **Fan, J.-X.** (2013) The ICS International Chronostratigraphic Chart. *Episodes*, **36**, 199–204.

Covault, J.A. and **Romans, B.W.** (2009) Growth patterns of deep-sea fans revisited: turbidite-system morphology in confined basins, examples from the California Borderland. *Mar. Geol.*, **265**, 51–66.

Cristallini, E., **Tomezzoli, R.**, **Pando, G.**, **Gazzera, C.**, **Martinez, J.M.**, **Quiroga, J.**, **Buhler, M.**, **Bechis, F.**,

Barredo, S. and **Zambrano, O.** (2009) Controles precuyanos en la estructura de la Cuenca Neuquina. *Rev. Asoc. Geol. Argentina*, **65**, 248–264.

Critelli, S. and **Ingersoll, R.V.** (1995) Interpretation of neovolcanic versus palaeovolcanic sand grains: an example from Miocene deep-marine sandstone of the Topanga Group (Southern California). *Sedimentology*, **42**, 783–804.

Critelli, S., **Criniti, S.**, **Ingersoll, R.V.** and **Cavazza, W.** (2023) Temporal and spatial significance of volcanic particles in sand(stone): implications for provenance and palaeotectonic reconstructions. In: *Volcanic Processes in the Sedimentary Record: When Volcanoes Meet the Environment* (Eds Di Capua, A., de Rosa, R., Kereszturi, G., Le Pera, E., Rosi, M. and Watt, S.F.L.), Vol. **520**, pp. 311–325. Geological Society of London, Bath.

Cucchi, R., **Leanza, H.A.**, **Repol, D.**, **Escosteguy, L.**, **González, R.** and **Danieli, J.C.** (2005) Hoja Geológica 3972-IV, Junín de los Andes. Provincia del Neuquén. Programa Nacional de Cartas Geológicas de la República Argentina a escala 1:250.000. *Inst. Geológia y Recur. Miner. Serv. Geológico Min. Argentino. Buenos Aires*, **357**, 102.

Cumberpatch, Z.A., **Kane, I.A.**, **Soutter, E.L.**, **Hodgson, D.M.**, **Jackson, C.A.-L.**, **Kilhams, B.A.** and **Poprawski, Y.** (2021) Interactions between deep-water gravity flows and active salt tectonics. *J. Sediment. Res.*, **91**, 34–65.

Dakin, N., **Pickering, K.T.**, **Mohrig, D.** and **Bayliss, N.J.** (2013) Channel-like features created by erosive submarine debris flows: field evidence from the Middle Eocene Ainsa Basin, Spanish Pyrenees. *Mar. Pet. Geol.*, **41**, 62–71.

Damborenea, S.E., **Echevarría, J.** and **Ros-Franch, S.** (2013) *Southern Hemisphere Palaeobiogeography of Triassic-Jurassic Marine Bivalves, Seaways and Landbridges: Southern Hemisphere Biogeographic Connections through Time, Springer Briefs in Earth System Sciences*. Springer Netherlands, Dordrecht.

Dasgupta, P. and **Manna, P.** (2011) Geometrical mechanisms of inverse grading in grain-flow deposits: an experimental revelation. *Earth Sci. Rev.*, **104**, 186–198.

de la Cruz, R. and **Suárez, M.** (1997) El Jurásico de la cuenca de Neuquén en Lonquimay, Chile; Formación Nacientes del Biobío (38-39 degrees S). *Rev. Geol. Chile*, **24**, 3–24.

D'Elia, L., **Bilmes, A.**, **Franzese, J.R.**, **Veiga, G.D.**, **Hernández, M.** and **Muravchik, M.** (2015) Early evolution of the southern margin of the Neuquén Basin, Argentina: tectono-stratigraphic implications for rift evolution and exploration of hydrocarbon plays. *J. S. Am. Earth Sci.*, **64**, 42–57.

Deller, K.E. (2005) Sedimentological Lithofacies, Internal Architecture and Evolution of Deep Marine Fans of the Tithonian Angel Formation, Northwestern Dampier Sub-Basin, North West Shelf, Australia. Unpublished PH.D. thesis, University of Adelaide, 305 p.

Deptuck, M.E., **Sylvester, Z.**, and **O'Byrne, C.J.** (2012) Pleistocene seascape evolution above a "simple" stepped slope—Western Niger Delta. In: *Application of the Principles of Seismic Geomorphology to Continental-Slope and Base-of-Slope Systems: Case Studies from Seafloor and Near-Seafloor Analogues* (Eds Prather, B.E,, Deptuck, M.E., Mohrig, D.C., van Hoorn, B. and Wynn, R.B.), 99, 199–222. SEPM Society for Sedimentary Geology, Tulsa, OK.

Dickinson, W.R. (1970) Interpreting detrital modes of graywacke and arkose. *J. Sediment. Res.*, **40**, 695–707.

Dickinson, W.R. and **Suczek, C.A.** (1979) Plate tectonics and sandstone compositions. *AAPG Bull.*, **63**, 2164–2182.

Dmitrieva, E., **Jackson, C.A.L.**, **Huuse, M.** and **Kane, I.A.** (2018) Regional distribution and controls on the development of post-rift turbidite systems: insights from the Paleocene of the eastern North Viking Graben, offshore Norway. In: *Petroleum Geology of NW Europe: 50 Years of Learning – Proceedings of the 8th Petroleum Geology Conference. Geol. Soc. of London, Petroleum Geology Conference Series* (Eds Bowman, M. and Levell, B.), pp. 147–170. Geological Society of London, Bath.

Dorobek, S.L. (2007) Carbonate-platform facies in volcanic-arc settings: characteristics and controls on deposition and stratigraphic development. In: *Formation and Applications of the Sedimentary Record in Arc Collision Zones: Geological Society of America Special Paper* (Eds Draut, A., Clift, P.D. and Scholl, D.W.), pp. 55–90. The Geological Society of America, Boulder, CO.

Dott, R.H. (1964) Wacke, greywacke and matrix—what approach to immature sandstone classification? *J. Sediment. Petrol.*, **34**, 625–632.

Eschard, R., **Albouy, E.**, **Gaumet, F.** and **Ayub, A.** (2004) Comparing the depositional architecture of basin floor fans and slope fans in the Pab Sandstone, Maastrichtian, Pakistan. In: *Confined Turbidite Systems* (Eds Lomas, S.A. and Joseph, P.), Vol. **222**, pp. 159–185. Geological Society of London, Bath.

Etienne, S., **Mulder, T.**, **Bez, M.**, **Desaubliaux, G.**, **Kwasniewski, A.**, **Parize, O.**, **Dujoncquoy, E.** and **Salles, T.** (2012) Multiple scale characterization of sand-rich distal lobe deposit variability: examples from the Annot Sandstones Formation, Eocene–Oligocene, SE France. *Sediment. Geol.*, **273–274**, 1–18.

Færseth, R.B. and **Lien, T.** (2002) Cretaceous evolution in the Norwegian Sea-a period characterized by tectonic quiescence. *Mar. Pet. Geol.*, **19**, 1005–1027.

Fildani, A., **Hubbard, S.M.**, **Covault, J.A.**, **Maier, K.L.**, **Romans, B.W.**, **Traer, M.** and **Rowland, J.C.** (2013) Erosion at inception of deep-sea channels. *Mar. Pet. Geol.*, **41**, 48–61.

Fonnesu, M., **Haughton, P.D.**, **Felletti, F.** and **McCaffrey, W.D.** (2015) Short length-scale variability of hybrid event beds and its applied significance. *Mar. Pet. Geol.*, **67**, 583–603.

Fonnesu, M., **Felletti, F.**, **Haughton, P.D.**, **Patacci, M.** and **McCaffrey, W.D.** (2018) Hybrid event bed character and distribution linked to turbidite system sub-environments: the North Apennine Gottero Sandstone (north-west Italy). *Sedimentology*, **65**, 151–190.

Franzese, J.R. and **Spalletti, L.A.** (2001) Late Triassic–early Jurassic continental extension in southwestern Gondwana: tectonic segmentation and pre-break-up rifting. *J. S. Am. Earth Sci.*, **14**, 257–270.

Franzese, J.R., **Veiga, G.D.**, **Schwarz, E.** and **Gómez-Pérez, I.** (2006) Tectonostratigraphic evolution of a Mesozoic graben border system: the Chachil depocentre, southern Neuquén Basin, Argentina. *J. Geol. Soc. Lond.*, **163**, 707–721.

Fugelli, E.M.G. and **Olsen, T.R.** (2007) Delineating confined slope turbidite systems offshore mid-Norway: the Cretaceous deep-marine Lysing Formation. *AAPG Bull.*, **91**, 1577–1601.

García Morabito, E. (2010) Tectónica y estructura del retroarco andino entre los 38°15′ y los 40° S. PhD thesis, Universidad de Buenos Aires, Buenos Aires, Argentina.

Gawthorpe, R.L. and **Leeder, M.R.** (2000) Tectono-sedimentary evolution of active extensional basins. *Basin Res.*, **12**, 195–218.

Ge, Z., **Nemec, W.**, **Gawthorpe, R.** and **Hansen, E.** (2017) Response of unconfined turbidity current to normal-fault topography. *Sedimentology*, **64**, 932–959.

Giacomone, G., **Olariu, C.**, **Steel, R.** and **Shin, M.** (2020) A coarse-grained basin floor turbidite system-the Jurassic Los Molles Formation, Neuquén basin, Argentina. *Sedimentology*, **67**, 1–35.

Gómez Omil, R., **Schmithalter, J.**, **Cangini, A.**, **Albariño, L.** and **Corsi, A.** (2002) El Grupo Cuyo en la Dorsal de Huincul, consideraciones estratigráficas, tectónicas y petroleras. Cuenca Neuquina. 5° Congreso de Exploración y Desarrollo de Hidrocarburos (Mar del Plata).

Gómez-Pérez, I. (2003) An Early Jurassic deep-water stromatolitic bioherm related to possible methane seepage (Los Molles Formation, Neuquén, Argentina). *Palaeogeogr. Palaeoclimatol. Palaeoecol.*, **201**, 21–49.

Gulisano, C.A. and **Guttiérrez Pleimling, A.R.** (1995) Field Guide. The Jurassic of the Neuquén Basin. Neuquén Province, Asociación Geológica Argentina, Serie E, 2: 1-111. Buenos.

Gulisano, C.A., **Guttiérrez Pleimling, A.R.** and **Digregorio, J.H.** (1984) Esquema estratigráfico de la secuencia jurásica del oeste de la provincia del Neuquén. In: *9° Congreso Geológico Argentino, Bariloche*, pp. 236–259. Asociación Geológica Argentina, Buenos Aires.

Gutiérrez Pleimling, A.R., **Ambrosio, A.**, **Gómez, C.**, **Bustos, G.**, **González, J.M.**, **Guzmán, C.** and **Tapia, F.** (2021) Sequence-stratigraphic study of Cuyo Group in the Agua del Cajón Block, Neuquén Basin, Argentina. *J. S. Am. Earth Sci.*, **110**, 103373.

Hadlari, T., **Midwinter, D.**, **Galloway, J.M.**, **Dewing, K.** and **Durbano, A.M.** (2016) Mesozoic rift to post-rift tectonostratigraphy of the Sverdrup Basin, Canadian Arctic. *Mar. Pet. Geol.*, **76**, 148–158.

Hansen, L.A.S., **Hodgson, D.M.**, **Pontén, A.**, **Bell, D.** and **Flint, S.S.** (2019) Quantification of basin-floor fan pinchouts: examples from the Karoo Basin, South Africa. *Front. Earth Sci.*, **7**, 12.

Haughton, P.D.W., **Barker, S.P.** and **McCaffrey, W.D.** (2003) 'Linked' debrites in sand-rich turbidite systems—origin and significance. *Sedimentology*, **50**, 459–482.

Haughton, P., **Davis, C.**, **McCaffrey, W.D.** and **Barker, S.** (2009) Hybrid sediment gravity flow deposits—Classification, origin and significance. *Mar. Pet. Geol.*, **26**, 1900–1918.

Hay, D.C. (2012) Stratigraphic Evolution of a tortuous corridor from the stepped slope of Angola. In: *Application of the Principles of Seismic Geomorphology to Continental-Slope and Base-of-Slope Systems: Case Studies from Seafloor and Near-Seafloor Analogues* (Eds Prather, B.E., Deptuck, M.E., Mohrig, D., van Hoorn, B. and Wynn, R.B.), Vol. **99**, pp. 163–180. SEPM Society for Sedimentary Geology, Tulsa, OK.

Heller, P.L. and **Dickinson, W.R.** (1985) Submarine ramp facies model for delta-fed, sand-rich turbidite systems. *AAPG Bull.*, **69**, 960–976.

Henstra, G.A., **Grundvåg, S.-A.**, **Johannessen, E.P.**, **Kristensen, T.B.**, **Midtkandal, I.**, **Nystuen, J.P.**, **Rotevatn, A.**, **Surlyk, F.**, **Sæther, T.** and **Windelstad, J.** (2016) Depositional processes and stratigraphic architecture within a coarse-grained rift-margin turbidite system: The Wollaston Forland Group, east Greenland. *Mar. Pet. Geol.*, **76**, 187–209.

Hodgson, D.M. (2009) Distribution and origin of hybrid beds in sand-rich submarine fans of the Tanqua depocentre, Karoo Basin, South Africa. *Mar. Pet. Geol.*, **26**, 1940–1956.

Hodgson, D.M. and **Haughton, P.D.W.** (2004) Impact of syndepositional faulting on gravity current behaviour and deep-water stratigraphy: Tabernas-Sorbas Basin, SE Spain. In: *Confined Turbidite Systems* (Eds Lomas, S.A. and Joseph, P.), Vol. **222**, pp. 135–158. Geological Society of London, Bath.

Hodgson, D.M., **Kane, I.A.**, **Flint, S.S.**, **Brunt, R.L.** and **Ortiz-Karpf, A.** (2016) Time-transgressive confinement on the slope and the progradation of basin-floor fans: implications for the sequence stratigraphy of deep-water deposits. *J. Sediment. Res.*, **86**, 73–86.

Hofstra, M., **Peakall, J.**, **Hodgson, D.M.** and **Stevenson, C.J.** (2018) Architecture and morphodynamics of subcritical sediment waves in an ancient channel-lobe transition zone. *Sedimentology*, **65**, 2339–2367.

Horton, B.K., **Fuentes, F.**, **Boll, A.**, **Starck, D.**, **Ramirez, S.G.** and **Stockli, D.F.** (2016) Andean stratigraphic record of the transition from backarc extension to orogenic shortening: a case study from the northern Neuquén Basin, Argentina. *J. S. Am. Earth Sci.*, **71**, 17–40.

Howell, J.A., **Schwarz, E.**, **Spalletti, L.A.** and **Veiga, G.D.** (2005) The Neuquén Basin: an overview. In: *The Neuquén Basin, Argentina: A Case Study in Sequence Stratigraphy and Basin Dynamics* (Eds Veiga, G.D., Spalletti, L.A., Howell, J.A. and Schwarz, E.), Vol. **252**, pp. 1–14. Geological Society of London, Bath.

Hsieh, Y.-H., **Liu, C.-S.**, **Suppe, J.**, **Byrne, T.B.** and **Lallemand, S.** (2020) The Chimei submarine canyon and fan: a record of Taiwan arc-continent collision on the rapidly deforming overriding plate. *Tectonics*, **39**, e2020TC006148.

Hurst, A., **Cartwright, J.** and **Duranti, D.** (2003) Fluidization structures produced by upward injection of sand through a sealing lithology. In: *Subsurface Sediment Mobilization* (Eds van Rensbergen, P., Hillis, R.R., Maltman, A.J. and Morley, C.K.), Vol. **216**, pp. 123–138. Geological Society of London, Bath.

Ingersoll, R.V. and **Suczek, C.A.** (1979) Petrology and provenance of Neogene sand from Nicobar and Bengal fans. DSDP site 211 and 218. *J. Sediment. Petrol.*, **49**, 1217–1228.

Ito, M. (2008) Downfan transformation from turbidity currents to debris flows at a channel-to-lobe transitional zone: the Lower Pleistocene Otadai Formation, Boso Peninsula, Japan. *J. Sediment. Res.*, **78**, 668–682.

Jackson, C.A.L., **Barber, G.P.** and **Martinsen, O.J.** (2008) Submarine slope morphology as a control on the development of sand-rich turbidite depositional systems: 3D seismic analysis of the Kyrre Fm (Upper Cretaceous), Måløy Slope, offshore Norway. *Mar. Pet. Geol.*, **25**, 663–680.

Jackson, C.A., **McAndrew, A.E.**, **Hodgson, D.M.** and **Dreyer, T.** (2021) Repeated degradation and progradation of a submarine slope over geological timescales. *J. Sediment. Res.*, **91**, 116–145.

Jones, D.J.R., **Dodd, T.J.H.** and **McCarthy, D.J.** (2023) The influence of complex palaeobathymetry on development of deep-lacustrine fan systems. *Mar. Pet. Geol.*, **149**, 106090.

Kane, I.A. and **Pontén, A.S.M.** (2012) Submarine transitional flow deposits in the Paleogene Gulf of Mexico. *Geology*, **40**, 1119–1122.

Klaus, A. and **Taylor, B.** (1991) Submarine canyon development in the Izu-Bonin forearc: a SeaMARC II and seismic survey of Aoga Shima Canyo. *Mar. Geophys. Res.*, **13**, 131–152.

Kochhann, K.G.D., **Baecker-Fauth, S.**, **Pujana, I.**, **da Silveira, A.S.** and **Fauth, G.** (2011) Toarcian-Aalenian (Early–Middle Jurassic) radiolarian fauna from the Los Molles Formation, Neuquén Basin, Argentina: taxonomy and paleobiogeographic affinities. *J. S. Am. Earth Sci.*, **31**, 253–261.

Kuenen, P.H. (1968) Origin of ptygmatic features. *Tectonophysics*, **6**, 143–158.

Lanés, S., **Giambiagi, L.**, **Bechis, F.** and **Tunik, M.** (2008) Late Triassic - Early Jurassic successions of the Atuel Depocenter: sequence stratigraphy and tectonic controls. *Rev. Asoc. Geol. Argent.*, **63**, 534–548.

Laursen, J. and **Normark, W.R.** (2003) Impact of structural and autocyclic basin-floor topography on the depositional evolution of the deep-water Valparaiso forearc basin, central Chile. *Basin Res.*, **15**, 201–226.

Leanza, H.A. and **Blasco, G.** (1990) Estratigrafía y ammonites pliensbachianos del área del Arroyo Ñireco, Neuquén, Argentina, con la descripción de Austromorphites gen. nov. *Rev. Asoc. Geol. Argent.*, **45**, 159–174.

Leanza, H.A., **Mazzini, A.**, **Corfu, F.**, **Llambías, E.J.**, **Svensen, H.**, **Planke, S.** and **Galland, O.** (2013) The Chachil Limestone (Pliensbachian–earliest Toarcian) Neuquén Basin, Argentina: U–Pb age calibration and its significance on the Early Jurassic evolution of southwestern Gondwana. *J. S. Am. Earth Sci.*, **42**, 171–185.

Leclerc, F., **Feuillet, N.** and **Deplus, C.** (2016) Interactions between active faulting, volcanism, and sedimentary processes at an Island arc: insights from Les Saintes channel, Lesser Antilles arc. *Geochem. Geophys. Geosyst.*, **17**, 2781–2802.

Leeder, M.R., **Collier, R.E.L.**, **Abdul Aziz, L.H.**, **Trout, M.**, **Ferentinos, G.**, **Papatheodorou, G.** and **Lyberis, E.** (2002) Tectono-sedimentary processes along an active marine/lacustrine half-graben margin: Alkyonides Gulf, E. Gulf of Corinth, Greece. *Basin Res.*, **14**, 25–41.

Legarreta, L. and **Uliana, M.A.** (1996) The Jurassic succession in west-central Argentina: stratal patterns, sequences and paleogeographic evolution. *Palaeogeogr. Palaeoclimatol. Palaeoecol.*, **120**, 303–330.

Legros, F. (2002) Can dispersive pressure cause inverse grading in grain-flows? *J. Sediment. Res.*, **72**, 166–170.

Lien, T. (2005) From rifting to drifting: effects on the development of deep-water hydrocarbon reservoirs in a passive margin setting, Norwegian Sea. *Nor. J. Geol.*, **85**, 319–332.

Llambías, E.J., **Leanza, H.A.** and **Carbone, O.** (2007) Evolución Tectono-magmática durante el pérmico al Jurásico temprano en la Cordillera del Viento (37°05′ S - 37°15′ S): Nuevas evidencias geológicas y geoquímicas del Inicio de la Cuencas Neuquina. *Rev. Asoc. Geol. Argent.*, **62**, 217–235.

Lowe, L.R. (1982) Sediment gravity flows: II Depositional models with special reference to the deposits of high-density turbidity currents. *J. Sediment. Petrol.*, **52**, 279–297.

Madof, A.S., **Christie-Blick, N.** and **Anders, M.H.** (2009) Stratigraphic controls on a salt-withdrawal intraslope minibasin, north-central Green Canyon, Gulf of Mexico: implications for misinterpreting sea-level change. *AAPG Bull.*, **93**, 535–561.

Maier, K.L., **Fildani, A.**, **Paull, C.K.**, **Graham, S.A.**, **McHargue, T.**, **Caress, D.** and **McGann, M.** (2011) The elusive character of discontinuous deep-water channels: new insights from Lucia Chica channel system, offshore California. *Geology*, **39**, 327–330.

Malkowski, M.A., **Schwartz, T.M.**, **Sharman, G.R.**, **Sickmann, Z.T.** and **Graham, S.A.** (2017) Stratigraphic and provenance variations in the early evolution of the Magallanes-Austral foreland basin: implications for the role of longitudinal versus transverse sediment dispersal during arc-continent collision. *AAPG Bull.*, **129**, 349–371.

Marini, M., **Milli, S.**, **Ravnås, R.** and **Moscatelli, M.** (2015) A comparative study of confined vs. semi-confined turbidite lobes from the Lower Messinian Laga Basin (Central Apennines, Italy): implications for assessment of reservoir architecture. *Mar. Pet. Geol.*, **63**, 142–165.

Marini, M., **Patacci, M.**, **Felletti, F.** and **McCaffrey, W.D.** (2016) Fill to spill stratigraphic evolution of a confined turbidite mini-basin succession, and its likely well bore expression: The Castagnola Fm, NW Italy. *Mar. Pet. Geol.*, **69**, 94–111.

Marsaglia, K. and **Ingersoll, R.V.** (1992) Compositional trends in arc-related, deep-marine sand and sandstone: a reassessment of magmatic-arc provenance. *Geol. Soc. Am. Bull.*, **104**, 1637–1649.

Marsaglia, K.M., **Boggs, S.**, **Clift, P.**, **Seyedolali, A.** and **Smith, R.** (1995) Sedimentation in western Pacific backarc basins: new insights from recent ODP drilling. In: *Active Margins and Marginal Basins of the Western Pacific. Geophysical Monograph Series* (Eds Taylor, B. and Natland, J.), pp. 291–314. American Geophysical Union (AGU), Washington, DC.

Martinez-Doñate, A., **Kane, I.A.**, **Hodgson, D.M.**, **Privat, A.M.-L.J.**, **Jackson, C.A.-L.**, **Schwarz, E.** and **Flint, S.S.** (2023) Stratigraphic change in flow transformation processes recorded in early post-rift deep-marine intraslope lobe complexes. *Sedimentology*, **70**, 1379–1412.

Martinsen, O.J. and **Bakken, B.** (1990) Extensional and compressional zones in slumps and slides in the Namurian of County Clare, Ireland. *J. Geol. Soc. Lond.*, **147**, 153–164.

Martinsen, O.J., **Lien, T.**, **Walker, R.G.** and **Collinson, J.D.** (2003) Facies and sequential organization of a mudstone-dominated slope and basin floor succession: the Gull Island Formation, Shannon Basin, Western Ireland. *Mar. Pet. Geol.*, **20**, 789–807.

Masalimova, L.U., **Lowe, D.R.**, **Sharman, G.R.**, **King, P.R.** and **Arnot, M.J.** (2016) Outcrop characterization of a submarine channel-lobe complex: the lower Mount Messenger Formation, Taranaki Basin, New Zealand. *Mar. Pet. Geol.*, **71**, 360–390.

McCave, I.N. and **Jones, K.P.** (1988) Deposition of ungraded muds from high-density non-turbulent turbidity currents. *Nature*, **333**, 250–252.

Mpodozis, C. and **Ramos, V.** (2008) Tectónica Jurásica en Argentina y Chile: extensión, subducción oblicua, rifting, deriva y colisiones? *Rev. Asoc. Geol. Argentina*, **63**, 481–497.

Mueller, P., **Patacci, M.** and **Di Giulio, A.** (2017) Hybrid event beds in the proximal to distal extensive lobe domain of the coarse-grained and sand-rich Bordighera turbidite system (NW Italy). *Mar. Pet. Geol.*, **86**, 908–931.

Muravchik, M., **D'Elia, L.**, **Bilmes, A.** and **Franzese, J.R.** (2011) Syn-eruptive/inter-eruptive relations in the syn-rift

deposits of the Precuyano Cycle, Sierra de Chacaico, Neuquén Basin, Argentina. *Sediment. Geol.*, **238**, 132–144.

Muravchik, M., **Bilmes, A.**, **D'Elia, L.** and **Franzese, J.R.** (2014) Alluvial fan deposition along a rift depocentre border from the Neuquén Basin, Argentina. *Sediment. Geol.*, **301**, 70–89.

Mutti, E. (1977) Distinctive thin-bedded turbidite facies and related depositional environments in the Eocene Hecho Group (South-central Pyrenees, Spain). *Sedimentology*, **24**, 107–131.

Mutti, E., **Tinterri, R.**, **Benevelli, G.**, **di Biase, D.** and **Cavanna, G.** (2003) Deltaic, mixed and turbidite sedimentation of ancient foreland basins. *Mar. Pet. Geol.*, **20**, 733–755.

Naipauer, M., **García Morabito, E.**, **Marques, J.C.**, **Tunik, M.**, **Rojas Vera, E.A.**, **Vujovich, G.I.**, **Pimentel, M.P.** and **Ramos, V.A.** (2012) Intraplate Late Jurassic deformation and exhumation in western central Argentina: constraints from surface data and U-Pb detrital zircon ages. *Tectonophysics*, **524–525**, 59–75.

Naipauer, M., **Morabito, E.G.**, **Manassero, M.**, **Valenica, V.V.** and **Ramos, V.A.** (2018) A provenance analysis from the lower jurassic units of the Neuquén Basin. Volcanic arc or intraplate magmatic input? In: *The Evolution of the Chilean-Argentinean Andes* (Eds Folguera, A., Contreras-Reyes, E., Heredia, N., Encinas, A.B., Iannelli, S., Oliveros, V.M., Dávila, F., Collo, G., Giambiagi, L., Maksymowicz, A., Iglesia Llanos, M.P., Turienzo, M., Naipauer, M., Orts, D.D., Litvak, V., Alvarez, O. and Arriagada, C.), pp. 191–222. Springer Earth System Sciences. Springer International Publishing, Cham.

Noda, A., **TuZino, T.**, **Furukawa, R.**, **Joshima, M.** and **Uchida, J.** (2008) Physiographical and sedimentological characteristics of submarine canyons developed upon an active forearc slope: the Kushiro Submarine Canyon, northern Japan. *Geol. Soc. Am. Bull.*, **120**(5/6), 750–767.

Paim, P.S.G., **Silveira, A.S.**, **Lavina, E.L.C.**, **Faccini, U.F.**, **Leanza, H.A.**, **Teixeira De Oliveira, J.M.** and **D'Avila, R.S.F.** (2008) High resolution stratigraphy and gravity flow deposits in the Los Molles formation (Cuyo Group-Jurassic) at La Jardinera region, Neuquén Basin. *Rev. Asoc. Geol. Argent.*, **63**, 728–753.

Paim, P.S.G., **Lavina, E.L.C.**, **Faccini, U.F.**, **da Silveira, A.S.**, **Leanza, H.** and **D'Avila, R.S.F.** (2011) Fluvial-derived turbidites in the Los Molles Formation (Jurassic of the Neuquén Basin): initiation, transport, and deposition. In: *Sediment Transfer from Shelf to Deep Water-Revisiting the Delivery System. AAPG Studies in Geology* (Eds Slatt, R.M. and Zavala, C.), pp. 95–116. American Association of Petroleum Geologists (AAPG), Tulsa, OK.

Pángaro, F., **Pereira, M.**, **Raggio, F.**, **Pioli, O.**, **Silvestro, J.L.**, **Zubiri, M.** and **Gozalvez, G.** (2006) Tectonic Inversion of the Huincul High, Neuquén Basin, Argentina: an Endangered Species. Stratigraphic evidences of its Disappearance. 9° Simp. Boliv. Explor. Subandean Basins.

Pángaro, F., **Pereira, D.M.** and **Micucci, E.** (2009) El sinrift de la dorsal de Huincul, Cuenca Neuquina: Evolución y control sobre la estratigrafía y estructura del área. *Rev. Asoc. Geol. Argent.*, **65**, 265–277.

Peakall, J., **Best, J.L.**, **Baas, J.**, **Hodgson, D.M.**, **Clare, M.A.**, **Talling, P.J.**, **Dorrell, R.M.** and **Lee, D.R.** (2020) An integrated process-based model of flutes and tool marks in deep-water environments: implications for palaeohydraulics, the Bouma sequence and hybrid event beds. *Sedimentology*, **67**, 1601–1666.

Pickering, K.T. and **Hiscott, R.N.** (1985) Contained (reflected) turbidity currents from the Middle Ordovician Cloridorme Formation, Quebec, Canada: an alternative to the antidune hypothesis. *Sedimentology*, **32**, 373–394.

Pierce, C.S., **Haughton, P.D.**, **Shannon, P.M.**, **Pulham, A.J.**, **Barker, S.P.** and **Martinsen, O.J.** (2018) Variable character and diverse origin of hybrid event beds in a sandy submarine fan system, Pennsylvanian Ross Sandstone Formation, western Ireland. *Sedimentology*, **65**, 952–992.

Poprawski, Y., **Basile, C.**, **Cumberpatch, Z.** and **Eude, A.** (2021) Mass transport deposits in deep-water minibasins: outcropping examples from the minibasins adjacent to the Bakio salt wall (Basque Country, Northern Spain). *Mar. Pet. Geol.*, **132**, 105194.

Prather, B.E. (2003) Controls on reservoir distribution, architecture and stratigraphic trapping in slope settings. *Mar. Pet. Geol.*, **20**, 529–545.

Prélat, A. and **Hodgson, D.M.** (2013) The full range of turbidite bed thickness patterns in submarine lobes: controls and implications. *J. Geol. Soc. Lond.*, **170**, 209–214.

Prélat, A., **Hodgson, D.M.** and **Flint, S.S.** (2009) Evolution, architecture and hierarchy of distributary deep-water deposits: a high-resolution outcrop investigation from the Permian Karoo Basin, South Africa. *Sedimentology*, **56**, 2132–2154.

Privat, A.M.-L.J. (2019) Sedimentology and Tectono-Stratigraphic Development of the Syn to Post-Rift Transition in Southern Neuquén Basin (Argentina) and Controls on Early Postrift Submarine Lobes of the Los Molles Formation. PhD thesis, University of Leeds, Leeds, UK.

Privat, A.M.-L.J., **Hodgson, D.M.**, **Jackson, C.A.L.**, **Schwarz, E.** and **Peakall, J.** (2021) Evolution from syn-rift carbonates to early post-rift deep-marine intraslope lobes: the role of rift basin physiography on sedimentation patterns. *Sedimentology*, **68**, 2563–2605.

Prosser, S. (1993) Rift-related linked depositional systems and their seismic expression. In: *Tectonics and Seismic Sequence Stratigraphy* (Eds Williams, G.D. and Dobb, A.), Vol. **71**, pp. 35–66. Geological Society of London, Bath.

Pujols, E.J., **Leva López, J.**, **Stockli, D.F.**, **Rossi, V.M.** and **Steel, R.J.** (2018) New insights into the stratigraphic and structural evolution of the middle Jurassic S. Neuquén Basin from detrital zircon (U-Th)/(He-Pb) and apatite (U-Th)/He ages. *Basin Res.*, **30**, 1280–1297.

Pyles, D.R. (2008) Multiscale stratigraphic analysis of a structurally confined submarine fan: Carboniferous Ross Sandstone, Ireland. *AAPG Bull.*, **92**, 557–587.

Rabineau, M., **Leroux, E.**, **Aslanian, D.**, **Bache, F.**, **Gorini, C.**, **Moulin, M.**, **Molliex, S.**, **Droz, L.**, **dos Reis, A.T.**, **Rubino, J.L.**, **Guillocheau, F.** and **Olivet, J.L.** (2014) Quantifying subsidence and isostatic readjustment using sedimentary paleomarkers, example from the Gulf of Lion. *Earth Planet. Sci. Lett.*, **388**, 353–366.

Ravnås, R. and **Steel, R.J.** (1997) Contrasting styles of Late Jurassic syn-rift turbidite sedimentation: a comparative study of the Magnus and Oseberg areas, northern North Sea. *Mar. Pet. Geol.*, **14**, 417–449.

Ravnås, R. and **Steel, R.J.** (1998) Architecture of marine rift-basin successions. *Am. Assoc. Pet. Geol. Bull.*, **82**, 110–146.

Ravnås, R., **Nøttvedt, A.**, **Steel, R.J.** and **Windelstad, J.** (2000) Syn-rift sedimentary architectures in the Northern North Sea. In: *Dynamics of the Norwegian Margin* (Ed Nøttvedt, A.), Vol. **167**, pp. 133–177. Geological Society of London, Bath.

Ravnås, R., **Berge, K.**, **Campbell, H.**, **Harvey, C.** and **Norton, M.J.** (2014) Halten Terrace Lower and Middle Jurassic inter-rift megasequence analysis: megasequence structure, sedimentary architecture and controlling parameters. In: *From Depositional Systems to Sedimentary Successions on the Norwegian Continental Margin* (Eds Martinius, A.W., Ravnås, R., Steel, R.J. and Wonham, J.P.), pp. 215–251. International Association of Sedimentologists, Wiley & Sons Ltd, West Sussex.

Riccardi, A.C. (1991) Jurassic and Cretaceous marine connections between the Southeast Pacific and Tethys. *Palaeogeogr. Palaeoclimatol. Palaeoecol.*, **87**, 155–189.

Riccardi, A.C., **Damborenea, S.E.**, **Manceñido, M.O.** and **Leanza, H.A.** (2011) Megainvertebrados del jurásico y su importancia geobiológica. In: *Geología y Recursos Naturales de La Provincia Del Neuquén: 18° Congreso Geológico Argentino, Neuquén*, pp. 441–464. Asociación Geológica Argentina, Buenos Aires.

Roberts, A.M., **Kuznir, N.J.**, **Yielding, G.** and **Beley, H.** (2019) Mapping the bathymetric evolution of the Northern North Sea: from Jurassic synrift archipelago through Cretaceous-Tertiary post-rift subsidence. *Pet. Geosci.*, **25**, 306–321.

Rodriguez, C.R., **Jackson, C.A.L.**, **Bell, R.E.**, **Rotevatn, A.** and **Francis, M.** (2021) Deep-water reservoir distribution on a salt-influenced slope, Santos Basin, offshore Brazil. *AAPG Bull.*, **105**, 1679–1720.

Romans, B.W., **Fildani, A.**, **Hubbard, S.M.**, **Covault, J.A.**, **Fosdick, J.C.** and **Graham, S.A.** (2011) Evolution of deep water stratigraphic architecture, Magallanes Basin, Chile. *Mar. Pet. Geol.*, **28**, 612–628.

Salles, L., **Ford, M.** and **Joseph, P.** (2014) Characteristics of axially-sourced turbidite sedimentation on an active wedge-top basin (Annot Sandstone, SE France). *Mar. Pet. Geol.*, **56**, 305–323.

Schiuma, M. and **Llambías, E.J.** (2008) New ages and chemical analysis on lower Jurassic volcanism close to the dorsal de Huincul, Neuquén. *Rev. Asoc. Geol. Argent.*, **63**, 644–652.

Schwarz, E., **Finzel, E.S.**, **Veiga, G.D.**, **Rapela, C.W.**, **Echevarria, C.** and **Spalletti, L.A.** (2021) U-Pb geochronology and paleogeography of the Valanginian–Hauterivian Neuquén Basin: implications for Gondwana-scale source areas. *Geosphere*, **17**, 244–270.

Shultz, M.R. and **Hubbard, S.M.** (2005) Sedimentology, stratigraphic architecture, and ichnology of gravity flow deposits partially ponded in a growth-fault-controlled slope minibasin, Tres Pasos Formation (Cretaceous), southern Chile. *J. Sediment. Res.*, **75**, 440–453.

Shumaker, L.E., **Sharman, G.R.**, **King, P.R.** and **Graham, S.A.** (2018) The source is in the sink: deep-water deposition by a submarine volcanic arc, Taranaki Basin, New Zealand. *Sedimentology*, **65**, 2506–2530.

Silvestro, J. and **Zubiri, M.** (2008) Convergencia oblicua: Modelo estructural alternativo para la dorsal Neuquina (39°S) - Neuquén. *Rev. Asoc. Geol. Argent.*, **63**, 49–64.

Sinclair, H.D. and **Tomasso, M.** (2002) Depositional evolution of confined turbidite basins. *J. Sediment. Res.*, **72**, 451–456.

Smith, R. (2004) Silled sub-basins to connected tortuous corridors; sediment distribution systems on topographically complex sub-aqueous slopes. In: *Confined Turbidite Systems* (Eds Lomas, S.A. and Joseph, P.), Vol. **222**, pp. 23–43. Geological Society of London, Bath.

Southern, S.J., **Patacci, M.**, **Felletti, F.** and **McCaffrey, W.D.** (2015) Influence of flow containment and substrate entrainment upon sandy hybrid event beds containing a co-genetic mud-clast-rich division. *Sediment. Geol.*, **321**, 105–122.

Southern, S.J., **Kane, I.A.**, **Warchoł, M.**, **Porten, K.W.** and **McCaffrey, W.D.** (2017) Hybrid event beds dominated by transitional-flow facies: character, distribution and significance in the Maastrichtian Springar Formation, north-west Vøring Basin, Norwegian Sea. *Sedimentology*, **64**, 747–776.

Soutter, E.L., **Bell, D.**, **Cumberpatch, Z.A.**, **Ferguson, R.A.**, **Spychala, Y.T.**, **Kane, I.A.** and **Eggenhuisen, J.T.** (2021) The influence of confining topography orientation on experimental turbidity currents and geological implications. *Front. Earth Sci.*, **8**, 620.

Spalletti, L.A., **Franzese, J.R.**, **Morel, E.**, **D'Elia, L.**, **Zúñiga, A.** and **Fanning, C.M.** (2010) Consideraciones acerca de la sedimentología, paleobotánica y geocronología de la Formación Piedra del Águila (Jurásico Inferior, Neuquén, República Argentina). *Rev. Asoc. Geol. Argent.*, **66**, 305–313.

Spychala, Y.T., **Hodgson, D.M.**, **Prélat, A.**, **Kane, I.A.**, **Flint, S.S.** and **Mountney, N.P.** (2017) Frontal and lateral submarine lobe fringes: comparing sedimentary facies, architecture and flow processes. *J. Sediment. Res.*, **87**, 75–96.

Steel, R.J., **Olariu, C.**, **Rossi, V.M.**, **Minisini, D.**, **Brinkworth, W.**, **Loss, L.**, **Giunta, D.** and **Vocaturo, G.** (2023) Prograding early to middle Jurassic margin, Neuquén Basin: topset process stratigraphy and morphodynamic sediment partitioning. *Basin Res.*, **35**, 978–1011.

Stevenson, C.J., **Jackson, C.A.L.**, **Hodgson, D.M.**, **Hubbard, S.M.** and **Eggenhuisen, J.T.** (2015) Deep-water sediment bypass. *J. Sediment. Res.*, **85**, 1058–1081.

Stevenson, C.J., **Peakall, J.**, **Hodgson, D.M.**, **Bell, D.** and **Privat, A.** (2020) Tb or not Tb: banding in turbidite sandstones. *J. Sediment. Res.*, **90**, 821–842.

Steventon, M.J., **Jackson, C.A.L.**, **Johnson, H.D.**, **Hodgson, D.M.**, **Kelly, S.**, **Omma, J.**, **Gopon, C.**, **Stevenson, C.** and **Fitch, P.** (2021) Evolution of a sand-rich submarine channel–lobe system, and the impact of mass-transport and transitional-flow deposits on reservoir heterogeneity: Magnus Field, Northern North Sea. *Pet. Geosci.*, **27**, 2020–2095.

Stow, D.A.V. and **Bowen, A.J.** (1980) A physical model for the transport and sorting of fine-grained sediment by turbidity currents. *Sedimentology*, **27**, 31–46.

Strachan, L.J., **Rarity, F.**, **Gawthorpe, R.L.**, **Wilson, P.**, **Sharp, I.** and **Hodgetts, D.** (2013) Submarine slope processes in rift-margin basins, Miocene Suez Rift, Egypt. *Geol. Soc. Am. Bull.*, **125**, 109–127.

Sumner, E.J., **Amy, L.A.** and **Talling, P.J.** (2008) Deposit structure and processes of sand deposition from decelerating sediment suspensions. *J. Sediment. Res.*, **78**, 529–547.

Sylvester, Z. and **Lowe, D.R.** (2004) Textural trends in turbidites and slurry beds from the Oligocene flysch of the East Carpathians, Romania. *Sedimentology*, **51**, 945–972.

Takano, O. (2002) Changes in depositional systems and sequences in response to basin evolution in a rifted and inverted basin: an example from the Neogene Niigata-Shin'etsu basin, Northern Fossa Magna, central Japan. *Sediment. Geol.*, **152**, 79–97.

Takano, O., **Tateishi, M.** and **Endo, M.** (2005) Tectonic controls of a backarc trough-fill turbidite system: the Pliocene Tamugigawa Formation in the Niigata–Shin'etsu inverted rift basin, Northern Fossa Magna, central Japan. *Sediment. Geol.*, **176**, 247–279.

Talling, P.J., **Masson, D.G.**, **Sumner, E.J.** and **Malgesini, G.** (2012) Subaqueous sediment density flows: depositional processes and deposit types. *Sedimentology*, **59**, 1937–2003.

Taylor, A.M. and **Goldring, R.** (1993) Description and analysis of bioturbation and ichnofabric. *J. Geol. Soc. Lond.*, **150**, 141–148.

Taylor, W.J., **Hodgson, D.M.**, **Peakall, J.**, **Kane, I.A.**, **Morris, E.A.** and **Flint, S.S.** (2024) Unidirectional and combined transitional flow bedforms: controls on process and distribution in submarine slope settings. *Sedimentology*, **71**, 1329–1362.

Tillmans, F., **Gawthorpe, R.L.**, **Jackson, C.A.L.** and **Rotevatn, A.** (2021) Syn-rift sediment gravity flow deposition on a Late Jurassic fault-terraced slope, Northern North Sea. *Basin Res.*, **33**, 1844–1879.

Tinterri, R. (2011) Combined flow sedimentary structures and the genetic link between sigmoidal- and hummocky-cross stratification. *GeoActa*, **10**, 43–85.

Tinterri, R. and **Tagliaferri, A.** (2015) The syntectonic evolution of foredeep turbidites related to basin segmentation: facies response to the increase in tectonic confinement (Marnoso-arenacea Formation, Miocene, Northern Apennines, Italy). *Mar. Pet. Geol.*, **67**, 81–110.

Veiga, G.D., **Schwarz, E.**, **Spalletti, L.A.** and **Massaferro, J.L.** (2013) Anatomy and sequence architecture of the early post-rift in the Neuquén Basin (Argentina): a response to physiography and relative sea-level changes. *J. Sediment. Res.*, **83**, 746–765.

Vergani, G.D., **Tankard, A.J.**, **Belotti, H.J.** and **Welsink, H.J.** (1995) Tectonic evolution and paleogeography of the Neuquén Basin, Argentina. In: *Petroleum Basins of South America. AAPG Memoir* (Eds Tankard, A.J., Suárez, R. and Welsink, H.J.), pp. 383–402. American Association of Petroleum Geologists (AAPG), Tulsa, OK.

Vinnels, J.S., **Butler, R.W.**, **McCaffrey, W.D.** and **Lickorish, W.H.** (2010) Sediment distribution and architecture around a bathymetrically complex basin: an example from the eastern Champsaur Basin, SE France. *J. Sediment. Res.*, **80**, 216–235.

Weaver, C. (1931) Paleontology of the Jurassic and Cretaceous of west central Argentina. Memoir University of Washington 1. Seattle, pp. 1–469.

Winker, C.D. and **Booth, J.R.** (2000) Sedimentary dynamics of the salt-dominated continental slope, Gulf of Mexico: integration of observations from the seafloor, near-surface, and deep subsurface. In: *Deep-Water Reservoirs of the World, 20th Annual GCSSEPM Foundation Bob F. Perkins Research Conference, Houston* (Eds Weimer, P., Slatt, R.M., Coleman, J., Rosen, N.C., Nelson, H., Bouma, A.H., Styzen, M.J. and Lawrence, D.T.), pp. 1059–1086. SEPM Society for Sedimentary Geology, Tulsa, OK.

Wu, N., **Jackson, C.A.L.**, **Johnson, H.D.**, **Hodgson, D.M.** and **Nugraha, H.D.** (2020) Mass-transport complexes (MTCs) document subsidence patterns in a northern Gulf of Mexico salt minibasin. *Basin Res.*, **32**, 1300–1327.

Yagupsky, D.L. (2009) Metodología para el estudio de sistemas compresivos y de sus controles estructurales. PhD thesis, Universidad de Buenos Aires, Facultad de Ciencias Exactas y Naturales, Argentina.

Yu, N.T., **Teng, L.S.**, **Chen, W.S.**, **Yue, L.F.** and **Chen, M.M.** (2013) Early post-rift sequence stratigraphy of a Mid-Tertiary rift basin in Taiwan: insights into a siliciclastic fill-up wedge. *Sediment. Geol.*, **286–287**, 39–57.

Zachariah, A.J., **Gawthorpe, R.** and **Dreyer, T.** (2009) Evolution and strike variability of early post-rift deep-marine depositional systems: lower to Mid-Cretaceous, North Viking Graben, Norwegian North Sea. *Sediment. Geol.*, **220**, 60–76.

Manuscript received 20 July 2023; revision accepted 24 February 2024

Supporting Information

Additional information may be found in the online version of this article:

Data S1 Figure S1. U-Pb geochronology results and Concordia ages for Tuffs 1 and 3 (calculated weighted arithmetic mean $^{206}Pb/^{238}U$ ages).

Figure S2. Sections located in the Chachil and Catán-Lil basins (see Fig. 5 for locations) indicating the position of the tuff samples analyzed in this study, at the base and top of Unit 3 which correspond to the Lower Los Molles Formation.

Table S1. Summary of SHRIMP-II U-Pb age results for zircons from Tuffs 1 and 3. Note the rated lines are data excluded due to a large error of measurement.

Figure S3. Detailed correlation panels of sandy subunits SU4.1, SU4.2 and SU4.3.

Table S2. Table of modal compositions and recalculated parameters used for ternary diagrams.

Table S3. Table showing the total point counts in the different classes of grain types used for recalculated parameters in percentages shown in Table S2 Qt (Qm + Qp); F (P + K); Lt (L + Qp); L (Lv + Ls + Lm); and, Lsm (Ls + Lm).

Table S4. Compositional modes table showing percentages for each class of grain types.

Table S5. Point count table for SU44.1-2 samples (cf. Fig. 5) showing grain types and class percentages used in Table S2.

Table S6. Point count table for SU44.3 samples (cf. Fig. 5) showing grain types and class percentages used in Table S2.